

# Parity Violation in Elastic Electron-Nucleon Scattering: Strangeness Content in the Nucleon

R. González-Jiménez,<sup>1</sup> J.A. Caballero,<sup>1</sup> and T.W. Donnelly<sup>2</sup>

*<sup>1</sup>Departamento de Física Atómica, Molecular y Nuclear,  
Universidad de Sevilla, 41080 Sevilla, SPAIN*

*<sup>2</sup>Center for Theoretical Physics, Laboratory for Nuclear Science and Department of Physics,  
Massachusetts Institute of Technology, Cambridge, MA 02139, USA*

## Abstract

Parity violation in elastic electron-nucleon scattering is studied with the basic goal of improving the understanding of electroweak hadronic structure with special emphasis on the strangeness content in the nucleon. Models for the parity-violating (PV) asymmetry are provided and compared with the world data measured at very different kinematics. The effects introduced in the PV asymmetry due to alternative descriptions of the hadronic structure are analyzed in detail. In particular, a wide selection of prescriptions for dealing with the electromagnetic and neutral current weak interaction nucleon form factors, including the most recent ones used in the literature, is considered.

## Contents

<b>I. Introduction</b>	2
<b>II. General formalism for PV elastic (<math>e, N</math>) scattering</b>	9
A. Hadronic Responses and PV Asymmetry	12
<b>III. Hadronic structure: EM and WNC nucleon form factors</b>	15
A. EM structure of the nucleon: $G_{E,M}^{p,n}$	18
B. Axial-vector nucleon form factor: $G_A^e$	27
C. Nucleon vector form factors with strangeness: $G_{E,M}^{(s)}$	30
<b>IV. Parity-violating asymmetry: analysis of results</b>	30
A. Dependence on EM nucleon structure	32
B. Dependence on axial-vector nucleon structure	37
C. Dependence on nucleon strangeness	39
D. Radiative Corrections	49
E. Global analysis of $\mathcal{A}^{PV}$	50
F. Q-weak Experiment	56
G. Additional analysis: Neutral weak effective couplings	59
H. Projections for Higher-Energy Experiments	62
<b>V. Conclusions</b>	64
<b>Acknowledgments</b>	68
<b>References</b>	68

## I. INTRODUCTION

Over the years electron scattering has provided much of the precise information on hadronic and nuclear structure. Most such studies have considered only the purely electromagnetic (EM) interaction, that is, parity-conserving (PC) electron scattering processes. The analysis of inclusive and semi-inclusive reactions, as well as the measurement of polarization observables in very different kinematical regimes, has allowed us to deepen very

significantly our knowledge of the internal structure of hadrons and nuclei: the EM nucleon form factors, the nuclear ground-state density, the momentum and energy distributions of nucleons inside nuclei, the role of meson-exchange currents, *etc.*, have been investigated in depth previously [1–6].

The weak interaction, although orders of magnitude weaker than the EM one, also plays a role in electron scattering processes leading to effects that can shed some light on ingredients of the reaction mechanism that are not available through the purely EM interaction. Studies of parity-violating (PV) observables through analyses of electron scattering — denoted simply as PV electron scattering to contrast it with PC scattering where only the EM interaction enters — has three basic motivations: i) to serve in testing the Standard Model of electroweak interactions, ii) to provide a tool for determining the electroweak form factors of the nucleon, and iii) to employ the semi-leptonic electroweak interaction as a probe of nuclear structure, much as PC (purely EM) electron scattering has been used for decades now. In this work, our interest is restricted to the second point. It is important to point out that the smallness of the weak coupling, compared with the EM one, forces one to analyze observables that are strictly linked to parity-violating effects, requiring at the same time, excellent control of the EM ingredients that enter into the description of the scattering reaction. Furthermore, from the combined study of electron scattering from the proton and from nuclei, involving elastic, inelastic and quasielastic regimes, additional useful constraints on the form factors can emerge. In this work we restrict ourselves to elastic PV electron-proton scattering. The extension to studies of nuclear structure effects will be considered in a forthcoming paper.

The first PV electron scattering experiment on deuterium was performed at high energies at SLAC in 1976 [7], where a powerful new experimental technique was introduced, the measurement of helicity-dependent electron scattering cross sections. Since then, considerable interest has emerged in the use of such experiments to study electroweak physics at intermediate energies. In particular, considerable attention has been paid to exploring the strange-quark content in the structure of the nucleon.

The existence of the quark sea and its influence on some basic properties of the nucleon (mass, spin, magnetic moment) has been firmly established in several experimental studies. However, the specific role of  $s\bar{s}$  pairs in the static EM properties of the nucleon still remains elusive. Polarization measurements in deep inelastic scattering (DIS) provides ac-

cess to the contribution of strange quarks to the nucleon spin. However, the analysis of several experiments has led to rather different conclusions: while the original EMC experiment [8] suggested a contribution of the order of  $\sim 10\%$ , more recent experiments [9, 10] are compatible with a null contribution (see [11] for details). Other discussions, both from theoretical and experimental points of view, also address the role of the  $s$ -quark with respect to the hadron mass [12–14]. In this work our interest is focused on the contribution of the strange quarks in the electroweak current of the nucleon. As already suggested by several authors [15, 16], knowledge of neutral current form factors, combined with the EM ones, provides access to specific strangeness content in the nucleon through analysis of PV electron scattering.

A complete description of the scattering process between electrons and hadrons and/or nuclei requires not only the dominant EM interaction but also the much smaller weak interaction, the latter being responsible for parity violation. Assuming the Born Approximation, *i.e.*, only one virtual boson exchanged in the process (photon  $\gamma$  for the EM interaction and neutral  $Z$  boson for the weak neutral current (WNC) process), the corresponding Feynman diagrams are depicted in Fig. 1. Because of the smallness of the weak coupling constant compared with the EM one, the leading-order PV contribution arises from the interference between the two processes shown diagrammatically in Fig. 1, namely, between the  $\gamma$ -exchange amplitude (diagram a: purely EM interaction) and the  $Z$ -exchange (diagram b: WNC process). In what follows we denote the scattering amplitudes associated with  $\gamma$ -exchange (Fig. 1 (a)) and  $Z$ -exchange (Fig. 1 (b)) as  $\mathcal{M}_\gamma$  and  $\mathcal{M}_Z$ , respectively. The contribution of the purely weak term  $|\mathcal{M}_Z|^2$  is typically negligible. It is important to stress that the PV interference contribution,  $Re(\mathcal{M}_\gamma^* \mathcal{M}_Z)$  is  $\sim 4$ – $5$  orders of magnitude smaller than the purely EM one,  $|\mathcal{M}_\gamma|^2$ . Hence, the determination of parity violation through electron scattering requires measurements of observables that only exist if the weak interaction comes into play. Furthermore, the investigation of the WNC nucleon form factors using PV electron scattering depends strongly on the depth of our knowledge of the purely EM form factors. Notice that higher-order corrections beyond the one-photon-exchange approximation in the EM sector, such as two-photon effects [17], can give contributions of the same order or higher than the  $\gamma$ – $Z$  interference term. Hence, it is important to explore how sensitive the EM nucleon form factors are to these higher-order corrections. In [18] it is argued that these corrections may affect the Rosenbluth separation, but are relatively much

less important for the extraction of the form factor ratio using polarization observables, and that, accordingly, using polarization degrees of freedom in elastic  $ep$  scattering can provide a clean separation of the form factors. In this work we will use the most recent models or prescriptions describing the EM nucleon form factors which account for effects coming from two-photon exchange (TPE) and other higher-order corrections in the EM interaction. Another topic of interest that has recently been investigated is the potential impact of isospin violations on the extraction of the nucleon strange vector form factors [19, 20].

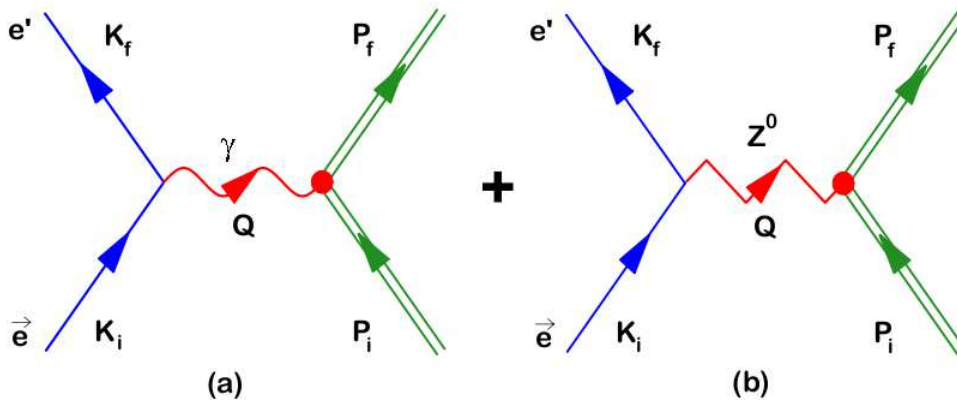


FIG. 1: One-boson-exchange diagrams for electron-proton scattering: (a) EM interaction and (b) WNC interaction.

Parity violation in electron scattering emerges from the measurement of the helicity asymmetry, also denoted as the PV asymmetry, that is given as the ratio between the difference and the sum of the cross sections corresponding to right and left-handed incident polarized electrons,

$$\mathcal{A}^{PV} = \frac{d\sigma^+ - d\sigma^-}{d\sigma^+ + d\sigma^-} = \frac{d\sigma^{PV}}{d\sigma^{PC}}, \quad (1)$$

where the index  $\pm$  indicates the helicity of the incident electron beam. It is important to point out that the above cross sections refer to single-arm (inclusive) scattering of longitudinally polarized electrons with no hadronic/nuclear polarizations. Otherwise, parity-conserving effects that are generally much larger than the effects coming solely from PV may also contribute to the asymmetry. As a basic example, in the case of exclusive  $A(\vec{e}, e'N)$  reactions, that is, polarized electrons and unpolarized nuclear targets, a purely EM response (called the fifth response) which is linked to the electron helicity and final-state interactions, contributes to the asymmetry unless coplanar kinematics are selected [5]. Similar comments

also apply to inclusive  $(\vec{e}, e')$  processes but with nuclear polarizations [6]. In contrast, in the particular case of single-arm electron scattering with no hadronic polarization, the purely EM cross section does not depend on the electron helicity; thus the difference in the numerator in Eq. (1) only enters because of the weak interaction (given through the interference between the amplitudes  $\mathcal{M}_\gamma$  and  $\mathcal{M}_Z$ ), and therefore, a value of  $\mathcal{A}^{PV} \neq 0$  is a clear signature of PV effects (exchange of the  $Z$ -boson). On the other hand, the sum in the denominator is dominated by the EM interaction (basically twice the unpolarized cross section), since residual contributions from the interference terms are negligible.

In recent years a great deal of effort has been devoted to the measurement and determination of the PV asymmetry. The analysis of data requires increasingly precise knowledge of the EM and WNC nucleon form factors. In what follows we summarize the main experimental programs that are focused on PV electron scattering from the proton, and in some cases using deuterium or helium.

1. **SAMPLE** [21, 22] These experiments were run at MIT-Bates and involved PV electron scattering from hydrogen and deuterium targets. Longitudinally polarized electrons with an energy of about 200 MeV were employed with scattering at large angles.
2. **HAPPEX** [23–26] This sequence of experiments employs the facilities of Jefferson Lab (Hall A). The energy of the polarized electron beam is typically around 3 GeV and both hydrogen and helium have been used as targets; forward-angle scattering is involved in all cases.
3. **PVA4** [27–29] This experiment was undertaken at MAMI (Mainz). To date longitudinally polarized electrons were scattered from hydrogen and various electron beam energies and scattering angles were employed. Future measurements are planned for hydrogen and deuterium.
4. **G0** [30, 31] This experiment was undertaken in Hall C (Jefferson Lab). Polarized electrons were scattered from hydrogen and deuterium. Forward- and backward-angle scattering measurements have been made, where in the forward configuration recoil protons were detected at angles corresponding to electrons in the forward direction,

while in the backward configuration the apparatus was reversed and scattered electrons were detected.

5. **Q-weak [32–34]** Experiment performed at JLab. Polarized electrons scattered from hydrogen at very low momentum transfer serve as a Standard Model test. Data acquisition was completed in May, 2012 and their analysis is now in progress.
6. **PVDIS at 6 GeV [35]** This experiment aims to measure the parity-violating asymmetry for deep inelastic scattering (DIS) of polarized electrons from  $^2\text{H}$  at  $|Q^2| = 1.1$  and  $1.9$   $(\text{GeV}/c)^2$ . The combination of the two measurements (data analysis is presently in progress) will provide a significant constraint on non-perturbative QCD effects. This may shed light on the knowledge of the neutral effective weak coupling constant combination  $2C_{2u} - C_{2d}$ . This experiment is also sensitive to the weak effective couplings,  $C_{1u}$  and  $C_{1d}$ , and it will provide a baseline measurement for the future 12 GeV program [36] at JLab.

In this work we compare our theoretical predictions evaluated with several recent descriptions of the hadronic structure with all available  $\vec{e}p$  data. Electroweak radiative corrections as well as effects from higher-order terms in the description of the EM interaction have been incorporated in the analysis. Special attention is devoted to the strangeness content in the electric, magnetic and axial-vector nucleon form factors.

Several different approaches to studies of PV  $\vec{e}p$  scattering may be followed, including

- Performing measurements at specific values of momentum transfer but different values of the electron scattering angle and thereby extracting the hadronic responses without having to resort to model assumptions for the underlying form factors.
- Using PV  $\vec{e}p$  data from different measurements at different values of momentum transfer and scattering angle, although now invoking some representation for the underlying form factors. For very low momentum transfers it may be possible to make low- $Q^2$  expansions; however, for extended ranges of momentum transfer one has to resort to parametrizations of the form factors.

The first option is clearly preferable, although this has been possible only for a subset of the world data, and the second option at very low momentum transfers is only applicable for

that kinematic region. In the present study we follow the second option invoking specific “reasonable” models and/or parametrizations for the nucleon form factors. In particular, for the electromagnetic form factors we use all of high-quality the world data and consider several specific vector meson dominance based models, as well as several popular parametrizations of these quantities. When parity-conserving  $\vec{e}p$  scattering measurements differ significantly, we investigate the impact this has on the PV asymmetry. For the weak neutral current form factors we consider several parametrizations. The spirit of our approach follows that of [37] where the axial-vector and strangeness form factors were characterized by simple “reasonable” expressions containing a few parameters to be varied. As discussed later in the paper, we explore the consequences of having a non-traditional axial-vector form factor as suggested by some recent neutrino reaction studies.

In recent years, there has been a great deal of progress in studying the structure of the nucleon from a theoretical point of view (see [38] and refs. therein). In particular, computation of strangeness form factors using microscopic calculations based on lattice-QCD has been presented in previous work, for instance, results from the quenched calculations in [39, 40]. More recently, the nucleon’s strange form factors have been simulated [41], and preliminary determinations of  $\Delta s$  presented in [42–46]. A general study, combining lattice with chiral perturbation theory, can be found in [47, 48].

Here we summarize some of our key findings — these are discussed at length later. We show that the uncertainty associated with the description of the EM nucleon form factors can be comparable to that due to the particular choice for the nucleons axial-vector structure. Concerning the specific strangeness content in the nucleon, our analysis of all available data is basically consistent with zero magnetic strangeness. However, present data do not allow us to select a specific strangeness content value that provides a successful description of data at all values of  $Q^2$ . On the contrary, our study shows consistency with positive electric strangeness. Although some caution should be drawn from these general conclusions because of the present uncertainties in the evaluation of the PV asymmetry, our results emerge from a global analysis of world data showing the  $1\sigma$  and  $2\sigma$  confidence ellipses in the magnetic-electric strangeness plane. We have also applied our study to the Q-weak experiment [32–34], and have shown how the confidence region may change due to the hypothetical Q-weak measurement, and moreover, how the various descriptions of the EM and WNC form factors can importantly affect the interpretation of this experiment.

The general organization of the paper is as follows: in Sect. II we present the general formalism needed in the description of elastic electron-nucleon scattering processes with parity violation. We show how to evaluate the differential cross section and PV asymmetry specifying the different approaches considered in this study. The study of the hadronic structure is presented in Sect. III. The electroweak nucleon form factors that enter in the general expressions for the EM and WNC contributions are analyzed in detail. Very different prescriptions, widely used in the literature, for the EM nucleon form factors are considered, including some of the most recent descriptions. In Sect. IV we present the results obtained for the PV asymmetry. Various kinematical regimes are considered and we analyze the sensitivity of  $\mathcal{A}^{PV}$  to the specific choices made for the nucleon's EM form factors (Sect. IV A) and axial-vector form factor (Sect. IV B). The influence of the  $s\bar{s}$  sea quark in the electric and magnetic strangeness form factors is also investigated in detail (Sect. IV C). A systematic comparison between the theoretical results and experimental data is provided. As discussed later, for these kinds of study having excellent control over the EM structure of the nucleon is required before definitive conclusions on the strangeness content in the nucleon can be reached. The impact of radiative corrections is also briefly addressed (Sect. IV D). In Sect. IV E a global analysis of all data is presented, while in Sect. IV F implications for the interpretation of the Q-weak experiment and for potential future experiments at higher energies (Sect. IV H) are discussed. Finally, in Sect. V we summarize our basic results and present our conclusions.

## II. GENERAL FORMALISM FOR PV ELASTIC $(e, N)$ SCATTERING

In this section we summarize the general formalism involved in the description of elastic parity-violating electron-nucleon scattering. Although, for simplicity, we restrict ourselves to the plane-wave Born approximation (PWBA) with a single-boson ( $\gamma$  or  $Z$ ) exchange, higher-order electroweak corrections will be discussed and incorporated in the analysis of the results. The processes we consider are represented in Fig. 1. Here, an electron with four-momentum  $K_i^\mu = (\epsilon_i, \mathbf{k}_i)$  and helicity  $h$  is scattered through an angle  $\theta_e$  to four-momentum  $K_f^\mu = (\epsilon_f, \mathbf{k}_f)$ , exchanging a photon (EM interaction) or a neutral boson  $Z$  (WNC interaction). The hadronic variables are  $P_i^\mu = (E_i, \mathbf{p}_i)$  the incident nucleon four-momentum and  $P_f^\mu = (E_f, \mathbf{p}_f)$  the final one. The transferred four-momentum in the process is given by  $Q^\mu = (K_i - K_f)^\mu =$

$(P_f - P_i)^\mu = (\omega, \mathbf{q})$ . We use the conventions and metric of [49] and accordingly, with the notation employed in previous work,  $Q^2 = \omega^2 - q^2 \leq 0$ .

Given the restriction to the PWBA the transition matrix amplitude for the scattering process can be written as

$$S_{fi} = -i \int d^4X [j_{EM}^\mu(X) A_\mu(X) + j_Z^\mu(X) Z_\mu(X)] , \quad (2)$$

where we have introduced the EM and WNC leptonic currents,  $j_{EM}^\mu$ ,  $j_Z^\mu$ , and the corresponding quantum fields,  $A^\mu$  and  $Z^\mu$ , attached to the hadronic vertex. The explicit expressions for the leptonic currents are:

$$j_{EM}^\mu(X) = -e \bar{\Psi}(X) \gamma^\mu \Psi(X) \quad (3)$$

$$j_Z^\mu(X) = \frac{g}{4 \cos \theta_W} \bar{\Psi}(X) (a_V \gamma^\mu + a_A \gamma^5 \gamma^\mu) \Psi(X) , \quad (4)$$

where the vector and axial-vector electron couplings at tree level are assumed [50, 51]:

$$a_V \equiv g_V = -1 + 4 \sin^2 \theta_W , \quad a_A \equiv -g_A = -1 . \quad (5)$$

After some algebra the scattering amplitude can be finally cast in the form

$$S_{fi} = -\frac{(2\pi)^4}{V^2} \delta^4(P_f - P_i + K_f - K_i) \frac{mM}{\sqrt{\epsilon_i \epsilon_f E_i E_f}} [\mathcal{M}_\gamma + \mathcal{M}_Z] , \quad (6)$$

where  $m$  and  $M$  represent the electron and hadron masses, respectively, and where we have introduced the amplitudes

$$\mathcal{M}_\gamma = j_{EM}^\mu \left( \frac{-ig_{\mu\nu}}{Q^2} \right) J_{EM}^\nu \quad (7)$$

$$\mathcal{M}_Z = j_Z^\mu \left( \frac{ig_{\mu\nu}}{M_Z^2} \right) J_Z^\nu \quad (8)$$

with  $M_Z$  the neutral boson mass.

In the extreme relativistic limit (ERL) for the electrons,  $k_{i,f} \approx \epsilon_{i,f}$ , the differential cross section is given as

$$\begin{aligned} \frac{d\sigma}{d\Omega_f} &= \frac{m^2}{(2\pi)^2} \left( \frac{\epsilon_f}{\epsilon_i} \right)^2 \overline{\sum} \left[ j_\mu^{EM} \left( \frac{-i}{Q^2} \right) J_{EM}^\mu + j_\mu^Z \left( \frac{i}{M_Z^2} \right) J_Z^\mu \right]^* \\ &\times \left[ j_\nu^{EM} \left( \frac{-i}{Q^2} \right) J_{EM}^\nu + j_\nu^Z \left( \frac{i}{M_Z^2} \right) J_Z^\nu \right] , \end{aligned} \quad (9)$$

where the lab frame has been chosen, *i.e.*, the proton target is taken to be at rest. The symbol  $\overline{\sum}$  refers to sum/average over spins of final/initial particles other than the incident

electron which is assumed to be longitudinally polarized (see below). We may isolate the contribution coming solely from the EM interaction and the EM-WNC interference term:

$$\overline{\sum} [(j_\mu^{EM})^* (j_\nu^{EM}) (J_{EM}^\mu)^* (J_{EM}^\nu)] = l_{\mu\nu} W^{\mu\nu} \quad (10)$$

$$\overline{\sum} [(j_\mu^{EM})^* (j_\nu^Z) (J_{EM}^\mu)^* (J_Z^\nu)] = \tilde{l}_{\mu\nu} \widetilde{W}^{\mu\nu}, \quad (11)$$

where we have neglected the contribution linked to the purely WNC terms that are several orders of magnitude smaller than the interference term, and have introduced the leptonic ( $l_{\mu\nu}, \tilde{l}_{\mu\nu}$ ) and hadronic ( $W^{\mu\nu}, \widetilde{W}^{\mu\nu}$ ) tensors that can be evaluated from the general expressions for the EM and WNC current operators.

In the case of longitudinally polarized incident electrons, as assumed in this work, the leptonic tensors can be written as

$$l_{\mu\nu} = \frac{e^2}{8m^2} (s_{\mu\nu} + h a_{\mu\nu}) \quad (12)$$

$$\tilde{l}_{\mu\nu} = \frac{-eg}{4 \cos \theta_W} \frac{1}{8m^2} \left[ (a_V - h a_A) s_{\mu\nu} + (h a_V - a_A) a_{\mu\nu} \right], \quad (13)$$

where  $h$  refers to the electron helicity and where we have separated the overall tensor into symmetric ( $s_{\mu\nu}$ ) and antisymmetric ( $a_{\mu\nu}$ ) contributions:

$$s_{\mu\nu} = 4 \left( K_\mu^i K_\nu^f + K_\nu^i K_\mu^f + \frac{Q^2}{2} g_{\mu\nu} \right), \quad a_{\mu\nu} = 4i \epsilon_{\mu\nu\alpha\beta} K_i^\alpha K_f^\beta. \quad (14)$$

The hadronic tensors in Eqs. (10,11) are constructed from the general expressions for the hadronic EM/WNC current operators,

$$W^{\mu\nu} = e^2 S^{\mu\nu} = e^2 \frac{1}{2} \text{Tr} \left[ \frac{(\not{P}_i + M)}{2M} \overline{\Gamma}_{EM}^\mu \frac{(\not{P}_f + M)}{2M} \Gamma_{EM}^\nu \right] \quad (15)$$

$$\widetilde{W}^{\mu\nu} = \frac{eg}{4 \cos \theta_W} \left[ \widetilde{S}^{\mu\nu} + \widetilde{A}^{\mu\nu} \right] = \frac{eg}{4 \cos \theta_W} \frac{1}{2} \text{Tr} \left[ \frac{(\not{P}_i + M)}{2M} \overline{\Gamma}_Z^\mu \frac{(\not{P}_f + M)}{2M} \Gamma_{EM}^\nu \right], \quad (16)$$

where we have taken into account that the hadronic EM current is purely a polar vector whereas the WNC includes an axial-vector contribution. No hadronic polarizations are assumed.

The differential cross section corresponding to elastic electron-nucleon scattering can then be cast as

$$\begin{aligned} \frac{d\sigma^{(h)}}{d\Omega_f} &= \frac{1}{(2\pi)^2} \left( \frac{\epsilon_f}{\epsilon_i} \right)^2 \frac{e^2}{8Q^2} \left\{ \frac{e^2}{Q^2} s_{\mu\nu} S^{\mu\nu} \right. \\ &\quad \left. + \left( \frac{\sqrt{2}g}{4M_Z \cos \theta_W} \right)^2 \left[ (a_V - h a_A) s_{\mu\nu} \widetilde{S}^{\mu\nu} + (h a_V - a_A) a_{\mu\nu} \widetilde{A}^{\mu\nu} \right] \right\}, \quad (17) \end{aligned}$$

whose evaluation requires the explicit calculation of the hadronic tensors that depend on the EM and WNC nucleon form factors. Hence, a proper description of the internal structure of the nucleon is needed in order to get a realistic description of the scattering process. However, before entering into a detailed discussion of the specific structure of the hadronic currents, the cross section can also be expressed in terms of hadronic response functions obtained by taking the appropriate components of the single-nucleon tensors  $S^{\mu\nu}$ ,  $\tilde{S}^{\mu\nu}$  and  $\tilde{A}^{\mu\nu}$ :

$$\frac{d\sigma^{(h)}}{d\Omega_f} = \sigma_M \left( \frac{\epsilon_f}{\epsilon_i} \right) \left\{ v_L R^L + v_T R^T + \left( \frac{Q^2}{e^2} \right) \left( \frac{\sqrt{2}g}{4M_Z \cos \theta_W} \right)^2 \right. \\ \left. \times \left[ (a_V - ha_A)(v_L \tilde{R}^L + v_T \tilde{R}^T) + (ha_V - a_A)v_{T'} \tilde{R}^{T'} \right] \right\} \quad (18)$$

with  $\sigma_M$  the Mott cross section and  $v_k$  the lepton kinematical coefficients given in the ERL as

$$v_L = \left( \frac{Q^2}{q^2} \right)^2, \quad v_T = \tan^2 \theta_e / 2 - \frac{1}{2} \left( \frac{Q^2}{q^2} \right), \quad v_{T'} = \tan \theta_e / 2 \sqrt{\tan^2 \theta_e / 2 - \frac{Q^2}{q^2}}. \quad (19)$$

The functions  $R^K$  ( $\tilde{R}^K$ ) are the hadronic EM (weak) responses that contain all of the information on the structure of the nucleon. They are given as bilinear combinations of the corresponding tensors:  $R^L = S^{00}$ ,  $R^T = S^{xx} + S^{yy}$  (likewise for  $\tilde{R}^{L,T}$  in terms of  $\tilde{S}^{\mu\nu}$ ) and  $\tilde{R}^{T'} = 2i\tilde{A}^{xy}$  with the specific components referred to a coordinate system in which the  $z$ -axis lies along the direction of the transfer momentum  $\mathbf{q}$ ,  $xz$  is the scattering plane defined by the electron momenta  $\mathbf{k}_i$  and  $\mathbf{k}_f$  and the  $y$ -axis lies along  $\mathbf{k}_i \times \mathbf{k}_f$ . The indices  $L$  and  $T, T'$  indicate contributions in the tensors along  $\mathbf{q}$  and transverse to  $\mathbf{q}$ , respectively.

### A. Hadronic Responses and PV Asymmetry

The general structure of the tensors containing the EM and WNC contributions can be derived from general symmetry properties, Lorentz covariance, charge conjugation and time reversal invariance and, in the case of the EM interaction, current and parity conservation. The EM current operator for on-shell nucleons is simply given in the form:

$$\Gamma_{EM}^\mu = F_1 \gamma^\mu + i \frac{F_2}{2M} \sigma^{\mu\nu} Q_\nu \quad (20)$$

with  $F_1$  and  $F_2$  the Pauli and Dirac nucleon form factors, respectively. In the case of the WNC operator we have

$$\Gamma_Z^\mu = \tilde{F}_1 \gamma^\mu + i \frac{\tilde{F}_2}{2M} \sigma^{\mu\nu} Q_\nu + G_A^e \gamma^\mu \gamma^5 + \frac{\tilde{G}_P}{M_N} Q^\mu \gamma^5, \quad (21)$$

where  $\tilde{F}_{1,2}$  are the WNC vector form factors and  $G_A^e$  ( $\tilde{G}_P$ ) the axial-vector (pseudoscalar) ones.

Introducing these explicit expressions for the currents into Eqs. (15) and (16), the hadronic symmetric and antisymmetric contributions to the tensors are finally given by

$$\begin{aligned} 2M^2 S^{\mu\nu} &= (F_1 + F_2)^2 \left( P_i^\mu P_f^\nu + P_i^\nu P_f^\mu + \frac{1}{2} Q^2 g^{\mu\nu} \right) \\ &- \left[ F_2(F_1 + F_2) - F_2^2 \left( \frac{1}{2} - \frac{Q^2}{8M^2} \right) \right] (P_i + P_f)^\mu (P_i + P_f)^\nu \end{aligned} \quad (22)$$

$$\begin{aligned} 2M^2 \tilde{S}^{\mu\nu} &= (F_1 + F_2)(\tilde{F}_1 + \tilde{F}_2) \left( P_i^\mu P_f^\nu + P_i^\nu P_f^\mu + \frac{1}{2} Q^2 g^{\mu\nu} \right) \\ &- \left[ \frac{1}{2} F_2(\tilde{F}_1 + \tilde{F}_2) + \frac{1}{2} \tilde{F}_2(F_1 + F_2) - F_2 \tilde{F}_2 \left( \frac{1}{2} - \frac{Q^2}{8M^2} \right) \right] (P_i + P_f)^\mu (P_i + P_f)^\nu \end{aligned} \quad (23)$$

$$2M^2 \tilde{A}^{\mu\nu} = i(F_1 + F_2) G_A^e \epsilon^{\mu\nu\alpha\beta} P_\alpha^i P_\beta^f. \quad (24)$$

Note that the pseudoscalar term  $\frac{\tilde{G}_P}{M_N} Q^\mu \gamma^5$  does not contribute to PV electron scattering at the order considered here. The explicit expressions for the EM/WNC hadronic responses are the following:

$$R^L = (1 + \lambda) [F_1 - \lambda F_2]^2 \quad (25)$$

$$R^T = 2\lambda [F_1 + F_2]^2 \quad (26)$$

$$\tilde{R}^L = (1 + \lambda) [F_1 - \lambda F_2] [\tilde{F}_1 - \lambda \tilde{F}_2] \quad (27)$$

$$\tilde{R}^T = 2\lambda (F_1 + F_2) (\tilde{F}_1 + \tilde{F}_2) \quad (28)$$

$$\tilde{R}^{T'} = 2\kappa (F_1 + F_2) G_A^e, \quad (29)$$

where the lab frame has been assumed, *i.e.*,  $P_i^\mu = (M, \vec{0})$ ,  $P_f^\mu = (E_f, 0, 0, q)$ , and the usual dimensionless variables  $\lambda \equiv \omega/2M$  and  $\kappa \equiv q/2M$  have been introduced.

In terms of the scale of parity-violating effects,  $\mathcal{A}_0 = G_F |Q^2| / (2\sqrt{2}\pi\alpha)$ , with  $G_F = g^2 / (4\sqrt{2}M_Z^2 \cos^2 \theta_W)$  the Fermi coupling and  $\alpha$  the fine structure constant, the expression

for the differential cross section that results is

$$\begin{aligned} \frac{d\sigma^{(h)}}{d\Omega_f} &= \sigma_M \left( \frac{\epsilon_f}{\epsilon_i} \right) \left[ v_L R^L + v_T R^T \right. \\ &\quad \left. - \frac{\mathcal{A}_0}{2} \left( (a_V - ha_A)(v_L \tilde{R}^L + v_T \tilde{R}^T) + (ha_V - a_A)v_{T'} \tilde{R}^{T'} \right) \right]. \end{aligned} \quad (30)$$

As noted, PV effects (linked to  $\tilde{R}^K$  responses) can be isolated through  $\vec{e}N$  measurements. In particular, by measuring the cross sections corresponding to the two helicities  $h = \pm 1$  and taking their difference, the result depends on the EM/WNC interference responses (denoted simply as the PV cross section),

$$\left( \frac{d\sigma}{d\Omega_f} \right)^{PV} = \frac{1}{2} \left( \frac{d\sigma^{(+)}}{d\Omega_f} - \frac{d\sigma^{(-)}}{d\Omega_f} \right) = \sigma_M \left( \frac{\epsilon_f}{\epsilon_i} \right) \frac{\mathcal{A}_0}{2} \left[ a_A(v_L \tilde{R}^L + v_T \tilde{R}^T) - a_V v_{T'} \tilde{R}^{T'} \right].$$

On the contrary, by taking the sum of the helicity-dependent cross sections one gets the purely EM cross section plus a minor contribution coming from the EM/WNC interference that can be neglected. Hence, one may write

$$\left( \frac{d\sigma}{d\Omega_f} \right)^{PC} = \frac{1}{2} \left( \frac{d\sigma^{(+)}}{d\Omega_f} + \frac{d\sigma^{(-)}}{d\Omega_f} \right) \approx \sigma_M \left( \frac{\epsilon_f}{\epsilon_i} \right) \left[ v_L R^L + v_T R^T \right], \quad (31)$$

where the index PC refers to Parity-Conserving cross sections.

The helicity-difference asymmetry (also called the PV asymmetry) is defined as

$$\mathcal{A}^{PV} \equiv \frac{(d\sigma/d\Omega_f)^{PV}}{(d\sigma/d\Omega_f)^{PC}} = \frac{\mathcal{A}_0}{2} \left[ \frac{a_A(v_L \tilde{R}^L + v_T \tilde{R}^T) - a_V v_{T'} \tilde{R}^{T'}}{v_L R^L + v_T R^T} \right]. \quad (32)$$

Using the explicit expressions for the EM and WNC hadronic responses in Eqs. (25-29) and introducing the Sachs form factors, *viz.*,  $G_E = F_1 - \tau F_2$  and  $G_M = F_1 + F_2$  (likewise for  $\tilde{G}_{E,M}$  in terms of  $\tilde{F}_{1,2}$ ), the PV asymmetry can be written as

$$\mathcal{A}^{PV} = \frac{\mathcal{A}_0}{2} \left[ \frac{a_A \left( \varepsilon G_E^N \tilde{G}_E^N + \tau G_M^N \tilde{G}_M^N \right) - a_V \sqrt{1 - \varepsilon^2} \sqrt{\tau(1 + \tau)} G_M^N G_A^{\varepsilon, N}}{\varepsilon (G_E^N)^2 + \tau (G_M^N)^2} \right], \quad (33)$$

with  $\tau \equiv |Q^2|/4M^2$ ,  $\varepsilon = [1 + 2(1 + \tau) \tan^2 \theta_e/2]^{-1}$  and the index  $N$  referring to protons or neutrons.

The analysis of the PV asymmetry in different kinematical regions is simplified by isolating the contributions linked to the electric (longitudinal), magnetic (transverse symmetric)

and axial-vector (actually magnetic/axial-vector interference; transverse antisymmetric) distributions. Thus, we may write

$$\mathcal{A}^{PV} = \mathcal{A}_E + \mathcal{A}_M + \mathcal{A}_A \quad (34)$$

with

$$\mathcal{A}_E = \frac{\mathcal{A}_0 a_{A\varepsilon} G_E^N \tilde{G}_E^N}{2 G^2} \quad (35)$$

$$\mathcal{A}_M = \frac{\mathcal{A}_0 a_{A\tau} G_M^N \tilde{G}_M^N}{2 G^2} \quad (36)$$

$$\mathcal{A}_A = -\frac{\mathcal{A}_0 a_V \sqrt{1 - \varepsilon^2} \sqrt{\tau(1 + \tau)} G_M^N G_A^{e,N}}{2 G^2}, \quad (37)$$

where we have introduced the term  $G^2 \equiv \varepsilon(G_E^N)^2 + \tau(G_M^N)^2 = (1 + \tau)\varepsilon F^2$  that depends only on the purely EM interaction. Note that both channels in the EM sector, *i.e.*, electric  $E$  and magnetic  $M$ , enter in the three separate PV asymmetry contributions defined in the above equations.

In the next section we focus on the analysis of the specific structure of the nucleon and provide various representations for the EM and WNC nucleon current operators.

### III. HADRONIC STRUCTURE: EM AND WNC NUCLEON FORM FACTORS

As shown in the previous section, the evaluation of PV observables (cross section, responses and helicity-asymmetry) requires knowledge of the EM and WNC nucleon form factors. In this section we show how to construct the electroweak hadronic currents and present a detailed study of the nucleon structure, comparing the results of different theoretical descriptions with experimental data.

The general Dirac structure of the vector and axial-vector currents in the lepton channel (to leading-order tree-level) is:  $j_V^\mu \sim \bar{u}_\ell \gamma^\mu u_\ell$  and  $j_A^\mu \sim \bar{u}_\ell \gamma^\mu \gamma^5 u_\ell$ , with  $u_\ell$  the lepton Dirac spinor. The EM and WNC hadronic currents,  $J_\mu^{EM}$ ,  $J_\mu^{WNC,V}$  and  $J_\mu^{WNC,A}$ , are characterized by the corresponding quark current operators:

$$J_\mu^{EM} = \sum_q Q_q \bar{u}_q \gamma_\mu u_q \quad (38)$$

$$J_\mu^{WNC,V} = \sum_q g_V^q \bar{u}_q \gamma_\mu u_q \quad (39)$$

$$J_\mu^{WNC,A} = \sum_q g_A^q \bar{u}_q \gamma_\mu \gamma^5 u_q, \quad (40)$$

where the indices  $WNC, V$  ( $WNC, A$ ) refer to the vector (axial-vector) contribution in the WNC, and the sum extends over all flavors of quarks:  $u, d, s, c, b$  and  $t$ . The term  $Q_q$  represents the EM lepton charge, and  $g_V^q$  ( $g_A^q$ ) the corresponding vector (axial-vector) charge in the weak sector.

In what follows we restrict the description of the hadronic states to the contribution of the three lightest quarks ( $u, d, s$ ).<sup>1</sup> In this case, the EM and WNC vector and axial-vector currents can be expressed in the form [52]

$$J_\mu^{EM} = J_\mu^{EM}(T=0) + J_\mu^{EM}(T=1) \quad (41)$$

$$J_\mu^{WNC,V} = \xi_V^{T=1} J_\mu^{EM}(T=1) + \sqrt{3} \xi_V^{T=0} J_\mu^{EM}(T=0) + \xi_V^{(0)} \hat{V}_\mu^{(s)} \quad (42)$$

$$J_\mu^{WNC,A} = \xi_A^{T=1} \hat{A}_\mu^{(3)} + \xi_A^{T=0} \hat{A}_\mu^{(8)} + \xi_A^{(0)} \hat{A}_\mu^{(s)}, \quad (43)$$

where we have separated the isoscalar and isovector EM currents and have made use of the SU(3) octet and singlet currents. In general we may write

$$J_\mu^{EM}(T=0) = [\bar{u}\gamma_\mu u + \bar{d}\gamma_\mu d - 2\bar{s}\gamma_\mu s] / 6 \quad (44)$$

$$J_\mu^{EM}(T=1) = [\bar{u}\gamma_\mu u - \bar{d}\gamma_\mu d] / 2 \quad (45)$$

$$\hat{A}_\mu^{(3)} = [\bar{u}\gamma_\mu\gamma_5 u - \bar{d}\gamma_\mu\gamma_5 d] / 2 \quad (46)$$

$$\hat{A}_\mu^{(8)} = [\bar{u}\gamma_\mu\gamma_5 u + \bar{d}\gamma_\mu\gamma_5 d - 2\bar{s}\gamma_\mu\gamma_5 s] / (2\sqrt{3}). \quad (47)$$

The terms  $\hat{V}_\mu^{(s)}$  ( $\hat{A}_\mu^{(s)}$ ) explicitly include the vector (axial-vector) currents between strange quarks:

$$\hat{V}_\mu^{(s)} \equiv \bar{s}\gamma_\mu s, \quad \hat{A}_\mu^{(s)} \equiv \bar{s}\gamma_\mu\gamma_5 s. \quad (48)$$

Finally, the  $\xi$  coefficients represent the coupling constants that can be written as

$$\xi_V^{T=1} = g_V^u - g_V^d = 2(1 - 2\sin^2\theta_W) [1 + R_V^{T=1}] \quad (49)$$

$$\sqrt{3}\xi_V^{T=0} = 3(g_V^u + g_V^d) = -4\sin^2\theta_W [1 + R_V^{T=0}] \quad (50)$$

$$\xi_V^{(0)} = g_V^u + g_V^d + g_V^s = - [1 + R_V^{(0)}] \quad (51)$$

$$\xi_A^{T=1} = g_A^u - g_A^d = -2 [1 + R_A^{T=1}] \quad (52)$$

$$\xi_A^{T=0} = \sqrt{3}(g_A^u + g_A^d) = \sqrt{3}R_A^{T=0} \quad (53)$$

$$\xi_A^{(0)} = g_A^u + g_A^d + g_A^s = 1 + R_A^{(0)}, \quad (54)$$

---

<sup>1</sup> The error introduced by neglecting the heavier quarks is expected to be of the order of  $10^{-4}$  ( $10^{-2}$ ) for the vector (axial-vector) currents [16, 37].

where we have included the radiative corrections  $R_{V,A}^{(a)}$  that are in general both  $Q^2$ - and process-dependent. These arise from higher-order elementary lepton-quark amplitudes, and we note that the effect of heavy quark current matrix elements, formally omitted in the previous expressions, may also be included in the  $R_{V,A}^{(a)}$  functions (see [52] for more details).

In the general expressions for the hadronic weak neutral currents in Eqs. (42,43), the physics associated with the electroweak gauge theory is contained into the coupling constants  $\xi$ , while hadronic effects emerge from the current matrix elements between quarks. Information on the various current matrix elements involved in the previous expressions can be obtained from different sources. PC electron scattering experiments provide a direct way to shed light on the purely EM (isoscalar and isovector) nucleon form factors. On the other hand,  $\beta$ -decay and semi-leptonic hyperon decay processes are sensitive to the axial-vector contribution in the weak interaction current. In this work, our interest focuses on the analysis of the strangeness current matrix elements and their effects on PV observables, *i.e.*, on the helicity asymmetry, and on the isovector axial-vector form factor.

The single-nucleon matrix elements of the electroweak currents, that are consistent with Lorentz covariance as well as parity and time-reversal invariance, are given through  $\bar{u}(P_f)\Gamma_a^\mu u(P_i)$  where  $u(P)$  are the single-nucleon wave functions properly normalized, and  $\Gamma_a^\mu$  are the corresponding EM and/or WNC current operators in Eqs. (20,21). Making use of the expressions given in Eqs. (42) and (43) for the WNC operators, the weak interaction nucleon form factors can be expressed in the general form

$$\tilde{G}_a(Q^2) = \xi_V^{T=1} G_a^{T=1} \tau_3 + \sqrt{3} \xi_V^{T=0} G_a^{T=0} + \xi_V^{(0)} G_a^{(s)}, \quad a = E, M \quad (55)$$

$$G_A^{e,N}(Q^2) = \xi_A^{T=1} G_A^{(3)} \tau_3 + \xi_A^{T=0} G_A^{(8)} + \xi_A^{(0)} G_A^{(s)} \quad (56)$$

with  $G_a^{T=0,1}$  the isoscalar and isovector combinations of the EM Sachs form factors of the nucleon,  $G_A^{(3,8)}$  the triplet and octet axial-vector form factors, and  $G_{E,M,A}^{(s)}$  the vector and axial-vector strange-quark form factors. At tree level, the following expressions apply to the nucleon WNC form factors:

$$\tilde{G}_{E,M}^{p,n} = (1 - 4 \sin^2 \theta_W) G_{E,M}^{p,n} - G_{E,M}^{n,p} - G_{E,M}^{(s)} \quad (57)$$

$$G_A^{e,N} = -2G_A^{(3)} \tau_3 + G_A^{(s)} = -(G_A^p - G_A^n) \tau_3 + G_A^{(s)}, \quad (58)$$

where the nucleon has been assumed to be an eigenstate of isospin. As shown, the WNC form factors of the nucleon are determined by the purely EM ones  $G_{E,M}^{p,n}$ , the axial-vector

$G_A^{e,N}$  and the terms  $G_{E,M,A}^{(s)}$  that only enter if the nucleon has non-zero strangeness content. Hence, in order to provide reliable analyses of PV electron scattering observables, excellent control of the EM structure of the nucleon is needed in addition to increasingly precise knowledge about the axial-vector form factors. In this situation, PV data can be safely used as a basic tool to determine how much strangeness enter in the nucleon structure. In what follows we present a systematic study of the nucleon form factors and discuss the large variety of prescriptions and models used in the literature.

### A. EM structure of the nucleon: $G_{E,M}^{p,n}$

The EM structure of the nucleon is one of the basic ingredients entering the description of lepton-nucleon scattering processes. Quantum Chromodynamics (QCD) is the fundamental theory of strong interactions; however, the complexity of the quark-gluon dynamics does not allow one to obtain analytical solutions of QCD in the energy regime relevant for low- $Q^2$  nuclear physics. Instead, various approaches based on numerical simulations of the theory on a lattice and/or through the use of effective hadron Lagrangians have been used.

As discussed above, in the case of free (on-shell) nucleons and the purely EM interaction, the hadronic structure is fully characterized by two functions: the electric ( $G_E^N$ ) and magnetic ( $G_M^N$ ) nucleon form factors (or alternatively  $F_{1,2}^N$ ), whose dynamical structure is given by their dependence on the only independent scalar variable in the scattering process, *i.e.*, the transferred four-momentum  $Q^2$ . It is important to point out that the description of nucleons in the nuclear medium, that is, off-shell nucleons, is much more complex: not only can the nucleon form factors depend explicitly on new independent dynamical variables in the process, but also the general structure of the EM hadronic current should include additional form factors (see [53–56] for details).

From the experimental point of view, most of the information at our disposal on the EM nucleon form factors comes from measurements of elastic electron-nucleon scattering. In the case of the proton, the use of hydrogen as a target has led to excellent determinations of the behavior of  $G_{E,M}^p$  (see [57–75]). In contrast, information on the neutron form factors is less precise because of the lack of free neutrons and thus the requirement to use nuclei as targets. Indeed, information on  $G_{E,M}^n$  comes mostly from analyses of scattering on light nuclear systems, such as deuterium and helium, typically exploiting polarization degrees of

freedom to isolate the form factors (see [76–103]).

Rosenbluth separations have been used for years to extract the contributions from the two elastic nucleon form factors in the cross section. However, this procedure presents important difficulties in the region of high  $|Q^2|$  because of the dominance of the  $G_M^2$  term and the very small (below 1% in some experiments at high  $|Q^2|$ ) contribution from  $G_E^2$ . More recently, the use of nucleon polarization techniques has permitted the extraction of interference effects that go as  $G_E G_M$  and hence provide relatively larger contributions. However, there still remain issues to be resolved that emerge from comparison of the results of different experiments, even in the regime of low- $Q^2$ . In Fig. 2 we show data on nucleon form factors from a large variety of analyses. We consider both electric (left panels) and magnetic (right) results for the proton (top panels) and the neutron (bottom). Data are compared with a large variety of models that are described below.

The internal dynamics of the nucleon is governed by the constituent quarks and the exchanged gluons that, for instance, may be simulated using lattice-QCD. Alternatively, approaches based on phenomenology and/or simplified models may be invoked. All of these approaches should be consistent with the behavior of the form factors at the limits where one can be sure of the answers. In the static limit, *i.e.*,  $Q^2 = 0$ , the EM nucleon form factors should give the correct values for the charge and magnetic moment of the nucleon:

$$\begin{aligned} G_E^p(0) &= 1, & G_M^p(0) &= \mu_p = 2.793, \\ G_E^n(0) &= 0, & G_M^n(0) &= \mu_n = -1.913. \end{aligned} \tag{59}$$

In the opposite extreme, at very high  $|Q^2|$ , the asymptotic behavior of the nucleon form factors can be obtained using perturbative QCD (pQCD). These yield  $F_1$  dependent on  $Q^{-4}$  and  $F_2 \sim F_1/Q^2$ . Once the behavior of  $G_{E,M}$  in the extreme situations is fixed, the specific dependence with the four-momentum transfer at small-intermediate values is required. In what follows we present different models, some of them widely used in the literature, and compare their predictions with available data. To make the discussion simpler, we have considered models in two basic categories, phenomenology and Vector Meson Dominance (VMD).

- **Phenomenological Models.**

Within this category, one may consider the Galster dipole parameterization that makes use of the following functional dependence:  $G_E^p = G_D^V$ ,  $G_E^n = -\mu_n \tau G_D^V \xi_n$ ,  $G_M^p = \mu_p G_D^V$

and  $G_M^n = \mu_n G_D^V$ , with  $G_D^V = (1 + \lambda_D^V \tau)^{-2}$  and  $\xi_n = (1 + \lambda_n \tau)^{-1}$ . We consider the standard values of the parameters:  $\lambda_D^V = 4.97$ ,  $\lambda_n = 5.6$ ,  $\mu_p = 2.79$  and  $\mu_n = -1.91$ . This model, still used in the literature, provides a reasonable description of proton data at  $|Q^2| \leq 1$  (GeV/c)<sup>2</sup> ( $\sim 5\%$ ). In the case of the neutron, the description is significantly less precise because of data uncertainties.

In this work we have considered two relatively new prescriptions developed by Kelly [104] and Arrington and Sick [105] (denoted A-S). In particular, the prescription developed by Kelly constitutes an extension of the Galster parameterization, providing a reasonable description of recent data taken from polarization measurements. Within this model, the electric and magnetic form factors of the proton, together with the neutron magnetic form factor, are given by the general function:

$$G(Q^2) \propto \frac{\sum_{k=0}^1 a_k \tau^k}{1 + \sum_{k=1}^3 b_k \tau^k}, \quad (60)$$

where  $a_0 = 1$  and the rest of parameters are given in Table I.

In the case of the electric form factor of the neutron, the Galster parameterization as given in [106] is used, *i.e.*,

$$G_E^n(Q^2) = \frac{A\tau}{1 + B\tau} G_D(Q^2), \quad (61)$$

with  $A$  and  $B$  as given in Table I and  $G_D(Q^2) = (1 + |Q^2|/\Lambda^2)^{-2}$  with  $\Lambda^2 = 0.71$  (GeV/c)<sup>2</sup>.

F.F.	$a_1$	$b_1$	$b_2$	$b_3$	$A$	$B$
$G_E^p$	$-0.24 \pm 0.12$	$10.82 \pm 0.19$	$12.82 \pm 1.1$	$21.97 \pm 6.8$		
$G_M^p/\mu_p$	$0.12 \pm 0.04$	$10.97 \pm 0.11$	$18.86 \pm 0.28$	$6.55 \pm 1.2$		
$G_M^n/\mu_n$	$2.33 \pm 1.4$	$14.72 \pm 1.7$	$24.20 \pm 9.8$	$84.1 \pm 41$		
$G_E^n$					$1.80 \pm 0.04$	$3.30 \pm 0.32$

TABLE I: Values of the parameters in the Kelly prescription [104].

The parametrizations of the form factors provided by A-S include the effects of the two-photon exchange corrections to the extracted EM form factors. This representation applies to momentum transfers up to  $|Q| \equiv \sqrt{|Q^2|} = 1$  GeV/c, and makes use of a

continued fraction (CF) expansion in the form,

$$G_{CF}(Q) = \frac{1}{1 + \frac{b_1 Q^2}{1 + \frac{b_2 Q^2}{1 + \dots}}}, \quad (62)$$

where different values for the fit parameters  $b_i$  are used for the EM proton and neutron form factors. In the particular case of  $G_E^n$  a modified three-parameter CF expansion is considered:  $G_E^n(Q) = 0.484 \times Q^2 \times G_{FC}$  with  $Q^2$  given in  $(\text{GeV}/c)^2$ .

- **Models based on Vector Meson Dominance (VMD).**

A more fundamental representation of the nucleon form factors can be obtained from models based on Vector Meson Dominance (VMD). Here, the virtual photon is assumed to be transformed into a neutral vector meson that couples to the corresponding hadron (see [107] for details). Thus, the nucleon form factors are expressed in terms of meson propagators and meson-nucleon form factors. Within this framework a variety of descriptions of the EM nucleon form factors have been presented in the literature. Some of the most representative cases are: i) Höhler [108], based on the use of dispersion relations to obtain the contribution of the  $\pi\pi$  continuum, fitting the width of the  $\rho$  meson with a simple function of the mass, and representing the  $\omega$  and  $\phi$  mesons by simple poles, and ii) Gari-Krumpelmann [109] that incorporates the high- $|Q^2|$  behavior as provided by pQCD using differing convergence rates of hadronic and quark form factors. The use of dispersion relations in the analysis of isoscalar vector current nucleon form factors has been considered in [110, 111]. In particular, the authors in [111] include explicitly the continuum  $K\bar{K}$  contribution in refitting the isoscalar EM form factors, and conclude that a naive VMD approach represents an effective parametrization, but leads to erroneous values of the  $\phi$ -nucleon resonance couplings. This also has implications for the nucleon's strange vector form factors.

Within the general framework of VMD models, in this work we present results corresponding to two of the most recent descriptions provided in the literature. On the one hand, we employ the model denoted GKex [112–114] developed by Lomon and collaborators whose validity extends to a wide range in the transferred momentum. This model is a generalized description of the original GK prescription, incorporating in addition to the asymptotic pQCD behavior, effects due to the vector mesons  $\rho$ ,  $\rho'$ ,  $\omega$ ,  $\omega'$  and  $\phi$  and including a width for the  $\rho$ . On the other hand, we also

consider the model developed by Beluskin, Hammer and Meißner [115] (BHM model) that is an extension of the Höhler-type model. In addition to the dispersion relations some constraints are also incorporated into the model, namely, contributions to the continuum coming from  $\pi\pi$ ,  $K\bar{K}$  and  $\rho\pi$ , and asymptotic convergence at high  $|Q|^2$ . Two basic approaches concerning the dynamical dependence on  $|Q^2|$  at high values (pQCD behavior) are used: i) SuperConvergence approach (denoted here as BHM-SC) and ii) explicit pQCD continuum approach (BHM-pQCD). In the former the asymptotic behavior is obtained by choosing the residues of the vector meson pole terms in such a way that a spectral function consistent with asymptotic behavior emerges (see [115] for details). The latter approach explicitly enforces the pQCD behavior, and it is consistent with a nonvanishing imaginary part of the form factors in the timelike region.

In Fig. 2 we present the EM nucleon form factors versus  $|Q^2|$  for all of the models described above, and compare them with data. As shown, all prescriptions provide reasonable descriptions of data at low  $|Q^2|$ , with a relatively small dispersion between the different curves. On the contrary, for increasing values of the transferred momentum the differences between the models go up significantly. This is in particular the case for the A-S prescription whose value for  $G_E^p/G_D$ , with  $G_D$  the standard dipole form, starts to grow rapidly for  $|Q^2| \geq 2$  (GeV/c)<sup>2</sup> whereas the other models lead to decreasing  $G_E^p/G_D$ . In contrast, the other models are reasonably successful at representing the data above 1.8 (GeV/c)<sup>2</sup> taken from polarization measurements. Note, however, that the A-S parameterization was only designed to be used when  $|Q^2| \leq 1$  (GeV/c)<sup>2</sup>.

In the case of  $G_M^p$  (right-top panel), data have been measured for a momentum transfer range that is significantly greater than for the other form factors. As shown, the ratio  $G_M^p/(\mu_p G_D)$  is relatively close to unity until  $|Q^2| \sim 1$  (GeV/c)<sup>2</sup>. Then, it increases and reaches its maximum in the region  $\sim 3-5$  (GeV/c)<sup>2</sup> before decreasing rapidly for  $|Q^2| > 7$  (GeV/c)<sup>2</sup>. All prescriptions reproduce the general behavior of data out to very high values of  $|Q^2|$ , with the exception of the A-S prescription (again, only to be used when  $|Q^2| < 1$  (GeV/c)<sup>2</sup>). Also noteworthy is that the BHM-pQCD model clearly overestimates data located at  $|Q^2|$ -values where the maximum is reached.

As already mentioned in previous paragraphs, the extraction of the neutron form factors from electron-deuteron and electron-<sup>3</sup>He scattering leads to greater uncertainties and a more

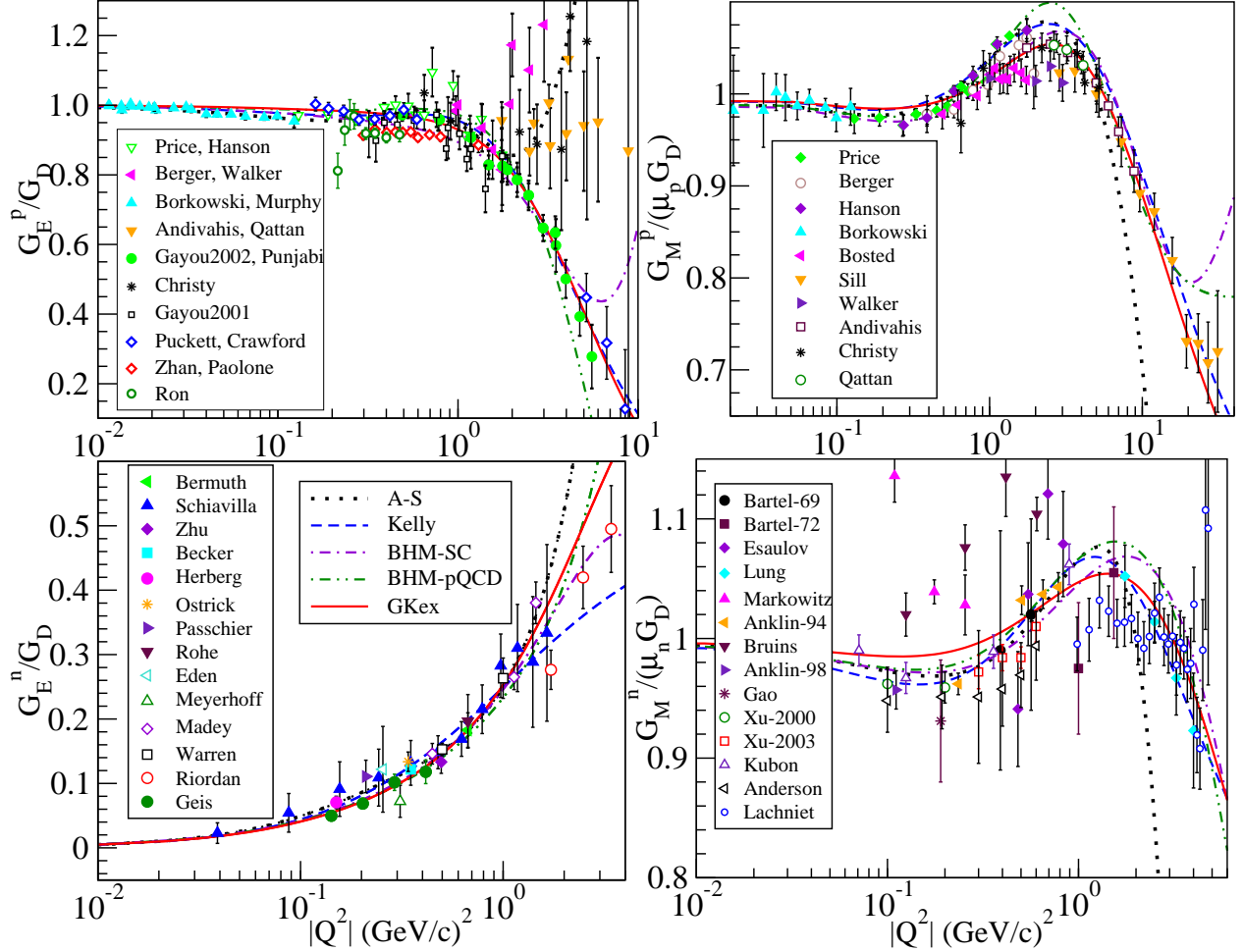


FIG. 2: (Color online) EM nucleon form factors obtained using different descriptions compared with data. The proton electric form factor (top-left panel) corresponding to Gayou2002, Gayou2001, Punjabi, Puckett, Zhan, Ron, Paolone and Crawford have been obtained from  $R_p$  data by dividing by the GKex model values of  $G_M^p/\mu_p$ . The same applies to Geis in the case of the electric neutron form factor (left-bottom), but using the GKex model  $G_M^n/\mu_n$ . The data are taken from references [57–103].

restricted momentum transfer range. This is clearly illustrated in the bottom panels shown in Fig. 2. In the case of the magnetic contribution to the neutron, the data scatter significantly in the region below  $1 (\text{GeV}/c)^2$ . The five models presented track the average of the scattered data in this region, fitting the higher- $|Q^2|$  behavior, except for the A-S prescription that falls much faster. Finally, data for  $G_E^n/G_D$  are presented in the left-bottom panel compared with the five prescriptions considered. Here, data derived from different polarization techniques as well as values obtained from analysis of the deuteron quadrupole form factor data [84] are

plotted. From comparison with theory we observe that all prescriptions provide reasonable descriptions of data up to  $\sim 1$   $(\text{GeV}/c)^2$ . For higher  $|Q^2|$  the models start to deviate, even changing the slope of the curve for the BHM-SC case.

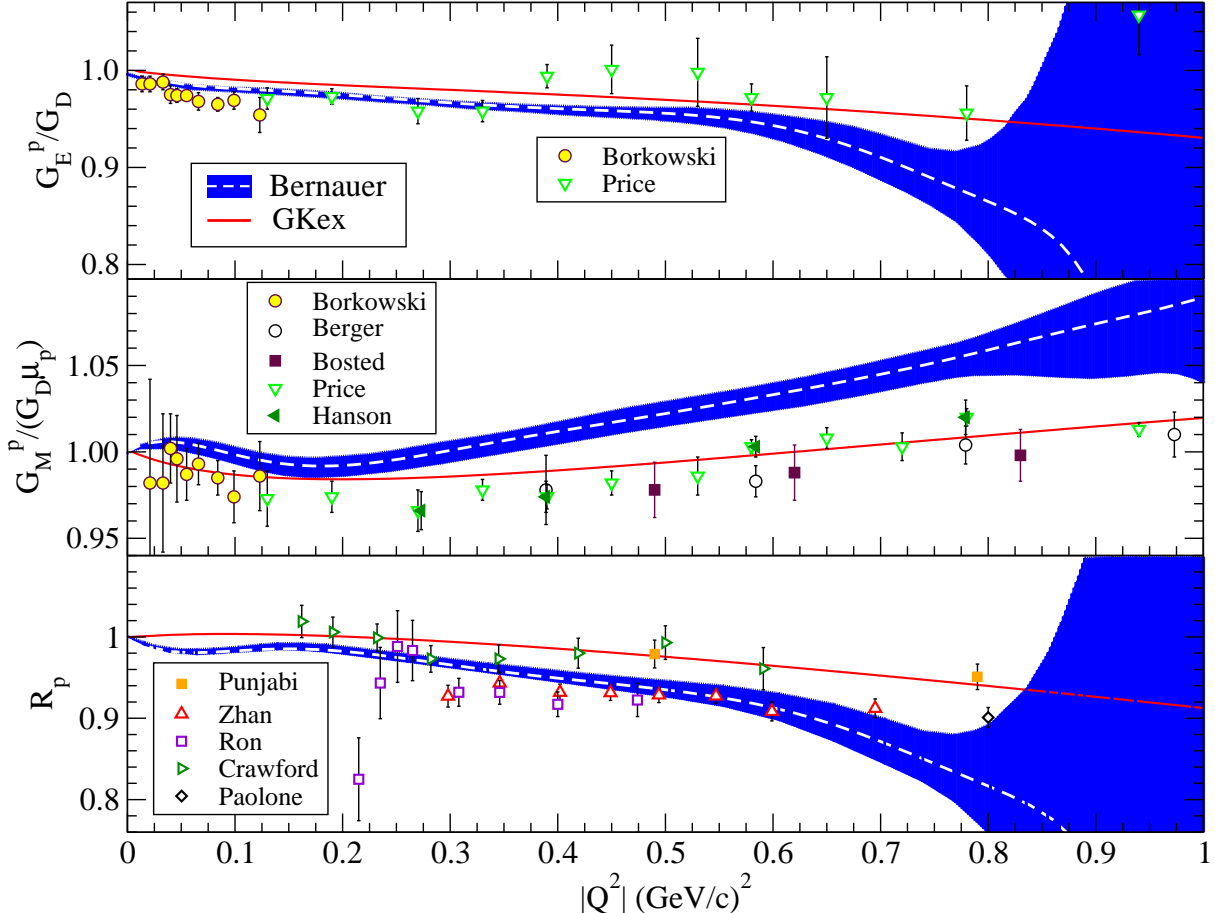


FIG. 3: (Color online) EM nucleon form factors from different experiments (see Fig. 2 for references) are compared with the GKex model and with the data of Bernauer *et al.* [116] (see text for details).

To complete the discussion of the EM form factors we present in Fig. 3 the analysis recently performed by Bernauer *et al.* [116], where about 1400 elastic electron-proton cross sections were measured with four-momentum transfers up to  $|Q^2| \sim 1$   $(\text{GeV}/c)^2$ . The dashed white lines in Fig. 3 represent the best fits to these data, whereas the blue shadowed areas include the statistical and experimental systematic errors plus effects coming from Coulomb corrections (see [116] for details). We compare these data with the results provided by the GKex model (red line). To make the discussion that follows easier, we also include in the graph data coming from experiments based on Rosenbluth separations in the two upper panels and data from polarization experiments in the bottom panel, both already shown in

Fig. 2.

The proton electric form factor normalized to the dipole form is presented in the top panel. We notice that GKex slightly overestimates the behavior of the data of Bernauer *et al.*, but it reproduces older Price measurements [57]. It is important to point out that for transfer momenta below  $0.7 \text{ (GeV/c)}^2$  the discrepancy between GKex and the data of Bernauer *et al.* and Borkowski *et al.* [60] is on average less than  $\sim 2\%$ . The results for the proton magnetic form factor are presented in the middle panel. In this case, the GKex model fits nicely data coming from the older experiments, but it underestimates the new analysis performed by Bernauer *et al.*; the difference is of the order of  $\sim 4\%$  at  $|Q^2| = 0.7 \text{ (GeV/c)}^2$ . Finally, the bottom panel in Fig. 3 shows the ratio  $R_p = \mu_p G_E^p / G_M^p$ . We display the most recent data presented in the literature, Paolone *et al.*, [71], Zhan *et al.* [72] and Ron *et al.* [73]. As shown, they are in accord with the analysis of Bernauer *et al.* but differ from previous experiments, namely those of Punjabi *et al.* [67] and Crawford *et al.* [70]. At  $|Q^2| = 0.7 \text{ (GeV/c)}^2$  the difference is about  $\sim 6\text{-}7\%$ . In Sect. IV A the consequences of using the results of Bernauer *et al.* for the EM form factors, rather than the GKex model fit to the older data, in obtaining the PV asymmetry are examined.

Summarizing, discrepancies between data taken in different experiments and the results provided by the GKex model are below  $\sim 6\text{-}7\%$  in the range  $|Q^2| \leq 0.7 - 0.8 \text{ (GeV/c)}^2$ .

For completeness, we present in Fig. 4 the results corresponding to the electroweak vector nucleon form factors,  $\tilde{G}_{E,M}$ , for the different EM descriptions considered. In all cases strangeness content in the nucleon has not been included, but the radiative corrections  $R_V^{(a)}$  entering in the electroweak vector coupling constants (Eqs. (49-51)) have been incorporated assuming the general expressions

$$R_V^{T=0} = \frac{R_V^n - (1 - 4 \sin^2 \theta_W) R_V^p}{4 \sin^2 \theta_W}, \quad (63)$$

$$R_V^{T=1} = \frac{(1 - 4 \sin^2 \theta_W) R_V^p + R_V^n}{2(1 - 2 \sin^2 \theta_W)} \quad (64)$$

with  $R_V^p = -0.0520$ ,  $R_V^n = -0.0123$  and  $R_V^{(0)} = -0.0123$  [117, 118], this last term not contributing to results in Fig. 4 because it only enters with strangeness  $G_{E,M}^{(s)}$  different from zero.

In the present study we follow closely the arguments already presented in [117] where a global analysis of experimental data from elastic PV electron scattering at low- $Q^2$  was given.

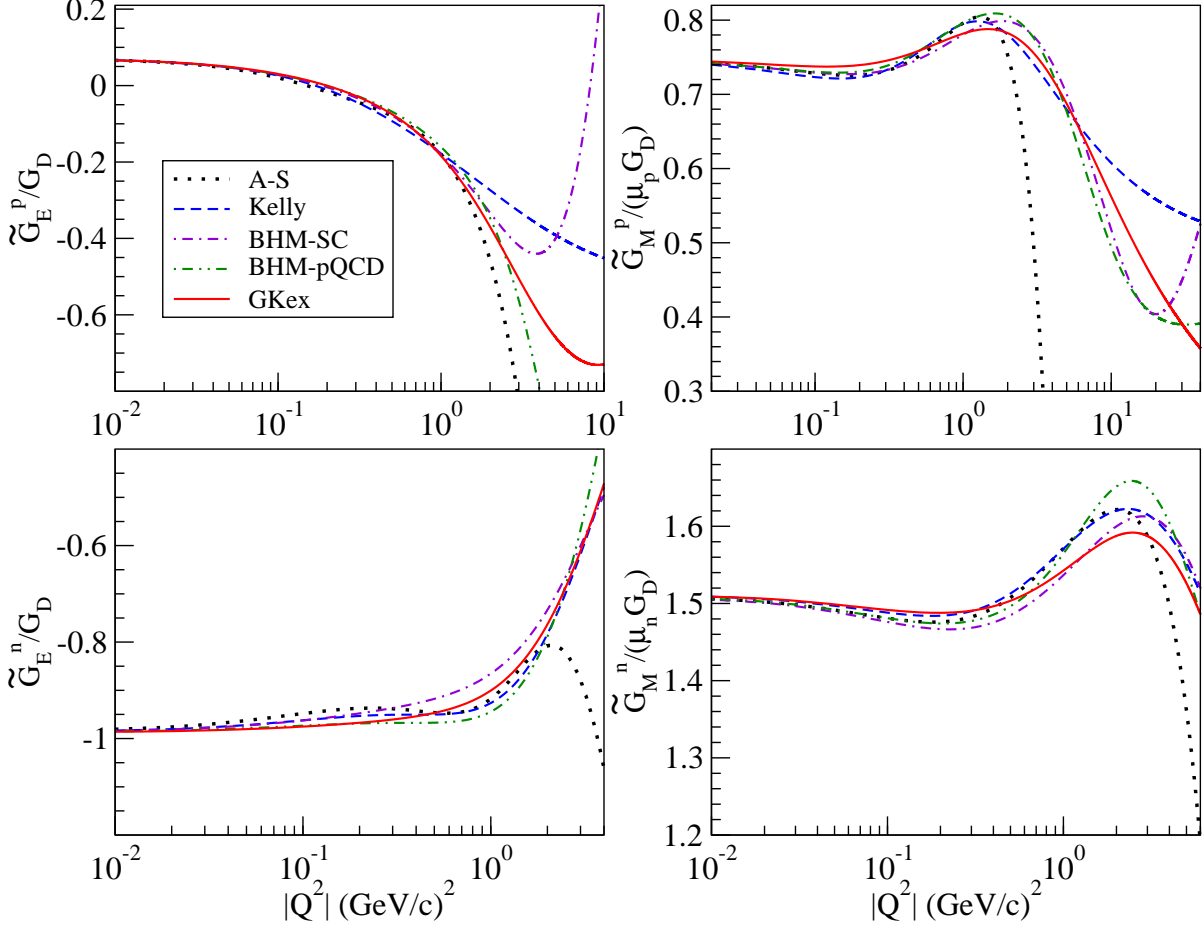


FIG. 4: (Color online) Electroweak form factors obtained with the different prescriptions analyzed in this work. Zero strangeness has been assumed here.

Contributions from perturbative QCD and coherent strong interaction effects in the radiative corrections associated with elastic nucleon scattering have been evaluated in [119, 120], providing also an improved estimate of the running of the weak mixing angle in the  $\overline{\text{MS}}$  renormalization scheme. All of these effects are included in the  $R_V$ -values shown above (see table I in [117]). As explained in [117], the theoretical uncertainties in  $R_V^n$  and  $R_V^{(0)}$  are less than 1%, and hence have a negligible impact on the analysis presented in this work. On the other hand, the theoretical error in the full expression  $(1 - 4 \sin^2 \theta_W)(1 + R_V^p)$  is slightly more than 1% (see [120]). In this work we use the conventional  $\overline{\text{MS}}$  renormalization scheme, and the weak mixing angle,  $\sin^2 \theta_W$ , used in the evaluation of the PV asymmetry results that are discussed in the next section, which takes on the value  $0.23122 \pm 0.00015$  in accordance with the arguments presented in [117, 121]. The use of a different  $\theta_W$ -value, for instance the running  $\sin^2 \theta_W(0)$  given in [120], leads to differences in the PV analysis that will be

considered briefly in the next section.

As shown, results for  $\tilde{G}_{E,M}^{p,n}$  provided by the five prescriptions are very similar for  $|Q^2| \leq 1$  (GeV/c)<sup>2</sup>. This is consistent with the general behavior presented in Fig. 2. On the contrary, the spread gets wider as  $|Q^2|$  increases. In general, comments already applied to the analysis of the purely EM form factors can be also extended here, but changing the isospin channel. Notice that the electroweak electric and magnetic form factors for the proton (neutron) are basically determined by the corresponding EM ones for the neutron (proton), *i.e.*,  $\tilde{G}_{E,M}^{p,n} \simeq G_{E,M}^{n,p}$ .

### B. Axial-vector nucleon form factor: $G_A^e$

The neutral current axial-vector form factor for a nucleon, which is directly linked to the weak interaction in electron scattering, can be decomposed into its isovector, singlet and octet axial-vector strangeness contributions,

$$G_A^{e,N} = \xi_A^{T=1} G_A^{(3)} \tau_3 + \xi_A^{T=0} G_A^{(8)} + \xi_A^{(0)} G_A^{(s)} \quad (65)$$

which may be recast into isoscalar, isovector and strangeness contributions. In contrast to the EM and WNC vector currents, the axial-vector current is not conserved, and hence the value of the axial-vector nucleon form factor at  $Q^2 = 0$  is not restricted by any exact symmetry. However, the term  $G_A^{(3)}(0)$  can be determined from Gamow-Teller  $\beta$ -decay, and analogously, information on  $G_A^{(8)}$  can be obtained combining data from neutron and hyperon  $\beta$ -decay measurements, assuming isospin invariance. In general, we may write:  $G_A^{(3)}(0) = (D + F)/2$  with  $D + F \equiv g_A$ , and  $G_A^{(8)}(0) = (3F - D)/(2\sqrt{3})$ . The terms  $F$  and  $D$  represent the matrix elements of the axial weak current for the states of different hyperons belonging to the SU(3) octet [37, 52, 122]).

Concerning the dynamical structure of  $G_A^e$ , *i.e.*, its dependence on  $Q^2$ , the usual procedure is to parametrize data making use of the standard dipole form:  $G_A^{(3,8)}(Q^2) = G_A^{(3,8)}(0) G_D^A(Q^2)$  with  $G_D^A(q^2) = (1 + |Q^2|/M_A^2)^{-2}$  and  $M_A = (1.032 \pm 0.036)$  GeV the axial-vector mass whose standard value comes from the analysis of charged-current quasielastic (CCQE) neutrino scattering processes (see [123–126]).

Some recent studies [117] (see also [11, 52]) have addressed the importance of including radiative corrections in the axial-vector term. An expression for the axial-vector form

factor [117] can be written as follows:

$$G_A^{e,p}(Q^2) = - \left[ g_A(1 + R_A^{T=1}) - \frac{3F - D}{2} R_A^{T=0} - \Delta_S(1 + R_A^{(0)}) \right] G_D^A(Q^2), \quad (66)$$

where the dependence of the axial-vector strange form factor on  $Q^2$  is also assumed to follow a dipole form. The values of the various parameters that have been used in this work are given in Table II. The ratios  $R_A^{T=1}$ ,  $R_A^{T=0}$  and  $R_A^{(0)}$  provide the effects of electroweak radiative corrections to the isovector, isoscalar and SU(3) singlet hadronic axial vector amplitudes, respectively. The terms  $R_A^{T=1,0}$  account for *one-quark* and *many-quark* contributions. The former correspond to the renormalization of the effective weak couplings,  $C_{2q}$ , and their values can be obtained from the SM predictions for these couplings. The latter, *i.e.*, many-quark contributions, include the *anapole* effects [127] as well as coherent strong interaction contributions. Contrary to the vector corrections,  $R_V$ , the importance of the many-quark effects in the  $R_A$  can be significant [117, 118].

Studies of the anapole form factor and its potential impact on the strangeness current have been presented in the past [128, 129]. In particular, the authors in [130, 131] evaluate the anapole form factor of the nucleon in chiral perturbation theory to sub-leading and leading order. The kinematic region considered is  $Q \equiv \sqrt{|Q^2|} \ll M_{QCD}$ , where  $M_{QCD}$  ( $\sim 1$  GeV) is the typical mass scale in QCD. In this regime a systematic expansion of the form factor in powers of  $Q/M_{QCD}$  is feasible, and the momentum dependence of the anapole form factor was presented in [130, 131]. Although its inclusion in the analysis of PV electron scattering on the nucleon should be valuable, the study presented in this work covers a  $Q^2$ -range large enough where the validity of the expansion in [130, 131] might be questionable. Furthermore, the uncertainty in the axial form factor, described through the use of different values for the axial mass, could make it difficult to isolate other residual contributions.

In addition to the standard dipole form considered for the dependence of  $G_A^{e,p}$  with the transferred momentum, it is also interesting to analyze the results when using a monopole form. This is motivated by VMD-based analyses such as those in [112, 113] and summarized in [114] where one finds for the EM form factors that it is more natural to have monopole behavior rather than dipole behavior, the latter arising from cancelations between the contributions of the particular vector mesons. Such cancelations cause the magnetic form factors  $G_M^p$  and  $G_M^n$  to be essentially dipole-like at small momentum transfers, but do not enter the same way for  $G_E^p$  and, in fact, the current understanding is that the electric form factors

	$R_A^{T=1}$	$R_A^{T=0}$	$R_A^{(0)}$
One-quark	-0.172	-0.253	-0.551
Many-quark	-0.086(0.34)	0.014(0.19)	N/A
Total	-0.258(0.34)	-0.239(0.20)	-0.55(0.55)

Parameters	Values
$g_A$	1.2695
$3F - D$	0.58(0.12)
$\Delta s$	-0.07(0.06)

TABLE II: Values of the parameters included in Eq. (66) (see [117, 118]). The top panel includes the one-quark [121] and many-quark [127] corrections to the axial charges. In the bottom panel we give the isovector axial form factor at zero momentum transfer,  $g_A$  (see [132–134]), the SU(3) reduced matrix elements,  $3F - D$ , taken from [135], and the strange quark contribution to the nucleon spin,  $\Delta s$  [136].

falls faster than a standard dipole. For the axial-vector form factor, and for the strangeness form factors discussed in the next section, the picture may be different: the cancelations that lead to dipole-like behavior may or may not occur and the “standard” assumption that a dipole form is the correct one to choose may not be warranted. Accordingly we have investigated what might change if monopoles rather than dipoles are assumed. In this case, the dependence is given through the function:

$$G_M^A(Q^2) = (1 + |Q^2|/\widetilde{M}_A^2)^{-1} \quad (67)$$

with  $\widetilde{M}_A$  being the monopole axial-vector mass introduced in a similar way to the dipole one  $M_A$ .

In Sect. IV B we analyze in detail the effects introduced in the PV asymmetry by the dipole versus monopole description of the axial-vector form factor by using different values for the axial-vector masses  $M_A$  and  $\widetilde{M}_A$ . Radiative corrections will also be explored in Sect. IV D. Finally, concerning the strangeness content in  $G_A^{e,p}$ , one finds that the PV asymmetry does not show much sensitivity to  $G_A^{(s)}$ , and hence in this work all results presented correspond to axial-vector strangeness as given in Table II (see [117, 118]).

### C. Nucleon vector form factors with strangeness: $G_{E,M}^{(s)}$

Our present knowledge about the strange vector nucleon form factors is much more limited than for the form factors discussed above although some general considerations can be made. Since the nucleon does not present any net strangeness, the strange electric form factor in the static limit, *i.e.*,  $Q^2 = 0$ , should fulfill the constraint  $G_E^{(s)}(0) = F_1^{(s)}(0) = 0$ . Analogously, the strangeness magnetic moment is given by the corresponding form factor in the limit  $Q^2 \rightarrow 0$ :  $\mu_s \equiv F_2^{(s)}(0) = G_M^{(s)}(0)$ . With regards to the functional dependence with the transferred four-momentum, the standard procedure is to consider the usual dipole form<sup>2</sup>

$$G_E^{(s)}(Q^2) = \rho_s \tau G_D^V(Q^2) \quad (68)$$

$$G_M^{(s)}(Q^2) = \mu_s G_D^V(Q^2) \quad (69)$$

with  $G_D^V(Q^2) \equiv (1 + |Q^2|/M_V^2)^{-2}$  and  $M_V$  the vector-mass parameter. The term  $\rho_s$  is given by the derivative of the electric strangeness nucleon form factor with respect to  $\tau$  evaluated at  $\tau = 0$ , *i.e.*,  $\rho_s \equiv dG_E^{(s)}/d\tau|_{\tau=0}$ . A detailed study of  $\rho_s$  and  $\mu_s$  and their influence on the scattering observables will be presented in the next section.

For completeness, following the arguments given above for the axial-vector form factor, a functional dependence of  $G_{E,M}^{(s)}$  with  $Q^2$  based on a monopole form will be also explored in the analysis of results. Thus, instead of using the function  $G_D^V(Q^2) = (1 + |Q^2|/M_V^2)^{-2}$  in Eqs. (68,69) we will also consider the functional dependence:  $\tilde{G}_M^V(Q^2) = (1 + |Q^2|/\tilde{M}_V^2)^{-1}$  where different values of the monopole vector mass  $\tilde{M}_V$  will be considered.

## IV. PARITY-VIOLATING ASYMMETRY: ANALYSIS OF RESULTS

In this section we present a systematic analysis of the PV asymmetry for elastic electron-proton scattering. As already mentioned, all results have been evaluated in the one-boson-exchange approximation. Different kinematical regimes including backward and forward scattering angles are considered. This study makes it possible to compare our predictions with a large variety of data, also showing the contribution in the asymmetry  $\mathcal{A}^{PV}$  coming from the separate electric, magnetic and axial-vector form factors.

---

<sup>2</sup> In some previous work [52, 137] additional functions  $\xi_{E,M}^{(s)}$  depending on  $Q^2$  were introduced; however, to make the discussion that follows simpler here we consider only  $\xi_{E,M}^{(s)} = 1$ .

The various ingredients entering the description of the process, *i.e.*, the EM and WNC structure of the proton, and their effects on  $\mathcal{A}^{PV}$  are analyzed. In particular, the description of the axial-vector form factor with its functional dependence on the transferred momentum, dipole versus monopole, and the specific value of the axial-vector mass are carefully investigated. Finally, we discuss at length how the strangeness content in the nucleon can modify  $\mathcal{A}^{PV}$ . This is one of the basic objectives in the study of PV electron scattering reactions due to the particular sensitivity shown by the PV asymmetry to the  $\bar{s}s$  content in the nucleon. In this work we present an exhaustive analysis, isolating the contribution of strangeness in the three channels involved in the process, electric, magnetic and axial-vector. We compare the results obtained with all available data, these spanning a range in  $|Q^2|$  up to 1 (GeV/c)<sup>2</sup>.

Before entering into a detailed discussion of the results obtained, here we comment on effects beyond the Born approximation. In particular, we focus on the corrections associated with two-photon exchange (TPE), since these can be of the same order as effects from the  $\gamma - Z$  interference term. We already presented some discussion on this topic in the introduction, with particular emphasis on the description of the EM form factors where effects due to these higher-order corrections have been estimated.

A renewed interest in the TPE mechanism in elastic electron-proton scattering emerged from the discrepancy between data at high- $Q^2$  for the electric and magnetic proton form factors as measured in unpolarized (Rosenbluth separation) and polarized electron scattering. Several studies suggested that this discrepancy could be explained by higher-order contributions and both theoretical and phenomenological analyses have been presented in the literature (for a general review see [138, 139]). The elastic EM form factors of the proton have been extracted using different parameterizations that account for two-photon interference effects. This is the case of [140] (and refs. therein) where differences up to the order of  $\sim 10\%$  were observed (increasing in size as  $Q^2$  goes up). These results were also compared with phenomenological extractions and direct calculations, showing similar results for several kinematics. A different approach to TPE was presented in [141], where the focus was on the large momentum transfer region, and the leading  $2\gamma$  amplitude was evaluated in terms of the leading twist nucleon distribution amplitudes; the claim made there is that the TPE contributions in fact go as  $Q^{-4}$ .

The implications of TPE for elastic PV electron scattering have been analyzed in previous work [105, 142]. In [142] higher-order corrections are obtained within the framework of the

parton model, making use of generalized parton distributions. TPE are shown to lead to a correction that depends on both  $Q^2$  and  $\varepsilon$  (see Eq. (33)) reaching an increase in the PV asymmetry of the order of  $\sim 1\%$  compared with its Born value. This effect results in about the same percentage decrease in the magnitude of the weak magnetic proton form factor.

A systematic study of the EM nucleon form factors including effects coming from TPE corrections was presented in [105]. This analysis is extended up to  $|Q^2| \sim 1.2$  (GeV/c)<sup>2</sup> and incorporates the effect of the two-photon box diagrams, but not the effect of the  $\gamma - Z$  box that will be commented upon later. The authors in [105] provide fits to the form factors accounting for TPE contributions, concluding that such higher-order effects in the PV asymmetry, due to cancelation between different terms, are less than 1% for  $|Q^2| < 1$  (GeV/c)<sup>2</sup>. In the next section we show results for the PV asymmetry obtained using the general prescription for the EM form factors provided in [105].

Despite the previous discussion, it is important to point out that the role played by TPE is not yet a settled issue and three experiments [143–145] are aimed at gaining some insight by studying (PC) electron-proton versus positron-proton scattering. Some initial results from Novosibirsk indicate that the box and cross-box (hard) contributions may be smaller than expected. Hence, some caution should be expressed on how precisely we are presently able to assess the impact of the TPE effects.

To conclude these brief discussions, let us point out that isospin breaking effects have recently been studied for PV electron scattering on nucleons [19] and <sup>4</sup>He [20] (see also [51, 146] for discussions of isospin mixing in PC electron scattering). The authors in [19, 20] find isospin violations to be smaller than strangeness uncertainties. However, these corrections may play a role in the case of global data analyses, particularly at increasing  $|Q^2|$ -values. As already mentioned, in this work we assume isospin symmetry; however, it should be noted that the strange form factors have sufficiently strong dependencies on the transferred four-momentum that, within their uncertainties, they cover the potential impact of isospin breaking at the kinematics of interest in this work.

### A. Dependence on EM nucleon structure

Here our aim is to analyze the sensitivity of the PV asymmetry to the particular description chosen for the EM form factors. Results are shown in Fig. 5 where we present  $|\mathcal{A}^{PV}|$

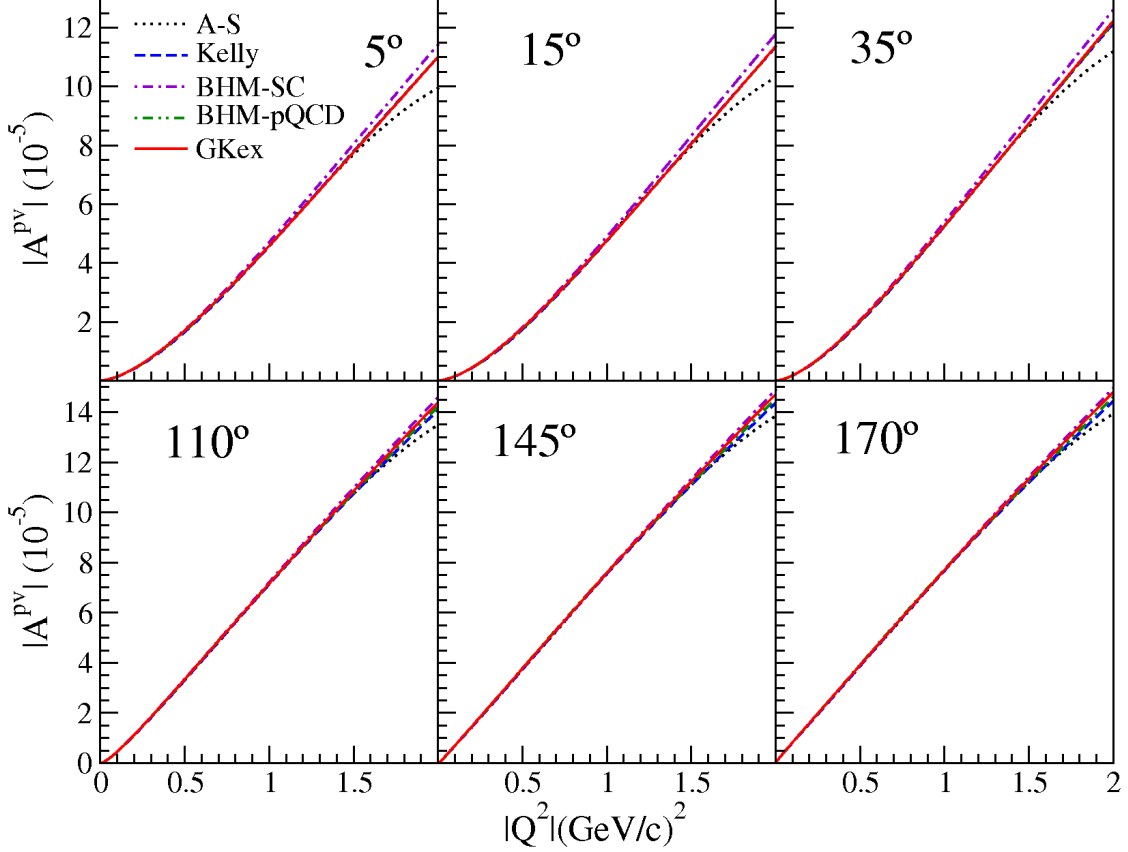


FIG. 5: (Color online) Absolute value of the PV asymmetry as a function of  $|Q^2|$ . Results are presented for six scattering angles and the five prescriptions considered in the previous section for the EM nucleon form factors. Radiative corrections according to Eq. (64) have been included, but nucleon strangeness is neglected here.

versus  $|Q^2|$  for six values of the scattering angle that range from very forward ( $\theta_e = 5^\circ$ ) to very backward ( $170^\circ$ ) kinematics. These include the regimes where different experiments have been performed (see discussion in next sections). For simplicity, all results in Fig. 5 have been evaluated assuming no strangeness in the nucleon and the five prescriptions for the EM nucleon form factors presented in Fig. 2 have been considered, namely, A-S (dotted line), Kelly (dashed), BHM-SC (dot-dashed), BHM-pQCD (double-dot-dashed) and GKex (solid). Only results based on the A-S model clearly depart from the others for  $|Q^2|$ -values above 1.5  $(\text{GeV}/c)^2$ . For  $|Q^2|$  above 2  $(\text{GeV}/c)^2$  (not shown in the graph) this discrepancy gets much larger, *i.e.*, consistent with the behavior shown by  $G_{E,M}^{p,n}$  in Fig. 2 (likewise for the electroweak form factors in Fig. 4). As noted earlier, A-S only applies to  $|Q^2| \leq 1$   $(\text{GeV}/c)^2$ .

Concerning the four remaining prescriptions, Kelly, GKex, BHM-SC and BHM-pQCD,

they yield very similar results for all transferred momentum values. The discrepancy is at most of the order of  $\sim 3\text{--}4\%$  at the limit  $|Q^2| = 2 \text{ (GeV/c)}^2$  and is very similar for all scattering angles. At  $|Q^2| = 1 \text{ (GeV/c)}^2$  (the limit in the experimental data for the asymmetry) the dispersion between the four prescriptions is about  $\sim 3\%$  in the very forward case ( $\theta_e = 5^\circ$ ), and gets much smaller for larger angles. In the most backward-angle kinematics, *i.e.*,  $\theta_e = 170^\circ$ , the dispersion is less than  $\sim 0.7\%$ . These differences are even smaller for decreasing transferred momenta.

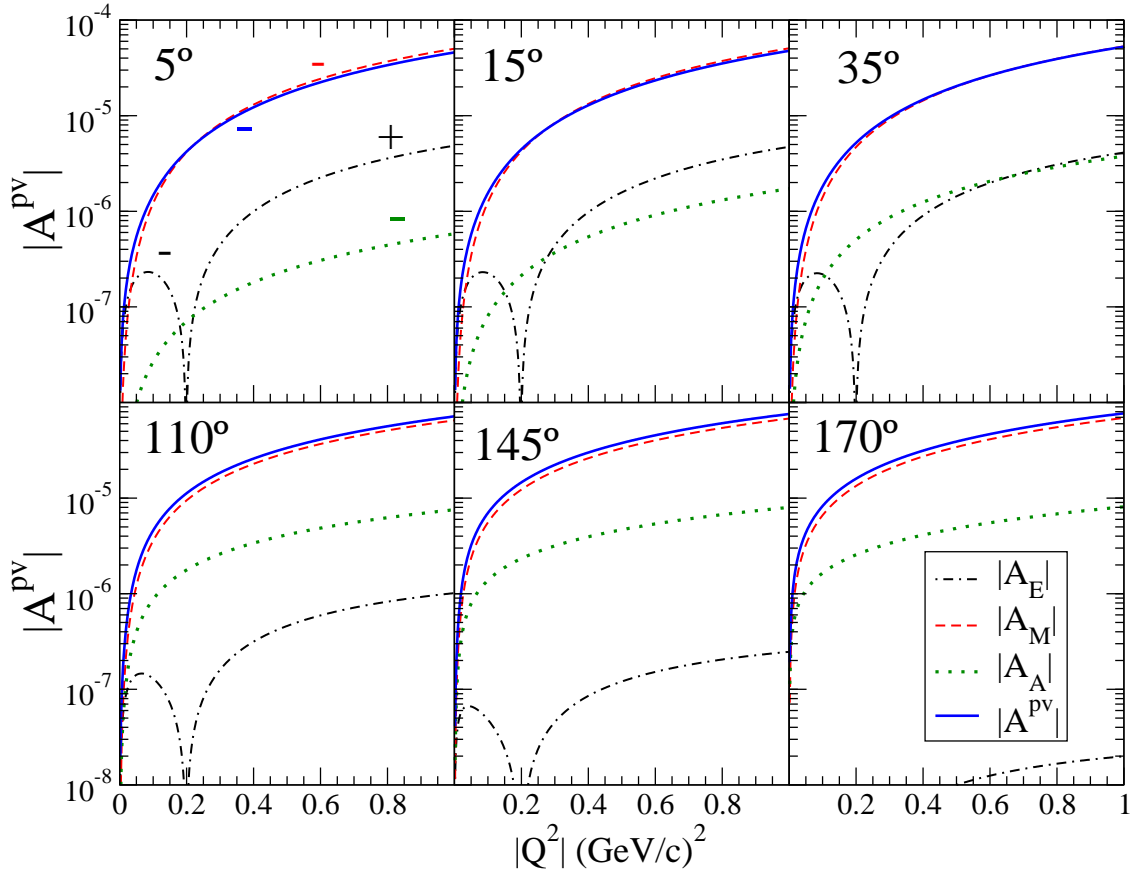


FIG. 6: (Color online) Separate contributions in the PV asymmetry coming from the electric (black dashed-dotted line), magnetic (red dashed line) and axial-vector (green dotted line) distributions (see Eq. (34)). The full asymmetry (blue solid line) is also shown for reference. Results correspond to the GKex prescription. As in the previous figure, radiative corrections are included, but strangeness in the nucleon is neglected.

In order to get some insight into the sensitivity of  $\mathcal{A}^{PV}$  on the EM nucleon structure for forward and backward scattering reactions, we isolate the contributions given by the electric, magnetic and axial-vector distributions. These are shown in Fig. 6 where the three terms

$\mathcal{A}_{E,M,A}$  (see Eq. (34)) are presented as absolute values. The full asymmetry (blue solid line) is also shown for reference. The symbol  $+(-)$  indicates the positive (negative) character of the corresponding response in the  $|Q^2|$  region selected. Note the absolute dominance of the magnetic contribution  $\mathcal{A}_M$  (negative for all  $Q^2$ ) in all kinematical situations, giving rise to the full response  $\mathcal{A}^{PV}$ . Concerning the electric and axial-vector terms, typically orders of magnitude smaller than  $\mathcal{A}_M$ , the relative predominance of one over the other depends on the specific kinematics. For very forward angles  $\mathcal{A}_E$  is larger, while the reverse holds in the backward-angle case. In fact,  $\mathcal{A}_E$  and  $\mathcal{A}_A$  are similar on average for  $\theta_e = 35^\circ$ .

These results can be explained easily using the general expressions given in Eqs. (35,36,37). In the limit of very forward-angle scattering,  $\theta_e \rightarrow 0^\circ$ , we have  $\varepsilon \rightarrow 1$ . Thus, the axial-vector contribution  $\mathcal{A}_A$  approaches zero, and the ratio between the magnetic and electric distributions simplifies to

$$\frac{\mathcal{A}_M}{\mathcal{A}_E} \longrightarrow \frac{\tau G_M^N \tilde{G}_M^N}{G_E^N \tilde{G}_E^N}. \quad (70)$$

In the backward-angle limiting case, *i.e.*,  $\theta_e \rightarrow 180^\circ$ , the factor  $\varepsilon \rightarrow 0$ . Hence, the electric term  $\mathcal{A}_E$  does not enter and the two remaining contributions are connected through

$$\frac{\mathcal{A}_M}{\mathcal{A}_A} \longrightarrow \sqrt{\frac{\tau}{1 + \tau}} \frac{a_A}{a_V} \frac{\tilde{G}_M^N}{G_A^{e,N}}. \quad (71)$$

This general discussion in the limit situations,  $\theta_e \rightarrow 0^\circ, 180^\circ$ , is consistent with the results presented in Fig. 6. For backward angles (three bottom panels), the larger  $\theta_e$  is the smaller the contribution from  $\mathcal{A}_E$ , being several orders of magnitude smaller than  $\mathcal{A}_{M,A}$ . Therefore, the PV asymmetry for backward-angle kinematics is entirely determined by the magnetic and axial-vector distributions.

In the case of forward-angle scattering, the electric term dominates over the axial-vector one for very small angles ( $\theta_e = 5^\circ$ ) and the two become similar at  $\theta_e \sim 30^\circ$ . Note the specific signs of  $\mathcal{A}_{E,A}$ : whereas the axial-vector term is negative for all  $Q^2$ , the electric one changes sign, being negative (positive) for the smaller (higher) values of  $|Q^2|$ . This means that  $\mathcal{A}_E + \mathcal{A}_A$  may get canceled for some transferred momenta at specific values of  $\theta_e$ . Note, however, that the inclusion of nucleon strangeness in the analysis may introduce significant deviations from these results (see below).

Returning to the discussion in Sect. III A where differences in EM form factors are seen for different experiments, we now briefly explore the consequences of these on the PV asym-

metry. In particular, we compare results using the GKex form factors with those obtained when  $G_E^p$  and  $G_M^p$  are replaced with the results found by Bernauer *et al.* [116] (see Fig. 3). The latter extend up to  $|Q^2| \cong 0.9 \text{ (GeV/c)}^2$ . The comparisons are shown in Fig. 7 and

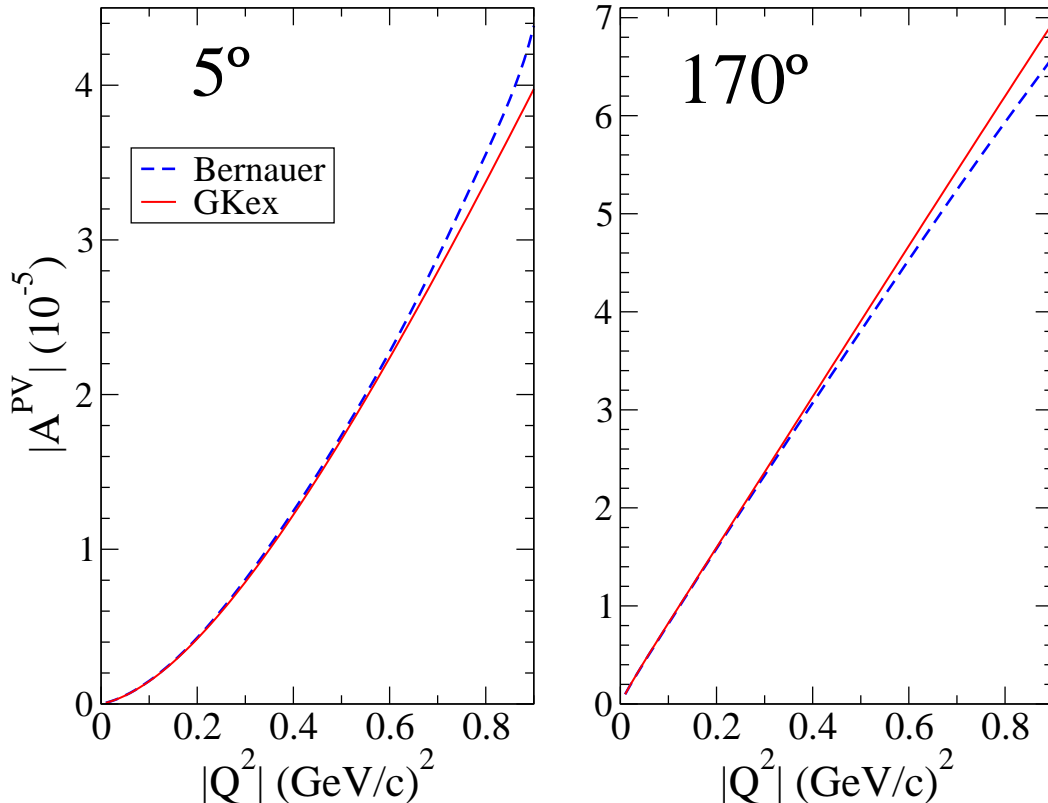


FIG. 7: (Color online) PV asymmetry computed using the fit of Bernauer *et al.* and the GKex description.

one sees that for  $\theta_e = 5^\circ$  the predicted asymmetries differ by 1.6% at  $|Q^2| = 0.2 \text{ (GeV/c)}^2$  up to 5% at  $|Q^2| = 0.8 \text{ (GeV/c)}^2$ , while for  $\theta_e = 170^\circ$  they differ by 0.7% at  $|Q^2| = 0.2 \text{ (GeV/c)}^2$  up to 4.3% at  $|Q^2| = 0.8 \text{ (GeV/c)}^2$ . Note that the magnitude of  $\mathcal{A}^{PV}$  is larger for the  $5^\circ$  case when using the Bernauer *et al.* form factors than when using the GKex form factors, but the opposite for the  $170^\circ$  case. The impact that these discrepancies may have on the analysis of the PV asymmetry and its connection with the strangeness content of the nucleon will be discussed in next sections.

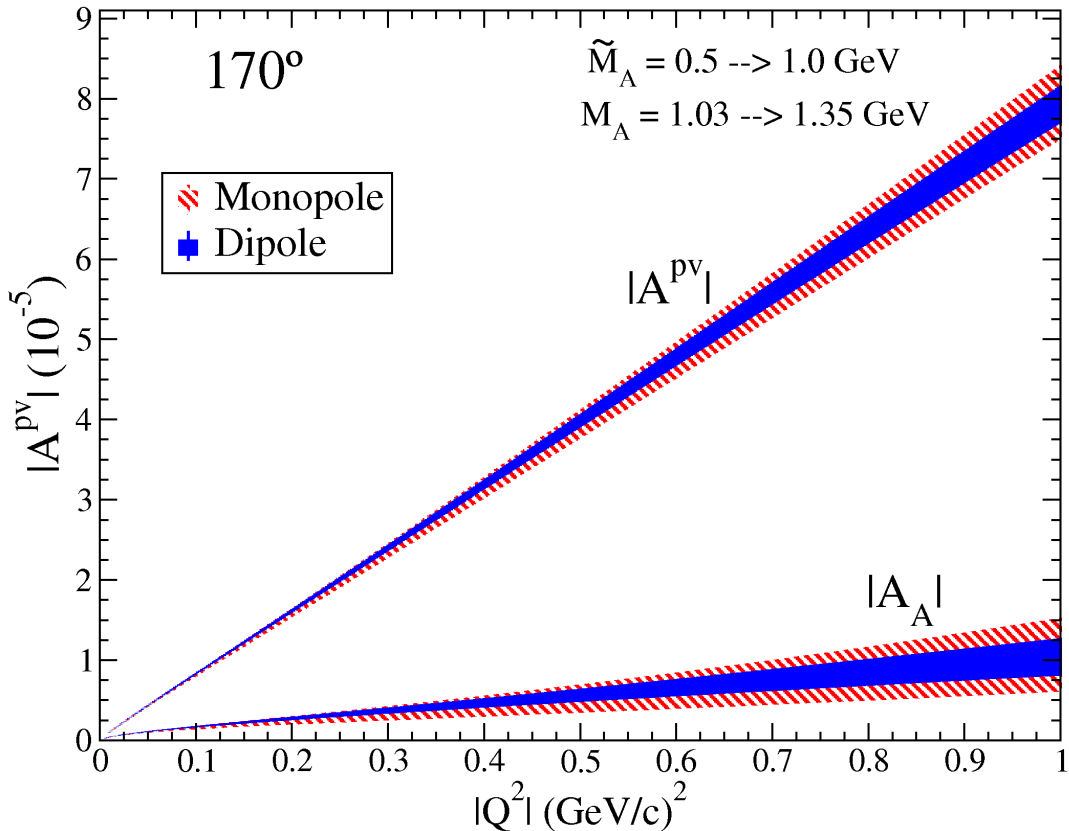


FIG. 8: (Color online) Dependence of the PV asymmetry on the description of the nucleon axial-vector form factor.

### B. Dependence on axial-vector nucleon structure

In the previous section we already introduced the basic ideas and expressions connected with the axial-vector nucleon form factor. Here we analyze how the PV asymmetry depends on the specific description of  $G_A^e$ . Results are presented in Fig. 8, where the GKex model has been used and no strangeness in the electric and magnetic sectors has been considered. In contrast, radiative corrections are included and the axial-vector strangeness content has been taken to be that in Table II. Note that  $\mathcal{A}^{PV}$  is very insensitive to  $G_A^{(s)}$ . Our interest in this section is focused on the role played by the specific functional dependence of  $G_A$  on the transferred momentum  $Q^2$  and its effect on the asymmetry. Within this context, we have evaluated the results corresponding to the standard dipole form,  $G_D^A(Q^2) = (1 + |Q^2|/M_A^2)^{-2}$ , as well as to the monopole one,  $G_M^A(Q^2) = (1 + |Q^2|/\tilde{M}_A^2)^{-1}$ .

Assuming either the dipole and monopole functional dependence, in Fig. 8 we present

results from an exploration of the effects introduced by using different values for the axial-vector masses,  $M_A$  (dipole) and  $\widetilde{M}_A$  (monopole). The average value for  $M_A$  taken from charged-current neutrino-nucleus scattering reactions is  $M_A = 1.032 \pm 0.036$  GeV (see [123]). However, recent measurements of quasielastic neutrino  $^{-12}\text{C}$  cross sections obtained by MiniBooNE collaboration [147] have shown an important discrepancy with several model predictions unless a considerably larger value of the axial-vector mass  $M_A$  is used. Although no definitive conclusions are yet in hand, and the MiniBooNE analysis may be taken more as an indication of incompleteness of the theoretical descriptions of the data, rather than as a strict indication for a larger axial-vector mass, a detailed study of modeling versus experiment for elastic PV electron-proton scattering may be able to shed light on the reliability of the different values of the axial-vector mass assuming not only the dipole shape but also the monopole one.

In Fig. 8 we show the absolute value of the PV asymmetry and the separate axial-vector contribution  $|\mathcal{A}_A|$ . The scattering angle is  $\theta_e = 170^\circ$ , that is, backward-angle scattering where the contribution of the axial-vector term is maximized. We represent as shadowed areas the range of values obtained for the asymmetry when different axial-vector masses are considered for both functional dependencies, dipole (blue area) and monopole (red). In the case of the standard dipole shape given through  $G_D^A(Q^2)$ , the values of the axial-vector mass selected are  $M_A = 1.032$  GeV (standard value) that corresponds to the lower limit and  $M_A = 1.35$  GeV (upper limit in the region) which is representative of what would bring modeling of  $\nu^{-12}\text{C}$  cross sections into agreement with data. Likewise, assuming a monopole dependence  $G_M^A(Q^2)$  (red region), the value  $\widetilde{M}_A = 0.5$  GeV corresponds to the lower limit and  $\widetilde{M}_A = 1.0$  GeV to the upper one. The strategy here is to explore the differences that might occur when a monopole form is employed rather than the conventional dipole form, making sure that a similar range of values is being considered. Choosing this (relatively generous) range for  $\widetilde{M}_A$  assures that the central values being parametrized are similar for the two choices of parametrization, as seen in the figure, and that one could obtain agreement with the neutrino experiments (given that the nuclear physics issues there are being dealt with appropriately) with either choice. Note that (by choice) the shadowed regions overlap. In fact, a larger axial-vector mass  $M_A$  in the dipole form leads to an asymmetry in accord with results corresponding to a smaller monopole axial-vector mass  $\widetilde{M}_A$ . Ultimately, results for the PV asymmetry and the different descriptions of  $G_A$ , *i.e.*, dipole versus monopole and

values of the axial-vector mass should be consistent with the analysis of neutrino scattering reactions, given that nuclear physics issues in the latter can be resolved.

To conclude this analysis, the significant effects introduced in the axial-vector contribution  $\mathcal{A}_A$  by the particular description of the axial-vector form factor lead to variations in the PV asymmetry of the order of  $\sim 5\text{--}6\%$  for dipole and  $\sim 10\text{--}11\%$  for monopole descriptions at  $|Q^2| = 1 \text{ (GeV/c)}^2$ . In both cases they are significantly larger than the ones attached to the particular description of the EM nucleon form factors, namely, about  $\sim 0.7\%$  for  $\theta_e = 170^\circ$ . However, these variations are similar to what is found when we compare the fit of Bernauer *et al.* [116] (see previous section) with the GKex or any other description, namely,  $\sim 4.3\%$  for  $\theta_e = 170^\circ$  at  $|Q^2| = 0.8 \text{ (GeV/c)}^2$ . This means that for any smaller value of the scattering angle the uncertainty associated with using the Bernauer *et al.* fit versus any other EM description is larger than the uncertainty linked to the particular  $G_A^e$  description. Again, recall that the relative contribution of the axial-vector term diminishes with decreasing values of the scattering angle.

### C. Dependence on nucleon strangeness

In this section we study the dependence of  $\mathcal{A}^{PV}$  on the strangeness content in the proton. We restrict our attention to the electric and magnetic sectors, as the axial-vector strangeness does not significantly modify the asymmetry. The functional dependence of  $G_{E,M}^{(s)}$  on  $Q^2$  is taken as the standard dipole shape in Eqs. (68,69), as well as through a monopole function that is determined by a monopole vector mass (see Sect. III C for details). The static values and the parameters that characterize the electric and magnetic strange form factors, namely,  $\mu_s$  and  $\rho_s$ , can be determined in principle from the analysis of data and their comparison with theory. Hence, in what follows we present a systematic study of the PV asymmetry with regards to the nucleon strangeness content in the electric and magnetic channels. Our theoretical predictions are compared with data taken at very different kinematics.

In order to illustrate which are the most favorable kinematical situations with regard to effects introduced by  $\bar{s}s$  in the electric and magnetic distributions, we rewrite the PV asymmetry isolating the strangeness contributions in  $\tilde{G}_{E,M}$ . Introducing the explicit expressions for the coupling constants (at tree level) and the electroweak form factors in Eqs. (57,58),

we can write:

$$\begin{aligned} \frac{2\mathcal{A}^{PV}}{\mathcal{A}_0} &= -(1 - 4 \sin^2 \theta_W) \\ &+ \frac{\varepsilon G_E^p \left( G_E^n + G_E^{(s)} \right) + \tau G_M^p \left( G_M^n + G_M^{(s)} \right) + \sqrt{\tau(1+\tau)(1-\varepsilon^2)}(1 - 4 \sin^2 \theta_W) G_M^p G_A^{e,p}}{\varepsilon (G_E^p)^2 + \tau (G_M^p)^2}. \end{aligned} \quad (72)$$

In the backward-angle scattering limit,  $\theta_e \rightarrow 180^\circ \implies \varepsilon \rightarrow 0$ , and hence the term  $G_E^{(s)}$  does not enter. In this situation the following asymmetry results:

$$\left[ \frac{2\mathcal{A}^{PV}}{\mathcal{A}_0} \right]_{\theta_e=180} = -(1 - 4 \sin^2 \theta_W) \left[ 1 - \sqrt{1 + \frac{1}{\tau} \frac{G_A^{e,p}}{G_M^p}} \right] + \frac{G_M^n + G_M^{(s)}}{G_M^p}, \quad (73)$$

where the entire dependence on strangeness is given through the magnetic term  $G_M^{(s)}$  (as already discussed, strangeness in the axial-vector form factor does not significantly modify  $\mathcal{A}^{PV}$ , and hence its contribution does not alter the general discussion that follows). From the above expressions it is clear that the basic objective in  $\mathcal{A}^{PV}$  measurements at backward-angle scattering is the determination of the strange magnetic form factor. This corresponds to the SAMPLE experiment performed at MIT-Bates [22]. However, note that a precise determination of  $G_M^{(s)}$  requires good knowledge of the axial-vector form factor. In some previous work [11, 37, 132, 133, 148] the correlation between the isovector axial-vector form factor  $G_A^{(1)}$  and the strange magnetic one  $G_M^{(s)}$  has been explored.

In the limiting forward-angle scattering kinematics  $\theta_e \rightarrow 0^\circ$ , we simply have  $\varepsilon \rightarrow 1$ ; thus, the axial-vector contribution is zero and the PV asymmetry (at tree level) reduces to

$$\left[ \frac{2\mathcal{A}^{PV}}{\mathcal{A}_0} \right]_{\theta_e=0} = -(1 - 4 \sin^2 \theta_W) + \frac{G_E^p \left( G_E^n + G_E^{(s)} \right) + \tau G_M^p \left( G_M^n + G_M^{(s)} \right)}{(G_E^p)^2 + \tau (G_M^p)^2}, \quad (74)$$

which depends not only on the magnetic strange content, but also on electric strangeness.

In addition to the TPE contributions linked to the  $\gamma\gamma$ -box (commented on at the beginning of Section IV) that are believed to be responsible for the discrepancy between the Rosenbluth and polarization transfer data [105, 140], one should also consider the role played by the  $\gamma Z$ -box. A detailed study on this topic, including also the  $WW$  and  $ZZ$ -box diagrams, has recently been presented in [149–151]. In those works the  $\gamma Z$ -box contribution is examined making use of dispersion relations and it is found to have a significant energy dependence. Although this could have some impact on the  $Q^2$ -dependence and strangeness

extraction, some caution should be exercised when drawing conclusions that are too strong from the results obtained for the strangeness content of the nucleon, including its specific  $Q^2$ -dependence.

From the analysis of the experimental data taken at  $|Q^2| = 0.1 \text{ (GeV/c)}^2$  for different targets,  $\text{H}_2$ ,  $\text{D}_2$ ,  $^4\text{He}$ , and considering forward and backward scattering angles, a correlation diagram in the  $G_E^{(s)} - G_M^{(s)}$  plane was obtained [12]. This compiles all data corresponding to SAMPLE, HAPPEX, G0 and PVA4 and provides ellipses showing the 68% and 95% confidence level constraints on the vector strange form factors. It is important to point out that these results only apply to  $|Q^2| = 0.1 \text{ (GeV/c)}^2$  where the effects introduced by different descriptions of the EM and axial-vector nucleon form factors are almost negligible (see previous sections). Our interest in this work is to present a global analysis of the asymmetry for all  $Q^2$ -values used in the experiments, showing its sensitivity to the vector strangeness content and the consistency between data and theoretical descriptions in the whole  $Q^2$ -range.

Within this general framework and because of the present lack of knowledge on the strange form factors  $G_{E,M}^{(s)}$  and their specific dependence with  $Q^2$ , our main task in what follows is to evaluate  $\mathcal{A}^{PV}$  for different values of the magnetic and electric strangeness parameters,  $\rho_s$  and  $\mu_s$ , assuming not only the standard dipole ( $G_D^V(Q^2)$ ), but also the monopole ( $G_M^V(Q^2)$ ) functional dependence. The values selected for the vector masses are  $M_V = 0.84 \text{ GeV}$ , the standard value for EM form factors, and  $\widetilde{M}_V = 1.02 \text{ GeV}$  which corresponds to using the mass of the  $\phi$  meson to explore what happens when a higher mass is employed. The values chosen for  $\widetilde{M}_A$  correspond to using a range that yields results similar to what occurs when using a dipole axial-vector form factor. Again, the objective of this study is to see what happens to the PV asymmetry when the functional  $Q^2$  dependence is changed (see the motivations presented in the previous section.)

In the figures that follow we show the evolution of  $\mathcal{A}^{PV}$  with  $|Q^2|$  for several scattering angles and different strengths for the strangeness content.

All data error bars presented in this work represent the total experimental error computed by adding in quadrature the statistical and systematic errors. For the particular case of the G0 experiment, the “extra” global systematic error has simply been added to the experimental one obtained by adding in quadrature the statistical and systematic errors. This follows from the general analysis presented in [31] where the error bars in the data include

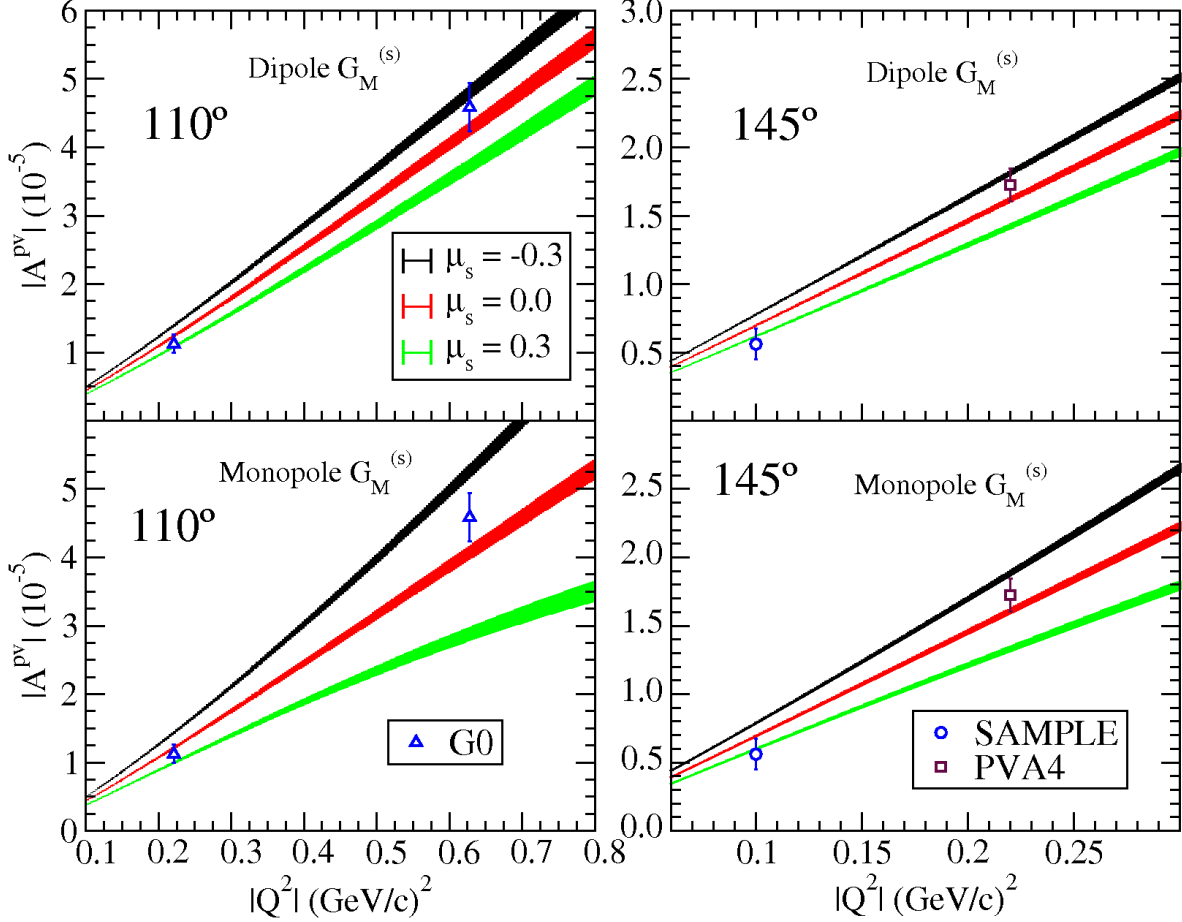


FIG. 9: (Color online) PV asymmetry for backward scattering angles:  $\theta_e = 110^\circ$  (left panels) and  $\theta_e = 145^\circ$  (right panels). Results in upper panels refer to the use of the standard dipole shape in  $G_M^{(s)}$ , whereas the monopole form has been considered in the lower panels. Three different values for the magnetic strange parameter  $\mu_s$  have been considered, namely,  $-0.3$  (upper curves),  $0$  (middle curves) and  $0.3$  (lower curves). In each case the shadowed area represents the uncertainty linked to the particular description of the WNC axial-vector form factor, specifically, the dipole functional dependence on  $Q^2$  has been chosen and the corresponding values for the axial-vector mass:  $M_A = 1.03$  and  $M_A = 1.35$  GeV. The data are taken from [22, 29, 30].

the statistical uncertainty and statistical plus point-to-point systematic uncertainties added in quadrature. The global systematic uncertainty in that work comes partially from the measurement and partially from the uncertainties in the evaluation of the “no-vector-strange” asymmetry (see [31] for details).

Results in Fig. 9 correspond to the asymmetry  $\mathcal{A}^{PV}$  evaluated at backward angles,  $\theta_e = 110^\circ$  (left panels) and  $\theta_e = 145^\circ$  (right panels). As already shown, in this kinematical

situation the contribution of  $G_E^{(s)}$  can be neglected. Hence the analysis of strangeness is focused on the purely magnetic sector. The results in the upper panels have been evaluated using the standard dipole shape for  $G_M^{(s)}$ , *i.e.*, given through  $G_D^V(Q^2) = (1 + |Q^2|/M_V^2)^{-2}$  with  $M_V = 0.84$  GeV. On the contrary, the lower panels present results obtained with the monopole function  $G_M^V(Q^2) = (1 + |Q^2|/\widetilde{M}_V^2)^{-1}$  with  $\widetilde{M}_V = 1.02$  GeV. In all cases the GKex prescription has been considered for the EM nucleon form factors and three different values for the static strange magnetic content  $\mu_s$  have been used:  $-0.3$  (black),  $0$  (red) and  $0.3$  (green). These values are consistent with some previous work [52, 137, 148].

The shadowed area for each  $\mu_s$ -value represents the region spanned by the uncertainty linked to the description of the WNC axial-vector form factor  $G_A^e$  using the dipole function as discussed in Fig. 8. The lower limit corresponds to  $M_A = 1.032$  MeV and the upper one to  $M_A = 1.35$  MeV. Note that when using the monopole shape for  $G_A^e$  the associated uncertainties increase to a few percent (see previous section).

The comparison with available data, also provided in Fig. 9, shows some difficulties in reproducing data from different experiments by using a single value for the magnetic strangeness parameter  $\mu_s$ . This comment applies to both backward angles no matter which particular functional dependence on  $Q^2$  is assumed for  $G_M^{(s)}$ . In this sense it is crucial to point out that the shadowed regions corresponding to the three  $\mu_s$ -values considered are clearly separated for all  $Q^2$  (particularly true for  $\theta_e = 145^\circ$  and  $\theta_e = 110^\circ$  with the monopole shape).

In order to clarify the above statements, let us start by discussing the kinematics where  $\theta_e = 110^\circ$  (left panels). As observed, the data taken from the G0 experiment at  $|Q^2| \sim 0.2$  and  $\sim 0.6$  (GeV/c)<sup>2</sup> are not in accord with theoretical results evaluated with the same magnetic strangeness content. Whereas the point at  $|Q^2| \sim 0.2$  (GeV/c)<sup>2</sup> is consistent with positive and close-to-zero  $\mu_s$  (green and red regions), on the contrary data at  $|Q^2| \sim 0.6$  (GeV/c)<sup>2</sup> are fitted by results obtained with negative or close-to-zero  $\mu_s$ -values. This situation is even more transparent for  $\theta_e = 145^\circ$  (right panels) where the dispersion linked to the axial-vector form factor is smaller due to the lower range in  $|Q^2|$  considered, and the regions for different  $\mu_s$  are widely separated. Note that the SAMPLE experiment ( $|Q^2| = 0.1$  (GeV/c)<sup>2</sup>) agrees on average with  $\mu_s = 0.3$ , but PVA4 ( $|Q^2| \sim 0.2$  (GeV/c)<sup>2</sup>) shows consistency with negative static strangeness. This conclusion, that applies to both functional dependencies in  $G_M^{(s)}(Q^2)$ , dipole (top panel) and monopole (bottom), should be taken with some caution due to the error bars shown by data.

In spite of the previous general discussion and the potentially different slopes shown by theory and data as functions of  $|Q^2|$ , the data error bands allow one to conclude that  $\mu_s = 0$  seems to be the case where theory and data fit the best. As discussed previously, backward-angle measurements of  $\mathcal{A}^{PV}$  should be considered as a means to isolate the contribution of  $G_M^{(s)}$ . Results in Fig. 9 show the significant sensitivity of the asymmetry to variations of the magnetic strangeness, in fact, much more important than effects introduced by other ingredients, the axial-vector and the EM form factors, including the fit of Bernauer *et al.*. However, comparison between theory and data taken at different  $Q^2$ -values (G0, SAMPLE and PVA4) presents some discrepancies that still need further investigation. From our general study using the entire set of different descriptions of the EM, axial-vector and strangeness form factors, it is not obvious that one is in a position to select a specific  $\mu_s$ -value that provides a successful description of all of the different  $Q^2$ -data measured. Results in Fig. 9 show that the slope of  $|\mathcal{A}^{PV}|$  increases with decreasing (larger) values of  $\mu_s$  ( $M_A$ ).

Our interest in the preceding discussion (with the results shown in Fig. 9) has been centered on a direct comparison between data taken at different  $|Q^2|$ -values and theoretical results evaluated assuming several prescriptions for the EM and WNC nucleon form factors. Particular emphasis has been placed on the roles played by the electric and magnetic strangeness content in the nucleon and their impact on the PV asymmetry; not only the global change in  $\mathcal{A}^{PV}$  but also the specific behavior with  $Q^2$  are investigated. This analysis allows one to get strong constraints on the potential amount of strangeness contained in the nucleon. Moreover, this study is also appropriate to dismiss specific descriptions of the nucleon form factors in conjunction with particular values of strangeness and/or  $Q^2$ -dependence. A direct comparison between theory and data is also helpful to determine clearly the dominant ingredients in  $\mathcal{A}^{PV}$  for different kinematics. This explains the analysis already presented for backward scattering (Fig. 9) and the detailed study that follows for kinematics at forward-angles (Figs. 10–12). However, in order to make the discussion clearer, it is important to connect all of these results with a global analysis of the world data. This is presented in Section IV.E, and complements the results shown in this section, in order to help the reader to obtain a general and convincing understanding of the ingredients and constraints connected with the PV asymmetry and the nucleon form factors.

The analysis of forward-angle scattering kinematics is presented in Figs. 10–12 where,

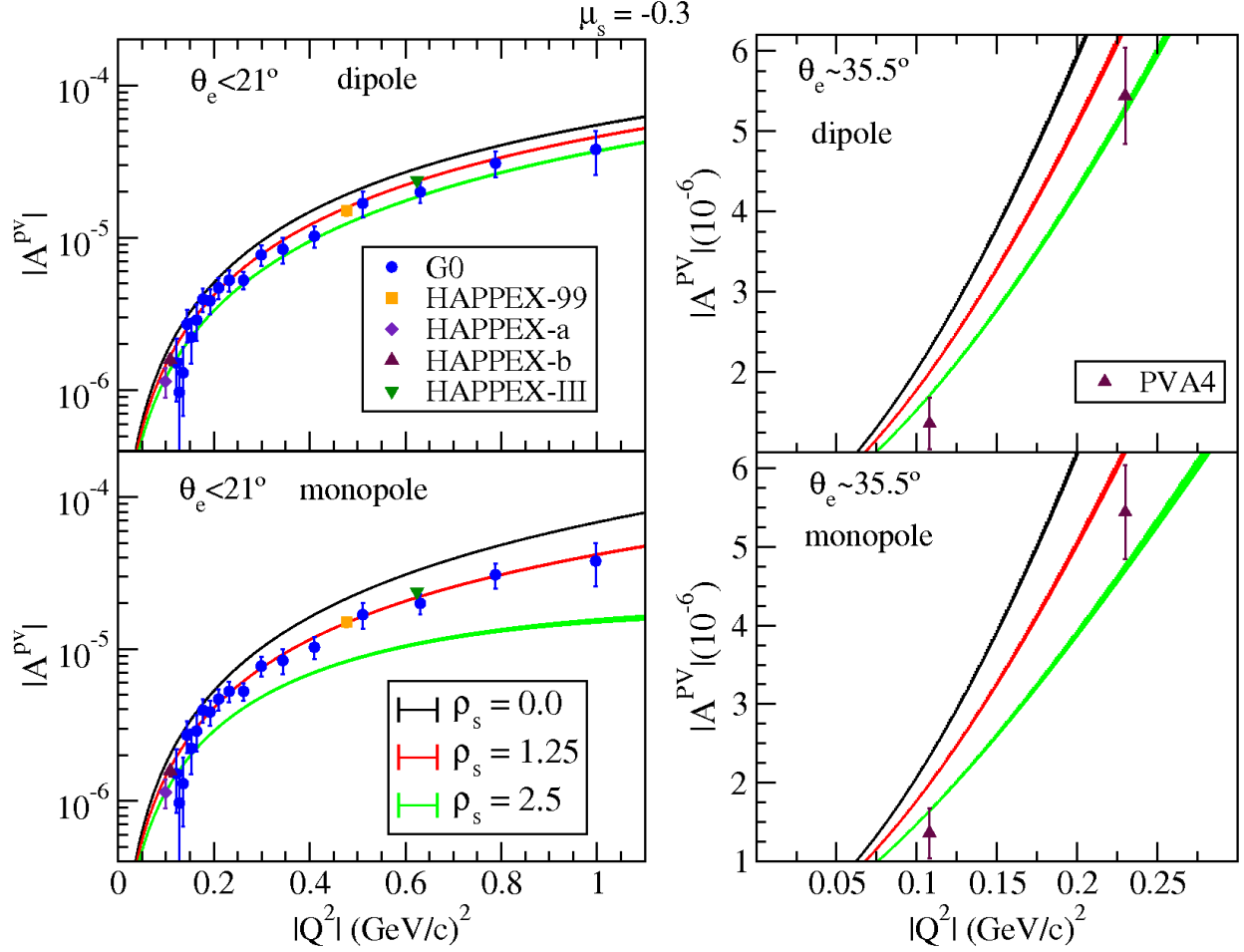


FIG. 10: (Color online) PV asymmetry evaluated at forward scattering angles compared with experimental data. The GKex prescription for the EM nucleon form factors has been used. The top panels correspond to the electric and magnetic strange form factors given through the standard dipole shape (see text for details), and the bottom panels to a monopole description. The width of the various curves incorporates the total uncertainty linked to the WNC axial-vector form factor description (see text for details). The value of the static magnetic strange parameter is fixed to  $\mu_s = -0.3$  and results are presented for three values of the electric strange content given through  $\rho_s$ : upper curves  $\leftrightarrow \rho_s = 0$ , middle curves  $\leftrightarrow \rho_s = 1.25$  and lower curves  $\leftrightarrow \rho_s = 2.5$ . The data are taken from [23–28, 31].

as in the previous case, the EM nucleon form factors provided by GKex model have been used. Each graph corresponds to results evaluated for specific magnetic strangeness content:  $\mu_s = -0.3$  (Fig. 10),  $\mu_s = 0$  (Fig. 11) and  $\mu_s = 0.3$  (Fig. 12). In all cases, theoretical results are compared with data taken at different kinematics. In order to make the discussion

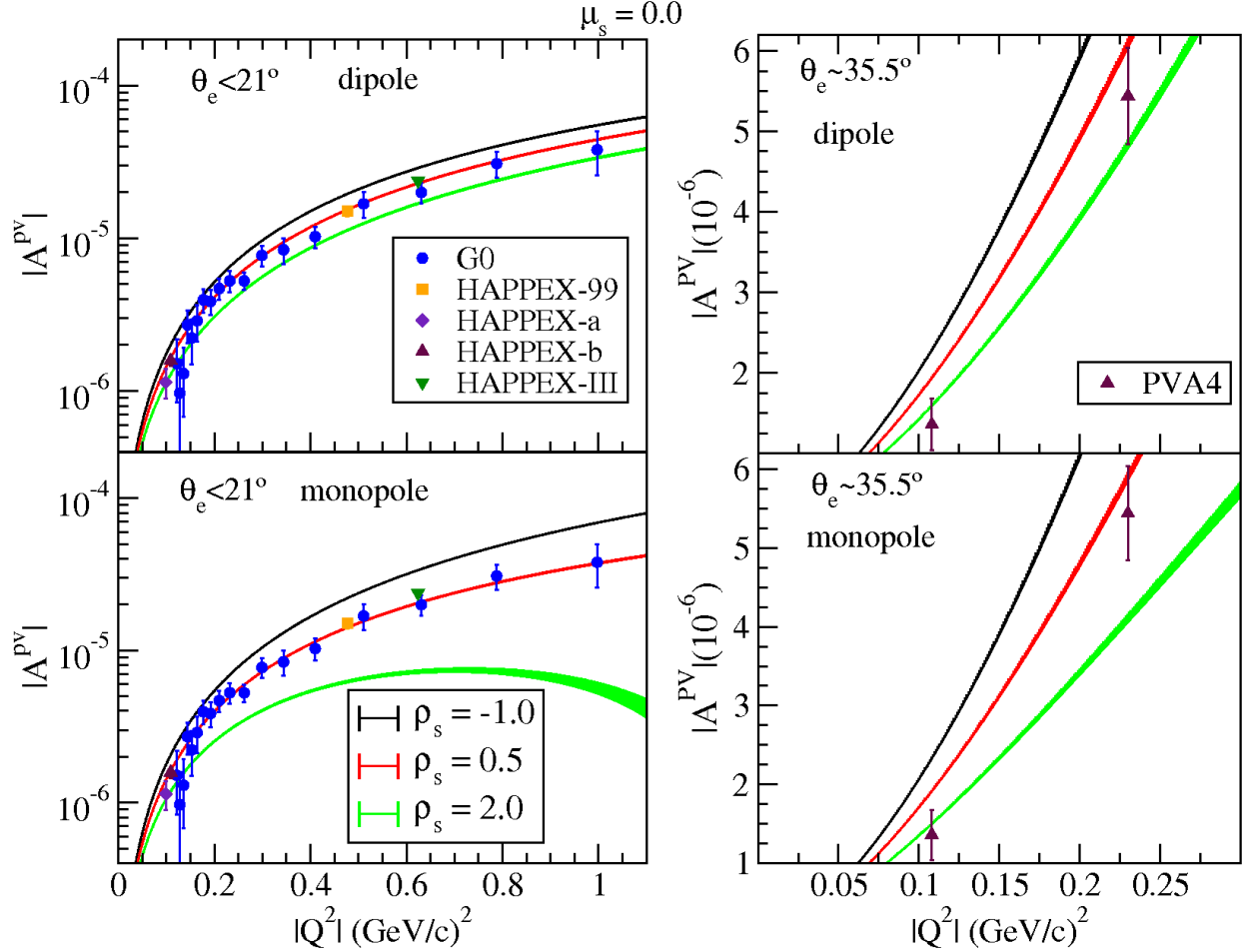


FIG. 11: (Color online) As for Fig. 10, except now for  $\mu_s = 0.0$  and with upper curves  $\leftrightarrow \rho_s = -1.0$ , middle curves  $\leftrightarrow \rho_s = 0.5$  and lower curves  $\leftrightarrow \rho_s = 2.0$ .

that follows easier, the data have been separated into two basic categories: i) forward-angle scattering, *i.e.*,  $\theta_e < 21^\circ$  (panels on the left), and ii) larger scattering angles,  $\theta_e \sim 35.5^\circ$  (right panels). In case i), the extreme values of the scattering angle for data are  $\theta_e = 6^\circ$  for HAPPEX-a and  $21^\circ$  for G0 at  $|Q^2| \cong 1$   $(\text{GeV}/c)^2$ . Hence, the theoretical PV asymmetries have been computed at  $\theta_e = 15^\circ$  since it corresponds approximately to the central value and differences between theoretical asymmetries evaluated at  $\theta_e = 15^\circ$  and  $6^\circ$  and between  $15^\circ$  and  $21^\circ$  are small (less than 3%). The difference between top and bottom panels is linked to the functional dependence assumed for the strangeness electric and magnetic form factors on  $|Q^2|$ , namely, dipole shape (top panels) and monopole one (bottom). In each case three values for the static electric strangeness content  $\rho_s$  have been considered. These are indicated by the three color curves, green, red and black. The widths of the curves take

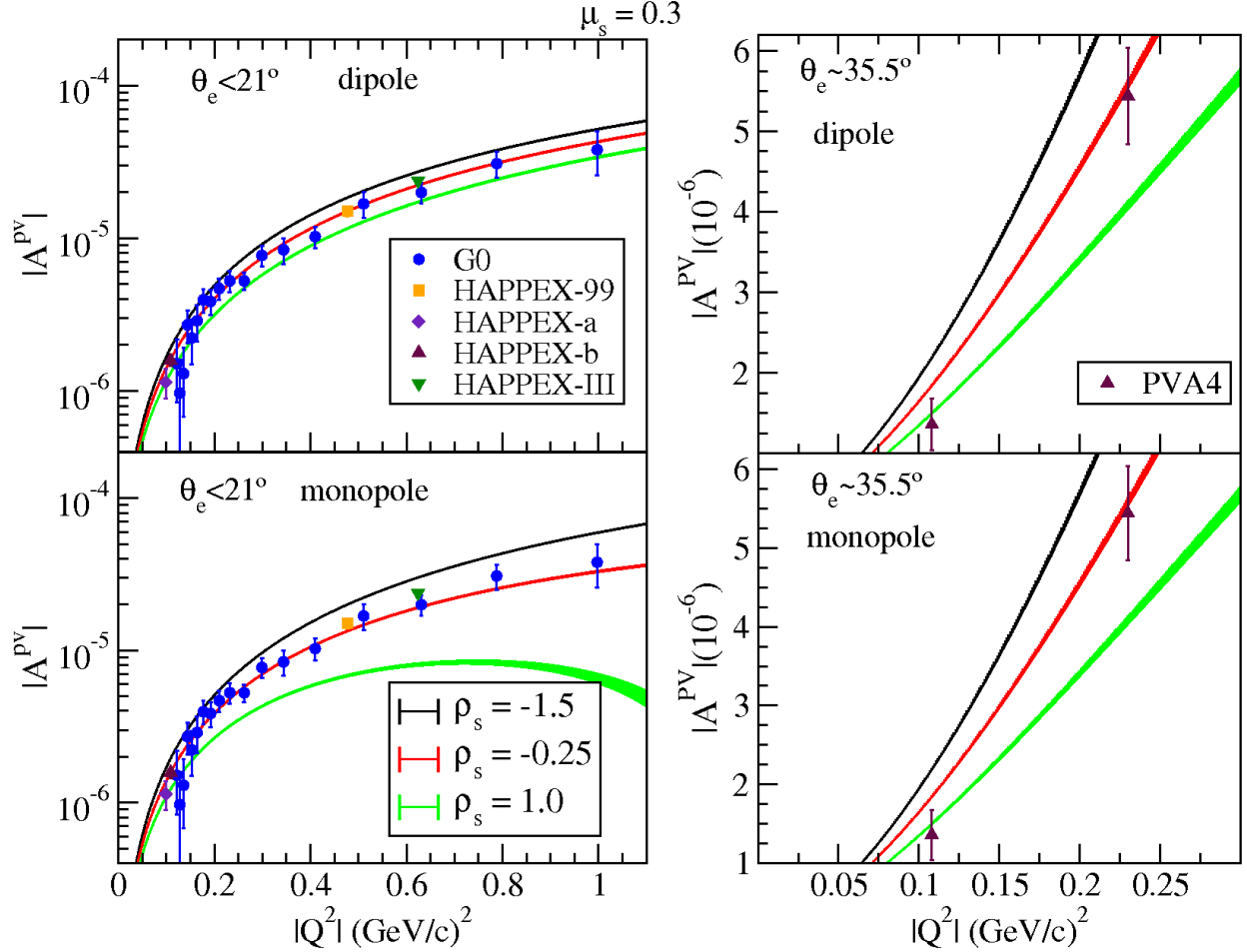


FIG. 12: (Color online) As for Fig. 10, except now for  $\mu_s = 0.3$  and with upper curves  $\leftrightarrow \rho_s = -1.5$ , middle curves  $\leftrightarrow \rho_s = -0.25$  and lower curves  $\leftrightarrow \rho_s = 1.0$ .

into account the uncertainty introduced by the description of the axial-vector form factor as discussed in the previous section. As expected, the width increases for larger scattering angles; compare for instance Fig. 9 with the right-hand panels in Figs. 10-12. Notice that the relative contribution of the WNC axial-vector form factor tends to vanish as  $\theta_e$  approaches zero (see Fig. 6).

As observed, the specific values selected for  $\rho_s$  are different in each figure in order to provide a region containing all data taken at different  $|Q^2|$ -values. The dependence of the PV asymmetry on the electric strangeness content  $\rho_s$  is clearly observable in all cases, particularly if the monopole shape is assumed. Let us note how the different curves depart for increasing  $|Q^2|$ -values (bottom panels). This clear separation may help in disentangling which specific choice of electric strangeness is best suited to the behavior of the data. This

analysis should be coherent with the study applied to backward-angle kinematics where the focus is on the magnetic strangeness content. However, as already discussed in that situation, the analysis of data at forward-angle scattering and its comparison with theory also introduces some ambiguities that need to be clarified.

Let us start with the case of smaller angles, *i.e.*,  $\theta_e < 21^\circ$ , and assuming the standard dipole form for the strange nucleon form factors (left-top panels in Figs. 10-12). As observed, the results for the three  $\mu_s$ -values are very similar and most of the data are located inside the region defined by the two  $\rho_s$  limit values considered in each graph. In particular, the results corresponding to the intermediate values:  $\rho_s = 1.25$  (Fig. 10),  $\rho_s = 0.5$  (Fig. 11) and  $\rho_s = -0.25$  (Fig. 12) fit nicely the behavior of the data with  $|Q^2|$ . This outcome also applies to results provided with the monopole functional dependence (left-bottom panels). However, in this case the differences introduced by the limit  $\rho_s$ -values are much larger, clearly over- or under-estimating the data for all transferred momenta. This means that any variation in the static parameters  $\rho_s$  and/or  $\mu_s$  may have a much stronger impact on the PV asymmetry when a monopole shape for the vector strangeness is assumed. This outcome is clearly shown in Section IV.E where a global analysis of world data is presented.

Results for larger scattering angles ( $\theta_e \sim 35.5^\circ$ ) are presented in the right-hand panels. Assuming the standard dipole parameterization for the strange form factors (upper panels), we observe that the accordance between data and theory gets better for the area between the green and red curves, that is, using the larger values of  $\rho_s$ . On the contrary, the remaining value (black curve) overestimates the data. This result holds for the three magnetic strangeness cases considered and it introduces some ambiguity in connection with the previous case, *i.e.*, scattering angle values  $\theta_e < 21^\circ$ . As shown, given a specific  $\mu_s$  and assuming the standard dipole shape for the functional  $|Q^2|$  dependence, the electric strangeness that provides the best accord with data at  $\theta_e < 21^\circ$  on the contrary overestimates the behavior of data at larger  $\theta_e \sim 35.5^\circ$ .

The use of a monopole shape in the form factors (right-bottom panels) does not introduce significant differences with respect to the previous case. This is consistent with the low- $Q^2$  region ( $|Q^2| \leq 0.3 \text{ (GeV/c)}^2$ ) explored in this situation.

It is important to point out that theoretical results obtained for  $\mu_s = -0.3$  and  $0.3$  are not in accord with all data measured at different  $|Q^2|$  for backward-angle kinematics (see Fig. 9). On the contrary, results evaluated for  $\mu_s = 0$  (no magnetic strangeness) agree with

data within the experimental error bands, although being at the extreme. As already stated, these general conclusions are consistent with the global analysis presented in Section IV.E where the PV asymmetry is analyzed taking the characterization of the electric and magnetic strangeness content of the nucleon as free parameters and leading to a better appreciation of the range of values permitted by analyses of the world data.

#### D. Radiative Corrections

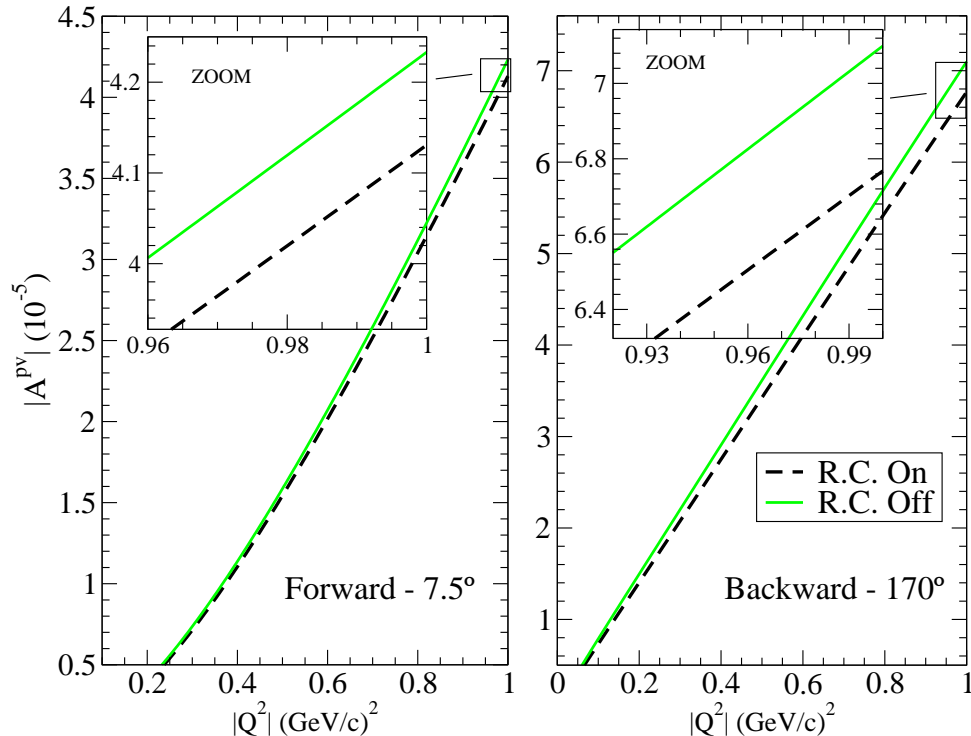


FIG. 13: (Color online) PV asymmetry evaluated at forward,  $\theta_e = 7.5^\circ$  (left panel) and backward,  $\theta_e = 170^\circ$  (right) kinematics. In both cases, results obtained with the electroweak form factors evaluated at tree level (see Eqs. (57, 58)) are compared with the ones incorporating radiative corrections as given in Eqs. (64, 66).

The effects introduced by radiative corrections in the PV asymmetry are illustrated in Fig. 13. Here the electric and magnetic strange form factors have been fixed to  $\rho_s = -0.25$ ,  $\mu_s = 0.3$ , and the dipole functional dependence with the axial-vector mass  $M_A = 1.032$  GeV has been chosen. Dashed lines correspond to results obtained at tree level, whereas the green solid lines incorporate the effects introduced by the radiative corrections at the level

of the electric, magnetic and axial-vector form factors. The analysis of these results shows that radiative corrections are more important at backward-angle kinematics where the difference amounts to  $\sim 5\%$  at  $|Q^2| = 1$  (GeV/c) $^2$ , falling to  $\sim 2\%$  at forward scattering angles. Concerning the separate contribution of the radiative corrections in the electric/magnetic (E/M) sector versus the axial-vector one, one notes that at forward-angle kinematics the entire dependence comes from the E/M sector. Indeed, the axial-vector contribution is negligible for  $\theta_e \rightarrow 0$ . On the contrary, for backward angles the radiative correction contribution in the axial-vector form factor amounts to  $\sim 3.5\%$  at  $|Q^2| = 1$  (GeV/c) $^2$ , hence being more important than the purely magnetic one ( $\sim 1.5\%$ ).

### E. Global analysis of $\mathcal{A}^{PV}$

As shown in previous sections, the result for the PV asymmetry may depend significantly on the various ingredients that enter in its evaluation, strangeness content in the nucleon, axial and vector masses,  $M_A$  and  $M_V$ , functional dependence of the weak form factors with  $Q^2$ , *etc.* Moreover, a global comparison of theory with available experimental data taken at different kinematics leads to some problems and inconsistencies that need further investigation. Thus, for completeness, we present in this section a combined analysis of the world data on  $\mathcal{A}^{PV}$  aiming to extract specific information on the WNC form factors.

To proceed we introduce the function

$$\chi^2 = \sum_{j=1}^{28} \left( \frac{\mathcal{A}_j^{exp} - \mathcal{A}_j^{th}}{\Delta \mathcal{A}_j^{exp}} \right)^2, \quad (75)$$

where  $\mathcal{A}_j^{exp}$  refers to the experimental PV asymmetry, with  $\Delta \mathcal{A}_j^{exp}$  being its uncertainty and  $\mathcal{A}_j^{th}$  the asymmetry given by the model. The sum runs over all available experimental data (28) taken at different kinematics [23–31]. To estimate the quality of the fit we have developed a code that minimizes the value of  $\chi^2$  as a function of the parameters taken for the model and finds the absolute minimum. Special care has been devoted to prevent the algorithm from being trapped in local minima. It is important to point out that for all but the G0 experiment  $\Delta \mathcal{A}_j^{exp}$  has been computed by adding in quadrature the statistical and systematic errors. In the case of G0 experiment, as mentioned before, the “extra” global systematic error has been added to the error already obtained by summing in quadrature the statistical and systematic ones (see, however, below).

To make contact with the discussion presented in previous sections, we have selected as parameters of the model the electric and magnetic strangeness content,  $\rho_s$  and  $\mu_s$ , respectively. The influence of the axial dipole mass  $M_A$ , and the vector dipole (monopole) mass  $M_V$  ( $\widetilde{M}_V$ ) in the system has also been studied.

In Fig. 14, we present the world data constraint on  $\mu_s$  and  $\rho_s$  parameters as result of our analysis. The ellipses are the projections of  $\chi^2$  function on the  $\mu_s - \rho_s$  plane and represent the  $1\sigma$  (inner) and  $2\sigma$  (outer) confidence level. The GKex model has been used for the EM form factors and radiative corrections have also been included. In the upper-left (lower-left) panel, a dipole (monopole) vector strange mass,  $M_V = 0.84$  GeV ( $\widetilde{M}_V = 1.02$  GeV) and standard dipole axial mass,  $M_A = 1.032$  GeV, have been assumed, namely, situation-(i) (situation-(iii)). In the upper-right (lower-right) panel, the same as in the left panels is assumed, but now using the extreme value for the dipole axial mass,  $M_A = 1.35$  GeV, namely, situation (ii) (situation (iv)). The reduced  $\chi^2$  is shown in each case. This is calculated as the ratio of  $\chi^2$  and the number of degrees of freedom for the system, that is, the number of experimental points minus the number of parameters. Again we note that for the G0 experiment we have used a conservative estimate where the global uncertainty is added to the other errors computed in quadrature. If instead one were to make more stringent assumptions, such as by entirely ignoring the global error (which may be warranted to some extent, since some theoretical uncertainties are apparently incorporated in the quantity), then the error ellipses become a bit smaller, although the central values change very little. Indeed, the new high- $Q^2$  HAPPEX point with its very tight uncertainty dominates the analysis.

Fig. 15 represents the same results as in Fig. 14, but in this case, the fit of Bernauer *et al.* [116] has been used to the description of the EM form factor of the proton. Note that here we have not included the G0 point at  $|Q^2| \sim 1$  (GeV/c)<sup>2</sup> because the fit of Bernauer *et al.* should not be used beyond  $|Q^2| \sim 0.9$  (GeV/c)<sup>2</sup>.

Comparing results in Figs. 14 and 15 we observe on general grounds a similar behavior for the confidence ellipses in the different situations. In particular, note the significant reduction in the area of the ellipses in the case of the monopole description for the vector strange form factors (situations (iii) and (iv)). This is in accord with Figs. 10–12 in which the dispersion in the asymmetry curves is larger when a monopole description is employed than when the form factor has a dipole shape. Note that in those figures  $\rho_s$  was fixed for the monopole and dipole descriptions, while for the ellipse here  $\rho_s$  is a free parameter. On the other hand,

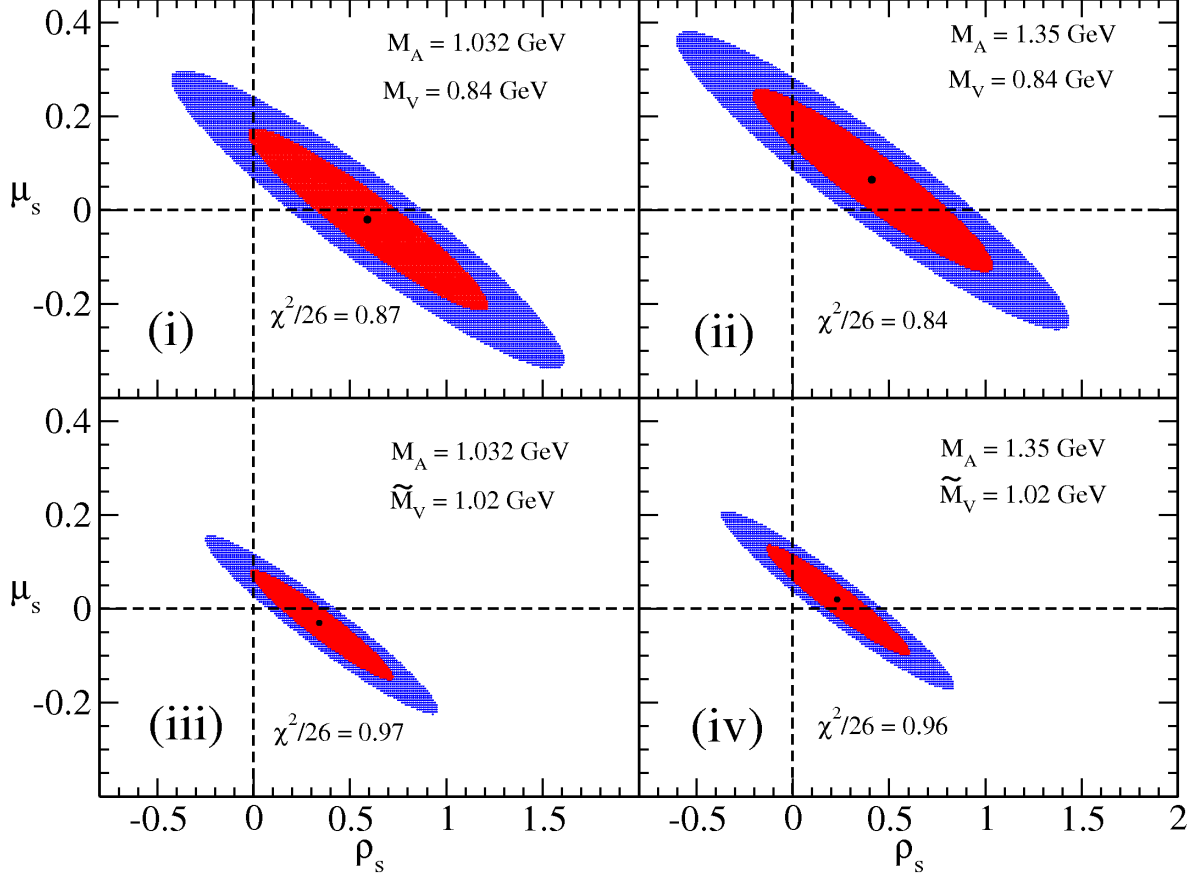


FIG. 14: (Color online) World data constraint in the  $\mu_s - \rho_s$  plane. The red (dark) and blue ellipses represent 68.27% ( $1\sigma \Rightarrow \Delta\chi^2 = 2.30$ ) and 95.45% ( $2\sigma \Rightarrow \Delta\chi^2 = 6.18$ ) confidence contours around the point of maximum likelihood (black), where  $\Delta\chi^2$  is the increase over the minimum value of  $\chi^2$ . Zero  $\mu_s$  and  $\rho_s$  (dashed black lines) are indicated for reference. The GKex model has been used for the EM form factor description. Each panel corresponds to different values of the dipole axial mass,  $M_A$ , and dipole (monopole) vector strange mass,  $M_V$  ( $\widetilde{M}_V$ ). The corresponding reduced  $\chi^2$  divided by the number of degrees of freedom for the system is also given in each panel (see text for details).

results obtained with GKex (Fig. 14) compared with the ones corresponding to the fit of Bernauer *et al.* (Fig. 15), show the confidence ellipses in the  $\mu_s - \rho_s$  plane slightly shifted towards decreasing values of  $\rho_s$  (left) and increasing  $\mu_s$  (upper). However, while most of the  $1\sigma$  ellipses are consistent with strictly positive  $\rho_s$ -values (only in situations (ii) and (iv) in Fig. 14 is the value  $\rho_s = 0$  clearly contained into the  $1\sigma$  confidence region), zero strangeness in the magnetic sector is on the contrary supported by the analysis of data in all situations.

The analysis of the  $2\sigma$  confidence ellipses also shows consistency with negative values for  $\rho_s$ .

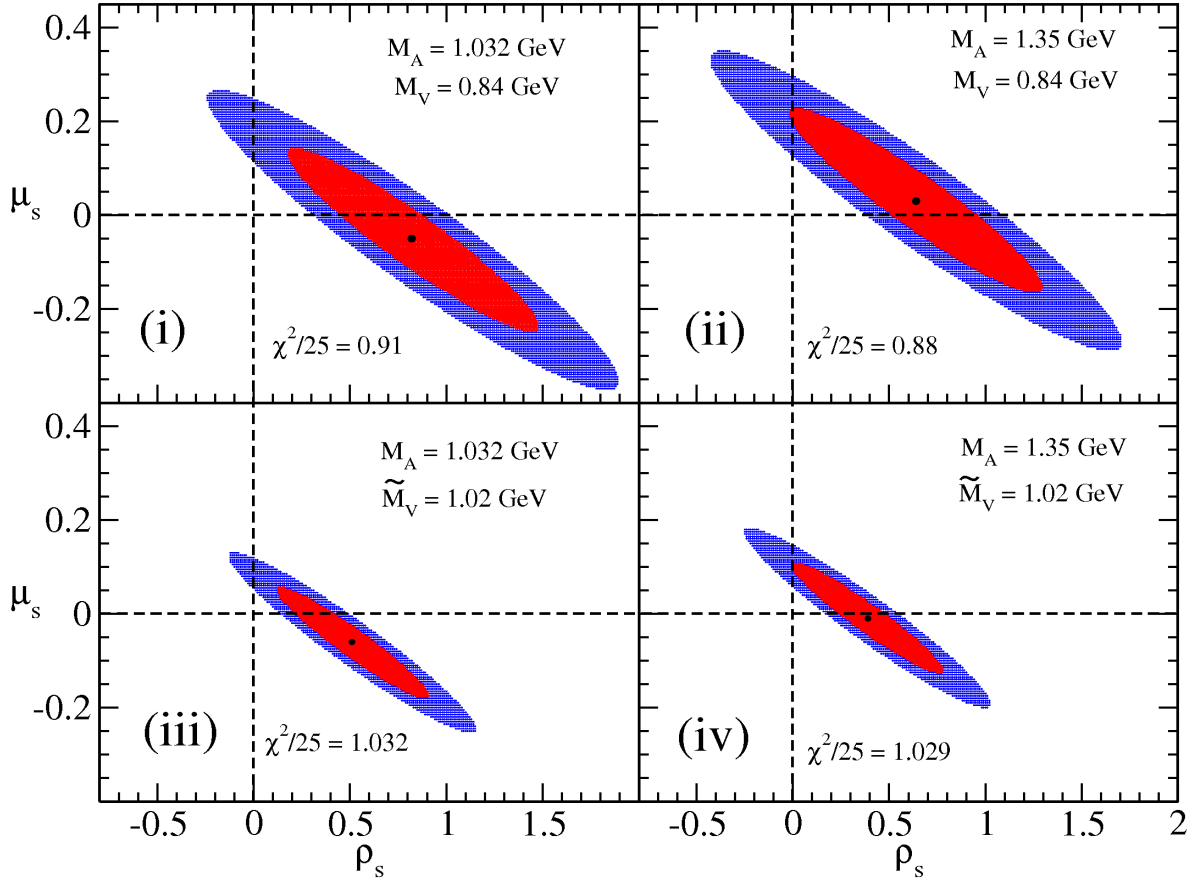


FIG. 15: (Color online) As for Fig.14, except now the Bernauer *et al.* fit has been used for EM form factors of the proton.

The effect on the PV asymmetry due to radiative corrections was studied in section IV D. For completeness, in Fig. 16 we represent the results when tree level is assumed. The standard dipole masses for both panels have been assumed,  $M_V = 0.84$  GeV and  $M_A = 1.032$  GeV. Comparing these results with the ones corresponding to situation (i) in Figs. 14 and 15, one observes that the confidence ellipses are significantly shifted to larger (smaller) values of  $\mu_s$  ( $\rho_s$ ). Although zero electric/magnetic strangeness is within the  $1\sigma$  confidence region (Fig. 16) for the two EM form factor descriptions considered, notice that the central points in the ellipses correspond to positive values of  $\rho_s$  and  $\mu_s$ .

In Table III we present a summary of all of the results shown in this section. The values presented for the parameters  $\mu_s$  and  $\rho_s$  correspond to the point of maximum likelihood (central values of the parameters). Their errors have been computed fixing one parameter

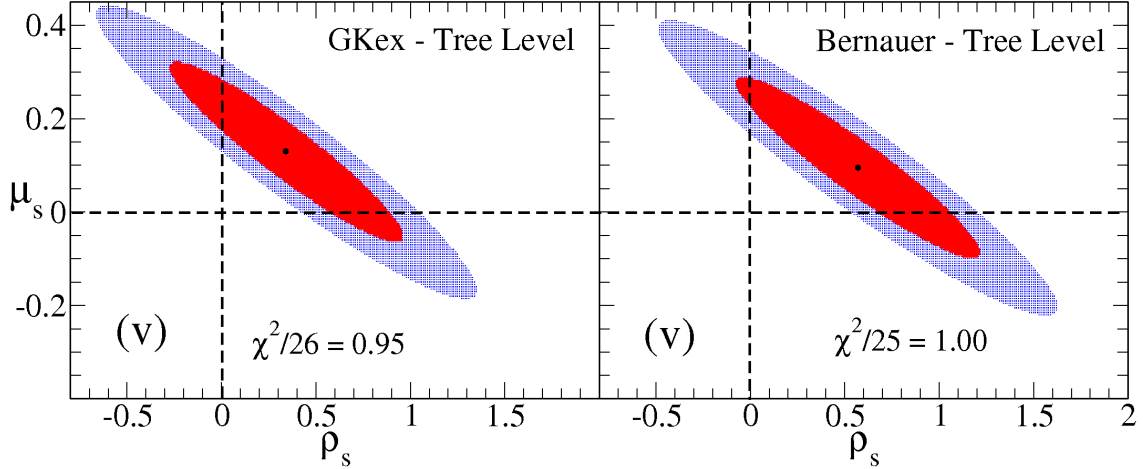


FIG. 16: (Color online) Same general comments as for Fig.14. In this case both panels correspond to a tree level calculation. A vector dipole mass,  $M_V = 0.84$  GeV, and standard axial mass,  $M_A = 1.032$  GeV, have been assumed. In the left-hand panel the GKex model has been assumed, while the fit of Bernauer *et al.* has been assumed for the right-hand one.

	GKex			Bernauer		
	$\rho_s$	$\mu_s$	$\chi^2/26$	$\rho_s$	$\mu_s$	$\chi^2/25$
(i)	$0.59 \pm 0.21$	$-0.020 \pm 0.065$	0.87	$0.82 \pm 0.22$	$-0.050 \pm 0.065$	0.91
(ii)	$0.41 \pm 0.21$	$0.065 \pm 0.065$	0.84	$0.64 \pm 0.22$	$0.030 \pm 0.065$	0.88
(iii)	$0.34 \pm 0.11$	$-0.030 \pm 0.035$	0.97	$0.51 \pm 0.11$	$-0.060 \pm 0.035$	1.032
(iv)	$0.23 \pm 0.11$	$0.020 \pm 0.035$	0.96	$0.39 \pm 0.11$	$-0.010 \pm 0.035$	1.029
(v)	$0.34 \pm 0.21$	$0.130 \pm 0.065$	0.95	$0.57 \pm 0.21$	$0.095 \pm 0.065$	1.00

TABLE III: Summary of the results shown in Fig 14 and Fig 15. Situation (v) corresponds to Fig. 16.

at its central value and moving the other parameter along the line out to the limit of the  $1\sigma$  contour.

From this analysis we conclude that the specific values of the electric and magnetic strangeness parameters show some dependence on the particular description of the EM form factors, namely, GKex versus the fit of Bernauer *et al.* The former gives rise to smaller central values for  $\rho_s$ , although they overlap with the ones obtained with the fit of Bernauer *et al.* when error bars are included. However, in all of the situations considered the analysis

of data is consistent with positive or zero  $\rho_s$ . The particular value selected for the axial mass in addition to the monopole/dipole description of the functional dependence of  $G_{E,M}^{(s)}$  with  $Q^2$  introduces important effects; note the significant reduction in  $\rho_s$  when moving from situation (i) to (iv).

Concerning the magnetic strangeness parameter  $\mu_s$ , the use of the fit of Bernauer *et al.* leads to smaller values, although the results are very close to zero strangeness. The modifications introduced using monopole/dipole form factors and the specific axial mass are also visible, leading to changes in the sign of  $\mu_s$ . However, the specific values of  $\mu_s$  are close to zero in all cases. Notice that  $\mu_s = 0$  is contained in the  $1\sigma$  confidence region in all situations.

The results obtained at tree level (Fig. 16), also summarized in Table III as situation (v), show some significant aspects that should be mentioned. The confidence ellipses are shifted towards smaller  $\rho_s$  and larger  $\mu_s$ . However, whereas the value of  $\rho_s$  is still positive but smaller than the ones corresponding to situation (i) in the previous cases, the central value of  $\mu_s$  is clearly shifted into the positive region. Note that  $\rho_s = 0$  and/or  $\mu_s = 0$  are contained in the  $1\sigma$  confidence region, in contrast with Figs. 14 and 15 (situation (i)) where  $\rho_s = 0$  is outside the  $1\sigma$  confidence region. However, the analysis of results extended to the  $2\sigma$  region also supports zero  $\rho_s$  strangeness.

To conclude, a common feature that emerges from all of the results shown in Figs. 14–16 is that either  $\rho_s = 0$  or  $\mu_s = 0$  are contained within the 95% confidence level. Moreover, no strong statement on the specific sign of  $\rho_s$  and/or  $\mu_s$  can be established. In fact, from Figs. 14–16 we observe that the only situation that is outside the  $1\sigma$  confidence contour corresponds to both  $\rho_s$  and  $\mu_s$  taking on negative values. Moreover, the special case of no strangeness, that is,  $\rho_s = \mu_s = 0$ , is also outside the  $1\sigma$  contour in most of the cases. However, some caution should be drawn for these specific  $\rho_s, \mu_s$ -values due to the analysis of the extended  $2\sigma$  confidence region.

Although not shown here, for completeness we have also analyzed the results obtained by using the weak mixing angle as given in [120]. In this case, the confidence ellipses favor smaller values of  $\mu_s$ , while the values of  $\rho_s$  permitted by the analysis of world data do not change significantly, that is, the ellipses simply move to more negative  $\mu_s$ -values. In fact, the point of maximum likelihood in the magnetic strangeness goes from a value close to zero to  $\mu_s \sim [-0.1, -0.2]$  and the case of no strangeness,  $\rho_s = \mu_s = 0$ , is within the  $1\sigma$  confidence

contour.

## F. Q-weak Experiment

In this section we analyze in detail the potential impact the variations we are considering might have on the Q-weak experiment [32–34, 152–154]. As is well known, the main aim of Q-weak is to search for new physics at the TeV scale via the measurement of the proton’s weak charge at  $|Q^2| = 0.028 \text{ (GeV/c)}^2$ , an incident energy of 1.16 GeV and  $\theta_e \sim 8^\circ$ . Some basic objectives of the experiment are to determine the weak charge of the proton to 4%, to extract  $\sin^2 \theta_W$  to 0.3% and to set limits on PV new physics at an energy scale of  $\sim 2\text{--}3$  TeV. However, in spite of the low  $|Q^2|$  value considered, the hadronic form factors still play a role and make the extracting the asymmetry and its associated error not entirely clean. Any variations we have discussed in the preceding sections may have some impact on the results. In what follows we briefly evaluate how the interpretation of the Q-weak result might be affected when different options for the description of the nucleon form factors are considered.

The general expression for the Q-weak term can be written as

$$Q_W^p = 1 - 4 \sin^2 \theta_W = \frac{-2G^2 \mathcal{A}^{PV} / \mathcal{A}_0 + B_{pn} + B_{ps}}{G^2(1 + R_V^p) - \sqrt{\tau(1 + \tau)(1 - \epsilon^2)} G_M^p G_A^{e,p}}. \quad (76)$$

In the limit of extreme forward-angle kinematics, *i.e.*,  $\theta_e \rightarrow 0$ , the axial-vector term does not contribute and the previous expression reduces to

$$Q_W^p = \frac{-2G^2 \mathcal{A}^{PV} / \mathcal{A}_0 + B_{pn} + B_{ps}}{G^2(1 + R_V^p)}. \quad (77)$$

As before, we have introduced  $G^2 = \epsilon(G_E^p)^2 + \tau(G_M^n)^2$  and the functions

$$\begin{aligned} B_{pn} &= (\epsilon G_E^p G_E^n + \tau G_M^p G_M^n)(1 + R_V^n) \\ B_{ps} &= (\epsilon G_E^p G_E^s + \tau G_M^p G_M^s)(1 + R_V^{(0)}). \end{aligned} \quad (78)$$

It is important to point out that our interest in this section is not to determine a precise value for the weak charge of the proton. On the contrary, it is to analyze how, as for the weak mixing angle, such a quantity may change due to the uncertainties associated with the description of the nucleon’s EM and WNC form factors, with special emphasis being placed on the potential electric/magnetic strangeness content in the nucleon.

EM	A-S	Kelly	BHM-SC	BHM-pQCD	GKex	Bernauer
$Q_W^p$	0.05373	0.05337	0.05422	0.05405	0.05340	0.05257
$\sin^2 \theta_W$	0.23657	0.23666	0.23644	0.23649	0.23665	0.23686

TABLE IV: Values for  $Q_W^p$  and  $\sin^2 \theta_W$  obtained through Eq. (76) for different descriptions of the EM nucleon form factors (see text for details). Electric and magnetic strangeness content of the nucleon have been fixed to the GKex-(i) situation (Table III):  $\rho_s = 0.59$  and  $\mu_s = -0.020$ .

Thus, the general procedure we adopt in this section is as follows: the value for the PV asymmetry at  $|Q^2| = 0.028$  (GeV/c)<sup>2</sup> is taken from the global fit to all electroweak data presented in [134]. This analysis leads to  $\mathcal{A}^{PV} = -1.91 \times 10^{-7}$ . Hence, the value of  $Q_W^p$  is computed through Eq. (76) making use of different descriptions for the EM and WNC nucleon form factors. The results obtained are shown in Table IV and V. All calculations have been made considering the situation GKex-(i) defined in the previous section as reference (see Table III), *i.e.*,  $M_A = 1.032$  GeV,  $M_V = 0.84$  GeV,  $\rho_s = 0.59 \pm 0.21$  and  $\mu_s = -0.020 \pm 0.065$ .

In Table IV it is seen that the effects introduced by the EM description of the form factors are very small, less than  $\sim 3\%$  to  $Q_W^p$ , *i.e.*, less than  $\sim 0.2\%$  to  $\sin^2 \theta_W$ . Note that these differences emerge from the comparison of results evaluated with the six prescriptions for the EM form factors presented in Table IV. In fact, the maximum discrepancy corresponds to the BHM-SC prescription compared with Bernauer's fit.

Table V shows the sensitivity of  $Q_W^p$  and  $\sin^2 \theta_W$  to variations of the strangeness parameters,  $\rho_s$  and  $\mu_s$ . As stated above, the PV asymmetry is taken as  $\mathcal{A}^{PV} = -1.91 \times 10^{-7}$ , and the GKex prescription is employed for the EM form factors. The specific values of the strangeness parameters presented in Table V correspond to the maximum and minimum values permitted by the ( $1\sigma$ ) errors in GKex-(i), considered as a reference case. The last column in the table shows the percentage deviation between the two values presented for  $Q_W^p$  (likewise for  $\sin^2 \theta_W$ ).

Notice that the deviations linked to the magnetic and electric strangeness are similar or even a little bit larger than the expected uncertainty of the Q-weak experiment. Hence a word of caution should be expressed on the analysis and interpretation of results derived from the Q-weak experiment.

Before concluding, we recall once more that the aim of this study is focused on the role

E-strange ( $\mu_s = -0.020$ )	$\rho_s = 0.80$	$\rho_s = 0.38$	(%)
$Q_W^p$	0.05499	0.05182	5.8
$\sin^2 \theta_W$	0.23625	0.23704	0.33
M-strange ( $\rho_s = 0.59$ )	$\mu_s = -0.085$	$\mu_s = 0.045$	(%)
$Q_W^p$	0.05203	0.05478	5.0
$\sin^2 \theta_W$	0.23699	0.23630	0.3

TABLE V: Values for  $Q_W^p$  and  $\sin^2 \theta_W$  obtained from Eq.(76) for different descriptions of the WNC nucleon form factors (see text for details). The last column corresponds to the difference between the cases considered.

played by the description of the EM and WNC form factors, particularly concerning the strangeness content, in the determination of the weak charge and/or the weak mixing angle. Thus, we have applied our global analysis as presented in previous sections to the particular kinematics corresponding to the Q-weak experiment, assuming for the PV asymmetry its value taken from an extrapolation to the forward angle using all current data [134]. Note that this study differs from the work shown in [151] (see also [149, 150]) where the focus is placed on exploring the theoretical uncertainties associated with contributions of hadronic intermediate states. The authors of [151] reexamine the  $\gamma Z$ -box contribution in the framework of dispersion relations and provide an estimate of the absolute size and uncertainty of the  $\gamma Z$  correction to the PV asymmetry in the forward-angle limit. This analysis is applied to the Q-weak experiment, providing a correction to  $\mathcal{A}^{PV}$  equivalent to a shift in the proton weak charge.

From all of this discussion it is clear that the precision measurement of the asymmetry at Jefferson Lab (Q-weak experiment) may help us in resolving some of the basic uncertainties that are still present in the study of PV elastic electron-proton scattering, and should help to deepen our understanding of the internal structure of the nucleon. Following these general ideas, and still waiting for the final analysis of the Q-weak experiment, in next section we extend our global study by incorporating the “*hypothetical*” Q-weak asymmetry value and examine its effect on the nucleon structure.

### G. Additional analysis: Neutral weak effective couplings

In this section we extend our previous analysis of strangeness in order to improve our knowledge of the WNC effective coupling constants. Thus, we provide an estimate of the electroweak parameters ( $C_{1u}$ ,  $C_{1d}$ ) consistent with the global analysis of world data presented in Section IV.E. Following the work in [134] we evaluate the confidence level contour ellipses displayed in the  $C_{1u} + C_{1d}$  versus  $C_{1u} - C_{1d}$  plane. To clarify what is done here, we explain in some detail the general procedure we have considered.

We start with the general expression for the PV asymmetry in terms of the nucleon form factors and electroweak couplings,

$$\mathcal{A}^{PV} = \frac{\mathcal{A}_0}{2} \left[ \frac{a_A \left( \varepsilon G_E^N \tilde{G}_E^p + \tau G_M^p \tilde{G}_M^p \right) - a_V \sqrt{1 - \varepsilon^2} \sqrt{\tau(1 + \tau)} G_M^p G_A^{e,p}}{\varepsilon (G_E^p)^2 + \tau (G_M^p)^2} \right], \quad (79)$$

and set the leptonic coupling constants to their values in the Standard Model at tree level, *i.e.*,  $a_A = -1$  and  $a_V = -1 + \sin^2 \theta_W$ . Coherently with our study in previous sections and also following the general arguments introduced in [117], the weak mixing angle is fixed to  $\sin^2 \theta_W = 0.23122$ . Thus, we choose as free parameters in the analysis the values of the weak neutral couplings,  $\xi_V^p$  and  $\xi_V^n$ , that enter in the WNC form factors through

$$\tilde{G}_{E,M}^p = \xi_V^p G_{E,M}^p + \xi_V^n G_{E,M}^n + \xi_V^{(s)} G_{E,M}^{(s)}. \quad (80)$$

The strangeness contribution is taken as  $\xi_V^{(s)} = -(1 + R_V^{(0)})$  with  $R_V^{(0)} = -0.0123$ .

In what follows we present a global analysis of the world data on  $\mathcal{A}^{PV}$  by showing the  $1\sigma$  (inner) and  $2\sigma$  (outer) confidence level ellipses in the  $C_{1u} + C_{1d}$  versus  $C_{1u} - C_{1d}$  plane. Results have been obtained by using the GKex description for the EM form factors and fixing the electric and magnetic strange parameters to the point of maximum likelihood using GKex-(i), *i.e.*,  $\rho_s = 0.59$ ,  $\mu_s = -0.020$  (see Table III and upper-left panel in Fig. 14). Dipole vector strange and axial masses have been assumed:  $M_V = 0.84$  GeV,  $M_A = 1.032$  GeV. As observed, for the specific GKex-(i) situation the  $1\sigma$  contour region spreads to the range  $(-0.52, -0.58)$  for  $C_{1u} - C_{1d}$  and  $(0.148, 0.18)$  for  $C_{1u} + C_{1d}$ . In the  $2\sigma$  case the range is extended to  $(-0.5, -0.6)$  [ $C_{1u} - C_{1d}$  axis] and  $(0.138, 0.19)$  [ $C_{1u} + C_{1d}$ ]. The value of the point of maximum likelihood, also presented as a label in Fig. 17, is  $C_{1u} + C_{1d} = 0.165$  and  $C_{1u} - C_{1d} = -0.550$ .

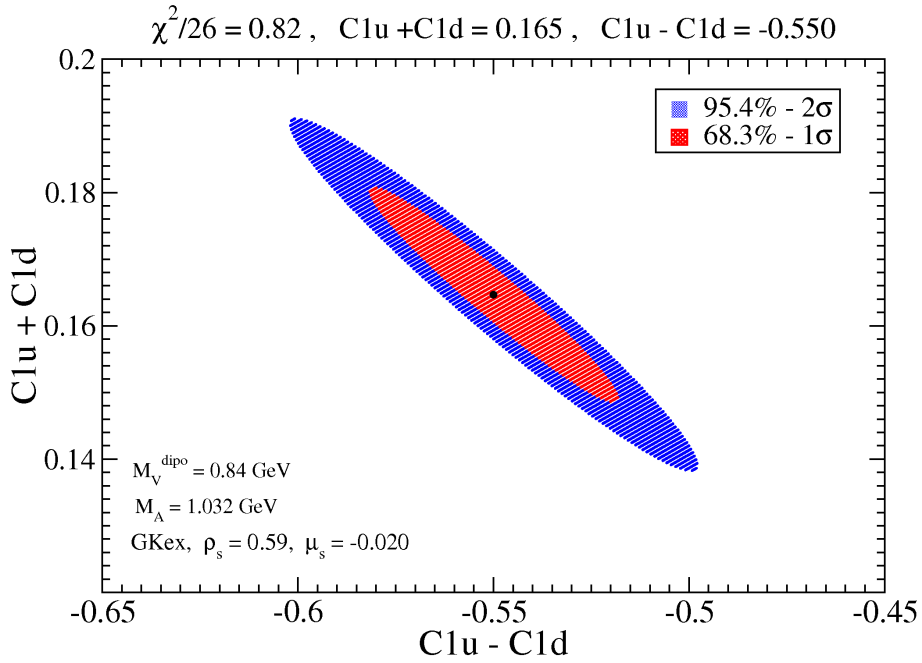


FIG. 17: (Color online) World data constraint in the  $C_{1u} + C_{1d}$  versus  $C_{1u} - C_{1d}$  plane. The red and blue ellipses represent 68.27% ( $1\sigma$ ) and 95.45% ( $2\sigma$ ) confidence contours around the point of maximum likelihood (black dot). The value of the minimum  $\chi^2$  and the point of maximum likelihood are indicated in the top legend.

As already mentioned, the use of a different value for the weak mixing angle, for instance  $\sin^2 \theta_W = 0.23867$  (see [120]), leads to differences in the confidence level ellipses. In particular, the new contour moves to the right by  $\sim 5\text{-}6\%$  (larger values of  $C_{1u} - C_{1d}$ ) and decreases ( $\sim 4\text{-}5\%$ ) along the  $C_{1u} + C_{1d}$  axis.

We complete the study by analyzing the dependence of the confidence level ellipses on the particular strangeness content in the nucleon. Thus, we redo the global analysis producing new contour ellipses that take into account the variation in strangeness, that is, the information contained in Figs. 14-16. In particular, as considered in Fig. 17, we restrict ourselves to the GKex-(i) situation and let the electric and magnetic strange parameters ( $\rho_s, \mu_s$ ) to float around the boundary contour corresponding to the  $1\sigma$  region in the upper-left panel in Fig. 14 (red region). Each point in the  $(\rho_s, \mu_s)$  contour leads to a specific confidence level ellipse in the  $C_{1u}/C_{1d}$  plane. In Fig. 18 we show the global region (green area) produced by the superposition of a full set of ellipses, each one corresponding to a specific  $(\rho_s, \mu_s)$  value.

As reference, we compare this global contour with the original one presented in Fig. 17 (red area) where the centroid:  $\rho_s = 0.59$ ,  $\mu_s = -0.02$ , was selected (see discussion above). Notice that only the  $1\sigma$  confidence level ellipses are presented in Fig. 18.

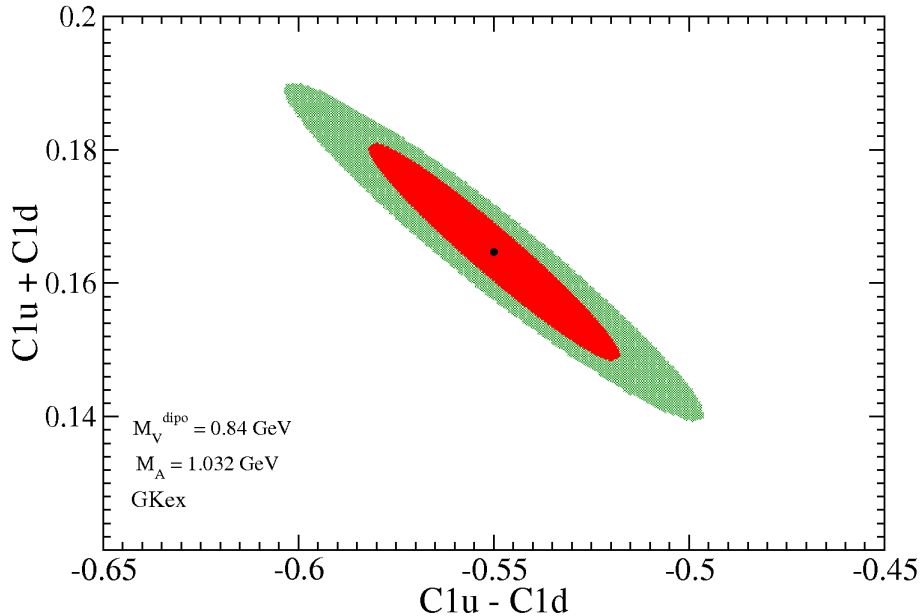


FIG. 18: (Color online) Green area represents the superposition of the full set of  $1\sigma$ -ellipses (see text for details). The red area is the original  $1\sigma$ -ellipse.

Next we investigate how the world data constraint in the  $C_{1u}/C_{1d}$  plane changes when introducing the “hypothetical” Q-weak measurement. To make the discussion that follows clear, we consider the specific situation shown in Fig. 17, and analyze how the contour changes by adding to the global fit the value  $\mathcal{A}^{PV} = -1.91 \times 10^{-7}$  with an error of  $\sim 2.2\%$  (expected Q-weak result). The new results are presented in Fig. 19 (left panel) that shows the  $1\sigma$  and  $2\sigma$  contours to be reduced very significantly; the areas in Fig. 19 are about  $\sim 85\%$  smaller than the ones shown in Fig. 17. To conclude, we apply the same analysis to results in Fig. 18, *i.e.*, letting the strange parameters float along the  $1\sigma$  level confidence contour in Fig. 14 (upper-left panel), and add again to the global fit the “hypothetical” Q-weak result. The new ellipses (linked to Fig. 18) are shown in the right panel of Fig. 19. As in the previous case, note the strong reduction in the area enclosed by the ellipses.

Finally, we note that a new experiment is planned to be run at Mainz making use of

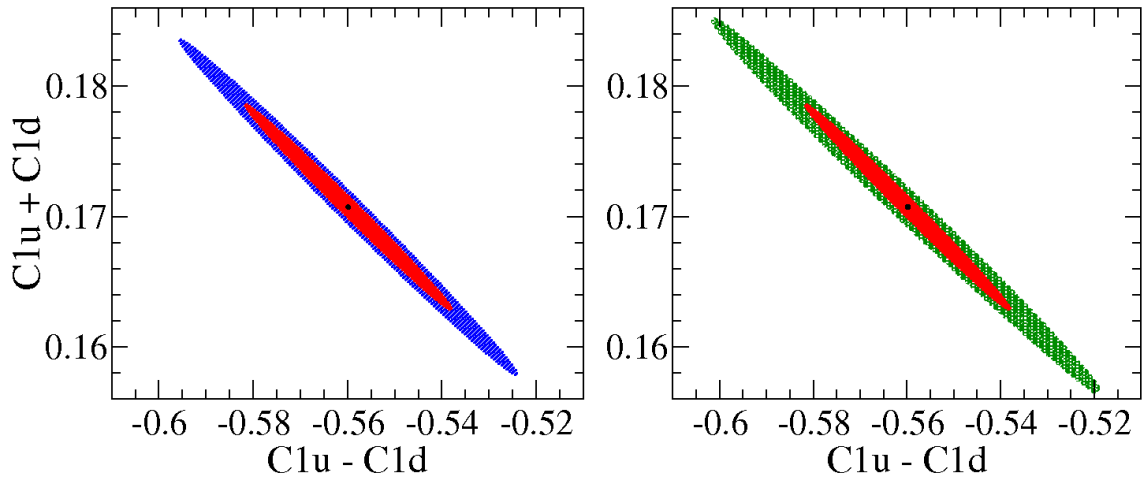


FIG. 19: (Color online) As for Fig. 17 (left panel) and Fig. 18 (right panel), except that now the hypothetical  $Q_{weak}$  result is included in the global analysis.

the MESA accelerator facility [155]. Its main aim is to provide a very precise measurement for the weak charge of the proton and weak mixing angle in the low-energy regime. The energy of the electron beam is 137 MeV and the scattering angle  $20^\circ \pm 10^\circ$ . The transferred momentum is fixed to  $|Q^2| = 0.0022 \text{ (GeV/c)}^2$ . As shown in [151], the impact of the  $\gamma Z$ -box correction is expected to be very small for these kinematics, and hence this result should complement the Q-weak experiment, at the same time providing a test for the Standard Model while also leading to a deeper understanding of the internal structure of the nucleon.

### H. Projections for Higher-Energy Experiments

To obtain some idea about the likelihood that high precision elastic e-p PV experiments may be feasible at higher energies we include here a brief section projecting what fractional precision could be attained. It should be noted that at present, even with JLab being upgraded to 11 GeV at the high currents needed for such studies, there are no approved experiments of this type; however, for completeness the following has been included. The results presented below are characterized using the standard figure of merit,

$$\mathcal{F} = (\mathcal{A}^{PV})^2 \sigma^{PC}, \quad (81)$$

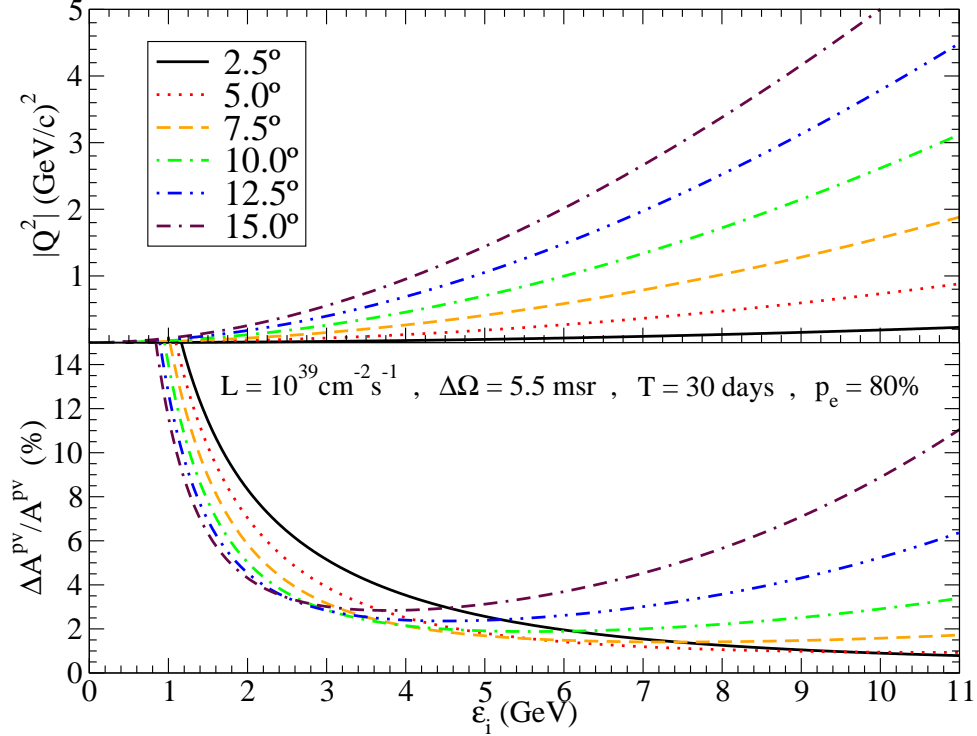


FIG. 20: (Color online). Fractional precision  $\Delta\mathcal{A}^{PV}/\mathcal{A}^{PV}$  as a function of the incident electron energy  $\varepsilon_i$  (bottom panel). The top panels show the transferred four-momentum versus  $\varepsilon_i$  for different scattering angles.

where the asymmetry  $\mathcal{A}^{PV}$  and the parity-conserving differential cross section  $\sigma^{PC}$  are evaluated within our theoretical model. This expression governs the level of statistical precision that can be achieved for given experimental conditions. The fractional precision in the asymmetry, assuming that systematic errors are under control is given by

$$\frac{\Delta\mathcal{A}^{PV}}{\mathcal{A}^{PV}} = \frac{1}{p_e \sqrt{\Delta\Omega T \mathcal{L} \mathcal{F}}}, \quad (82)$$

where  $p_e$  represents the incident electron polarization,  $\Delta\Omega$  is the detector solid angle,  $T$  is the runtime and  $\mathcal{L}$  is the luminosity. In this work we choose specific “canonical” values for all of these (see Fig. 20). For more details on these choices the reader can look at [52, 153]. The resulting fractional precision is shown in the bottom panel of Fig. 20 for a large variety of scattering angles at forward kinematics. As observed, for a wide range of kinematical conditions, *i.e.*, values of the energy  $\varepsilon_i$ , the precision expected for our “canonical” conditions lies in the vicinity of 2%, being even smaller ( $\sim 1\%$ ) for high energies and very forward scattering angles. Notice that this situation corresponds to the lowest values of the transferred momentum  $|Q^2|$  (see top panel). This is consistent with the fact that at very high  $|Q^2|$  it is

hard to avoid uncertainties coming from ingredients beyond the elastic scattering regime.

As an example of using these projections, consider the  $7.5^\circ$  case (dashed lines): at 11 GeV, the upgraded energy of the JLab facility for experiments in Halls A and C, one could reach a fractional error of better than 2% at momentum transfers reaching almost  $2 \text{ (GeV/c)}^2$ .

## V. CONCLUSIONS

This work presents a systematic study of elastic electron-nucleon scattering including parity violation (PV) in its description, *i.e.*, not only the dominant EM interaction is considered but also the role played by the weak interaction. The basic goal of the present study is to deepen our knowledge of the hadronic structure involved with a special focus on the analysis of strangeness and axial-vector content in the electroweak nucleon form factors.

Within the general framework of the Electroweak Theory of the Standard Model, we have summarized the general formalism needed in the description of the above-mentioned scattering process. Hadronic response functions and the parity-violating asymmetry or helicity asymmetry (denoted simply as PV asymmetry,  $\mathcal{A}^{PV}$ ) have been evaluated. The latter is defined as the ratio between the difference and the sum of the electron scattering cross sections for positive and negative incoming electron helicities. The helicity asymmetry being different from zero is a clear signature of the presence of the weak interaction, and thus its measurement allows one to gain insight into the electroweak structure of the nucleon. In recent years significant efforts from both the experimental and theoretical points of view have been devoted to this problem. New experiments have been devised and performed for a variety of kinematical situations. Data reported at backward and forward scattering angles are compared in this work with theoretical modeling showing the role played by the various ingredients that enter into the description of the reaction mechanism.

One of the basic ingredients in the PV asymmetry comes from the EM structure of the nucleon. Our present knowledge about the EM nucleon form factors, particularly in the case of the proton, is rather precise through measurements of elastic (parity-conserving) electron-nucleon scattering. These have involved techniques based on the Rosenbluth separation, as well as the use of nucleon polarization measurements. Although a proper description of data is provided by different models, still some ambiguities emerge from the analysis of different experiments. In particular, the behavior of the nucleon form factors with  $Q^2$  (transferred

four-momentum) may differ significantly with the particular prescription considered. In this work we have investigated a wide selection of models for the nucleon's EM structure and have analyzed the impact of these choices on the helicity asymmetry. A precise description of the EM structure of the nucleon is essential for the analysis of the PV asymmetry.

A systematic study of the PV asymmetry including its dependence on the various nucleon form factors has been presented in Sect. IV. In addition to the purely EM nucleon structure, the effects introduced by the WNC axial-vector form factor have been analyzed at depth. Functional dependencies on  $Q^2$  based on dipole and monopole shapes have been assumed using different values for the axial-vector mass in both cases. The strangeness content in the axial-vector form factor does not introduce significant effects in the PV asymmetry. From our study, when applied to backward-angle kinematics where the axial-vector contribution has its largest impact, the uncertainty in  $\mathcal{A}^{PV}$  linked to the description of the axial-vector form factor is of the order of  $\sim 5\text{--}6\%$  for dipole and  $\sim 10\text{--}11\%$  for monopole descriptions at  $|Q^2| = 1 \text{ (GeV/c)}^2$ . This uncertainty has been evaluated assuming the axial-vector mass to span the ranges  $M_A = 1.032 - 1.35 \text{ GeV}$  (dipole) and  $\widetilde{M}_A = 0.5 - 1 \text{ GeV}$  (monopole).

One of the main objectives in studies of PV electron scattering concerns the role of the strange quark in the electric and magnetic sectors  $\mathcal{A}_E$  and  $\mathcal{A}_M$  which do not involve the axial-vector form factor. Thus, the helicity asymmetry has been evaluated using different approaches to describing the strange form factors  $G_{E,M}^{(s)}(Q^2)$ . The specific strangeness content is given by the static strangeness parameters  $\rho_s$  and  $\mu_s$  in the electric and magnetic sectors, respectively, whereas the specific dependence on  $Q^2$  is taken as dipole (with the vector mass fixed to  $M_V = 0.84 \text{ GeV}$ ) and monopole ( $\widetilde{M}_V = 1.02 \text{ GeV}$ ). The analysis performed includes backward and forward scattering angles spanning the kinematics involved in the experiments.

Backward-angle measurements of  $\mathcal{A}^{PV}$  are meant to isolate the contribution of  $G_M^{(s)}$  (the electric sector is severely reduced there). From our modeling and comparisons with data some significant discrepancies emerge that need further investigation. Although being cautious because of the error bands, the behavior of data versus  $|Q^2|$  presents a positive slope which is larger than the one resulting in the theoretical calculations. This applies to both dipole and monopole functional dependencies for the strange and axial-vector form factors, and shows the difficulty in reproducing all data with a specific value for the static strange parameter  $\mu_s$ . Only  $\mu_s$ -values close to zero overall reproduce the data at different  $Q^2$  (just

touching the extreme error bands). However, data at small  $|Q^2| = 0.1$  (GeV/c)<sup>2</sup> (SAMPLE) agree better with results for positive  $\mu_s$ , whereas for  $|Q^2| = 0.6$  (G0) the best agreement emerges for slightly negative  $\mu_s$ . Finally, data measured at  $|Q^2| \sim 0.2$  (GeV/c)<sup>2</sup> for G0 ( $\theta_e = 110^\circ$ ) and SAMPLE ( $\theta_e = 145^\circ$ ) also present some difficulties when compared with theory. Whereas the former implies an intermediate value of  $\mu_s$  within the range  $[0, 0.3]$ , the latter is consistent with  $\mu_s \in [-0.3, 0]$ .

Forward scattering kinematics, where a wide selection of data taken at different  $Q^2$  are available, has been also studied in detail in Sect. IV. Comparison between theory and data shows in general good accordance concerning the behavior with  $Q^2$ . However, some significant differences which need to be clarified also emerge. In particular, assuming the dipole shape for the strange form factors with a fixed value for the magnetic strangeness parameter  $\mu_s$ , it is difficult to reproduce data taken at forward angles,  $\theta_e < 21^\circ$ , and at  $\theta_e \sim 35.5^\circ$  using a single value for the electric strangeness content  $\rho_s$ . This is, for instance, the case of  $\mu_s = 0$ , *i.e.*, no magnetic strangeness, where data at  $\theta_e < 21^\circ$  are in accord with calculations for  $\rho_s = 0.5$ , whereas data for larger scattering angles,  $\theta_e \sim 35.5^\circ$ , are located within the area between the curves corresponding to  $\rho_s = 0.5$  and larger  $\rho_s = 2$ . Similar comments apply to the other  $\mu_s$  values selected,  $\pm 0.3$ . Although the spread of results corresponding to different  $\rho_s$  is not very large, further investigation is needed in order to settle the reason for this discrepancy. When assuming a monopole shape for the strange form factors the spread between the curves calculated for different  $\rho_s$  is much higher, the different cases being clearly separated, even if uncertainties linked to the description of the axial-vector form factor are included. Discussion of the role of  $\rho_s$  and comparison with data follows similar trends to the ones already applied to the dipole description.

Summarizing, the general discussion presented in previous paragraphs clearly indicates that further studies and investigations are needed before definite conclusions on the strangeness content in the nucleon can be drawn. Not only the specific values of the strangeness content given through the parameters  $\mu_s$  and  $\rho_s$  should be reviewed, but also the specific functional dependence with  $Q^2$  has to be explored in depth. Moreover, the role played by the WNC axial-vector form factor is also crucial in understanding the results for the PV asymmetry and its comparison with data. Contrary to some previous work [12, 132, 133, 154] where the focus was placed on the analysis of specific data taken at fixed  $|Q^2|$ , here our interest has been to provide a general and coherent description of

all data measured at different transferred momenta. We also have estimated the amount of uncertainty in  $\mathcal{A}^{PV}$  linked to different descriptions of the electroweak form factors, namely to their strengths and  $Q^2$ -dependencies. Radiative corrections in the electric, magnetic and axial-vector form factors have been also analyzed and their impact on the asymmetry evaluated.

Following these general discussions a global analysis of the asymmetry  $\mathcal{A}^{PV}$  has been performed by presenting the world data constraint on the electric and magnetic strangeness parameters. Ellipses showing the  $1\sigma$  and  $2\sigma$  confidence regions in the  $\rho_s$ - $\mu_s$  plane have been presented in different situations, using GKex and the fit of Bernauer *et al.* for the EM form factors, as well as assuming monopole/dipole functional dependencies for  $G_{E,M}^{(s)}$  and different values for the axial/vector masses. From this global analysis consistency of world data with positive values of  $\rho_s$  emerges, although the specific central value of  $\rho_s$  depends on the particular situation considered. Nevertheless, the  $1\sigma$  confidence ellipses are located in most of the cases in the positive  $\rho_s$ -region (only situations (ii) and (iv) in Fig. 14 and (v) in Fig. 16 touch negative  $\rho_s$ -values at the extreme). The  $2\sigma$  confidence level extends the validity of  $\rho_s$  to slightly negative values in all cases. Concerning the magnetic sector, zero strangeness,  $\mu_s = 0$ , is located inside the  $1\sigma$  confidence region in all situations. In fact, the central values obtained using GKex (Fig. 14) and the fit of Bernauer *et al.* (Fig. 16) are very close to  $\mu_s = 0$  (within the error bands). Only when radiative corrections are neglected (Fig. 16), does the point of maximum likelihood for  $\mu_s$  clearly become positive, although zero strangeness is still contained inside the  $1\sigma$  confidence region. In general, we conclude that the magnitude of strangeness effects are constrained to be quite small. However, the analysis of the  $1\sigma$  and  $2\sigma$  confidence ellipses shows that the case of no strangeness, *i.e.*,  $\rho_s = \mu_s = 0$ , is excluded by most of the fits, as is the region where the signs are both negative.

Additionally, some considerations concerning the likelihood of future high precision PV experiments have been presented, together with discussions of the kinematical conditions under which the precision is expected to be maximum. This is likely to be the situation for the planned MESA experiment [155] where effects coming from  $\gamma Z$ -box corrections [149–151] and isospin violations [19, 20] are expected to be very small.

Finally, the potential impact the variations considered in this work might have on interpretations of the Q-weak experiment has been also discussed. From this study, we conclude

that a rough variation in the parameters of the model consistent with available data ( $1\sigma$  confidence region) may lead to the proton's weak charge determined by  $\sim 5\text{-}6\%$ , *i.e.*,  $\sin^2 \theta_W$  extracted to  $\sim 0.3\%$ . This is similar to the basic objectives pursued by the Q-weak experiment.

### Acknowledgments

This work was partially supported by DGI (Spain): FIS2011-28738-C02-01, by the Junta de Andalucía, the Spanish Consolider-Ingenio 2000 programmed CPAN (CSD2007-00042), and part (TWD) by U.S. Department of Energy under cooperative agreement DE-FC02-94ER40818. R.G.J. acknowledges support from the Ministerio de Educación. We thank K. Kumar for helpful discussions.

- 
- [1] S. Boffi, C. Giusti and F. D. Pacati, Phys. Rep. **226** (1993) 1.
  - [2] S. Boffi, C. Giusti, F. D. Pacati and M. Radici, Electromagnetic Response of Atomic Nuclei, Oxford-Clarendon Press, Oxford (1996).
  - [3] J. J. Kelly, Adv. in Nucl. Phys. **23**, Plenum Press, N.Y. (1996).
  - [4] J. D. Walecka, Electron Scattering for Nuclear and Nucleon Structure, Cambridge University Press, Cambridge (2001)
  - [5] A. S. Raskin and T. W. Donnelly, Ann. of Phys. **191**, 78 (1989)
  - [6] T. W. Donnelly and A. S. Raskin, Ann. of Phys. **169**, 247 (1986)
  - [7] C. Y. Prescott *et al.*, Phys. Lett. B **77**, 347 (1978)
  - [8] J. Ashman *et al.*, Phys. Lett. B [EMC] **206**, 364 (1978)
  - [9] V. Y. Alexakhin *et al.* [COMPASS Collaboration], Phys. Lett. B **647**, 8 (2007)
  - [10] A. Airapetian *et al.* [HERMES Collaboration], Phys. Rev. Lett. **92**, 012005 (2004)
  - [11] D. H. Beck and R. D. McKeown, Annu. Rev. Nucl. Part. Sci. **51**, 187 (2001)
  - [12] D. Lhuillier *et al.*, Prog. Part. Nucl. Phys. **61**, 183 (2008)
  - [13] D. von Harrach, Prog. Part. Nucl. Phys. **55**, 308 (2005)
  - [14] J. Gasser and H. Leutwyler, Phys. Rep. **87**, 77 (1982)
  - [15] S. J. Pollock, CEBAF Parity Violation Workshop, CEBAF-PR-86-015 (1986), p. 145

- [16] D. Kaplan and A. V. Manohar, Nucl. Phys. B **310**, 527 (1988)
- [17] Y. B. Dong and D. Y. Chen, Phys. Lett. B **675**, 426 (2009)
- [18] P. A. M. Guichon and M. Vanderhaeghen, Phys. Rev. Lett. **91**, 142303 (2003)
- [19] B. Kubis and R. Lewis, Phys. Rev. C **74**, 015204 (2006)
- [20] M. Viviani, R. Schiavilla, B. Kubis, and R. Lewis, Phys. Rev. Lett. **99**, 112002 (2009)
- [21] D. T. Spayde *et al.* [SAMPLE Collaboration], Phys. Rev. Lett. **84**, 1106 (2000)
- [22] E. J. Beise, M. L. Pitt, D. T. Spayde, Prog. Part. Nucl. Phys. **54**, 289 (2005)
- [23] K. A. Aniol *et al.* [HAPPEX-99], Phys. Rev. C **69**, 065501 (2004)
- [24] K. A. Aniol *et al.* [HAPPEX-a], Phys. Lett. B **635**, 275 (2006)
- [25] A. Acha *et al.* [HAPPEX-b], Phys. Rev. Lett. **98**, 032301 (2007)
- [26] Z. Ahmed *et al.* [HAPPEX-III], arXiv:1107.0913v1 [nucl-ex]
- [27] F. E. Maas *et al.* [PVA4], Phys. Rev. Lett. **93**, 022002 (2004)
- [28] F. E. Maas *et al.* [PVA4], Phys. Rev. Lett. **94**, 152001 (2005)
- [29] S. Baunack *et al.*, [PVA4] Phys. Rev. Lett. **102**, 151803 (2009)
- [30] D. Androić *et al.* [G0 Collaboration], Phys. Rev. Lett. **104**, 012001 (2010)
- [31] D. S. Armstrong *et al.* [G0 Collaboration], Phys. Rev. Lett. **95**, 092001 (2005)
- [32] W. T. H. van Oers, [for the Qweak Collaboration], Nucl. Phys. A **805**, 329c (2008)
- [33] D. S. Armstrong *et al.*, PAC Proposal Update: JLab E02-020, December 10, 2007;  
(<http://www.jlab.org/Hall-C/Qweak/>)
- [34] J. F. Rajotte, Proceedings of the DPF-2011 Conf., Providence, RI.  
arXiv:1110.2218v1 (2011)
- [35]  $\bar{e} - ^2 H$  Parity Violating Deep Inelastic Scattering (PVDIS) at CEBAF 6 GeV, [the Hall A  
Collaboration];  
(<http://hallaweb.jlab.org/experiment/E05-007/>)
- [36] <https://www.jlab.org/12-gev-upgrade>
- [37] M. J. Musolf and T. W. Donnelly, Nucl. Phys. A **546**, 509 (1992)
- [38] M. J. Ramsey-Musolf, Eur. Phys. J. A **24**, 197 (2004)
- [39] S. J. Dong, K. F. Liu, and A. G. Williams, Phys. Rev. D **58**, 074504 (1998)
- [40] R. Lewis, W. Wilcox, and R. M. Woloshyn, Phys. Rev. D **67**, 013003 (2003)
- [41] T. Doi *et al.*, Phys. Rev. D **80**, 094503 (2009)
- [42] R. Babich *et al.*, Proc. Sci., lat2008, 160 (2008)

- [43] G. Bali, S. Collins, and A. Schafer, Proc. Sci., LAT2009, 149 (2009)
- [44] S. Collins *et al.*, Proc. Sci., LAT2010, 134 (2010)
- [45] D. Toussaint and W. Freeman, Phys. Rev. Lett. **103**, 122002 (2009)
- [46] K. Takeda *et al.*, Phys. Rev. D **83**, 114506 (2011)
- [47] D. B. Leinweber *et al.*, Phys. Rev. Lett. **94**, 212001 (2005); **97**, 022001 (2006)
- [48] P. Wang, D. B. Leinweber, A. W. Thomas, and R. D. Young, Phys. Rev. C **79**, 065202 (2009)
- [49] J. D. Bjorken and S. D. Drell, *Relativistic Quantum Mechanics* (McGraw-Hill, New York, 1964)
- [50] T. W. Donnelly and R. D. Peccei, Phys. Rep. **50**, 1 (1979)
- [51] T. W. Donnelly, J. Dubach and I. Sick, Phys. Rev. C **37**, 6 (1988)
- [52] M. J. Musolf *et al.*, Phys. Rep. **239**, 1 (1994)
- [53] J. A. Caballero, T. W. Donnelly and G. I. Poulis, Nucl. Phys. A **555**, 709 (1993)
- [54] M. C. Martínez, J. A. Caballero, T. W. Donnelly, Nucl. Phys. A **707**, 83 (2002)
- [55] H. W. L. Naus and J. H. Koch, Phys. Rev. C **36**, 2459 (1987)
- [56] P. C. Tiemeijer and J. A. Tjon, Phys. Rev. C **42**, 599 (1990)
- [57] L. E. Price *et al.*, Phys. Rev. D **4**, 45 (1971)
- [58] Ch. Berger *et al.*, Phys. Lett. B **35**, 87 (1971)
- [59] K. M. Hanson *et al.*, Phys. Rev. D **8**, 753 (1973)
- [60] F. Borkowski *et al.*, Nucl. Phys. B **93**, 461 (1975)
- [61] R. C. Walker *et al.*, Phys. Rev. D **49**, 5671 (1994)
- [62] J. J. Murphy *et al.*, Phys. Rev. C **9**, 2125 (1974)
- [63] L. Andivahis *et al.*, Phys. Rev. D **50**, 5491 (1994)
- [64] I. A. Qattan *et al.*, Phys. Rev. Lett. **94**, 142301 (2005)
- [65] O. Gayou *et al.* [JLab Hall A Collaboration] Phys. Rev. Lett. **88**, 092301 (2002)
- [66] O. Gayou *et al.* [JLab Hall A Collaboration], Phys. Rev. C **64**, 038202 (2001)
- [67] V. Punjabi *et al.*, Phys. Rev. C **71**, 055202 (2005); **71**, 069902(E) (2005)
- [68] M. E. Christy *et al.* [E94110 Collaboration], Phys. Rev. C **70**, 015206 (2001)
- [69] A. J. R. Puckett *et al.*, Phys. Rev. Lett. **104**, 242301 (2010)
- [70] C. B. Crawford *et al.*, Phys. Rev. Lett. **98**, 052301 (2007)
- [71] M. Paolone *et al.* [E03-104 Collaboration], Phys. Rev. Lett. **105**, 072001 (2010)
- [72] X. Zhan *et al.* [JLab Hall A Collaboration], arXiv: 1102.0318v1 [nucl-ex] 1 Feb 2011

- [73] G. Ron *et al.* [JLab Hall A Collaboration], arXiv: 1103.5784v1 [nucl-ex] 29 Mar 2011
- [74] P. E. Bosted *et al.*, Phys. Rev. C **42**, 38 (1990)
- [75] A. F. Sill *et al.*, Phys. Rev. D **48**, 29 (1993)
- [76] G. Warren *et al.*, Phys. Rev. Lett. **92**, 042301 (2004)
- [77] S. Riordan *et al.*, Phys. Rev. Lett. **105**, 262302 (2010)
- [78] E. Geis *et al.*, Phys. Rev. Lett. **101**, 042501 (2008)
- [79] W. Xu *et al.*, Phys. Rev. C **67**, 012201(R) (2003)
- [80] B. Anderson *et al.*, Phys. Rev. C **92**, 034003 (2007)
- [81] J. Lachniet *et al.*, Phys. Rev. Lett. **102**, 192001 (2009)
- [82] R. Madey *et al.*, Phys. Rev. Lett. **91**, 122002 (2003)
- [83] H. Zhu *et al.*, Phys. Rev. Lett. **87**, 081801 (2001)
- [84] R. Schiavilla and I. Sick, Phys. Rev. C **64**, 041002-1 (2001)
- [85] J. Bermuth *et al.*, Phys. Lett. B **564**, 199 (2003)
- [86] J. Becker *et al.*, Eur. Phys. J. A **6**, 329 (1999)
- [87] C. Herberg *et al.*, Eur. Phys. J. A **5**, 131 (1999)
- [88] M. Ostrick *et al.*, Phys. Rev. Lett. **83**, 276 (1999)
- [89] I. Passchier *et al.*, Phys. Rev. Lett. **82**, 4988 (1999)
- [90] D. Rohe *et al.*, Phys. Rev. Lett. **83**, 4257 (1999)
- [91] T. Eden *et al.*, Phys. Rev. C **50**, R 1749 (1994)
- [92] M. Meyerhoff *et al.*, Phys. Lett. B **327**, 201 (1994)
- [93] G. Kubon *et al.*, Phys. Lett. B **524**, 26 (2002)
- [94] W. Xu *et al.*, Phys. Rev. Lett. **85**, 2900 (2000)
- [95] H. Anklin *et al.*, Phys. Lett. B **428**, 248 (1998)
- [96] E. E. Bruins *et al.*, Phys. Rev. Lett. **75**, 21 (1995)
- [97] H. Anklin *et al.*, Phys. Lett. B **336**, 313 (1994)
- [98] H. Gao *et al.*, Phys. Rev. C **50**, R546 (1994)
- [99] A. Lung *et al.*, Phys. Rev. Lett. **70**, 718 (1993)
- [100] P. Markowitz *et al.*, Phys. Rev. C **48**, R5 (1993)
- [101] A. S. Esauslov *et al.*, Sov. J. Nucl. Phys. **v45**, 258 (1987)
- [102] W. Bartel *et al.*, Phys. Lett. B **39**, 407 (1972)
- [103] W. Bartel *et al.*, Phys. Lett. B **30**, 285 (1969)

- [104] J. J. Kelly, Phys. Rev. C **70**, 068202 (2004)
- [105] J. Arrington and I. Sick, Phys. Rev C **76**, 035201 (2007)
- [106] S. Galster *et al.*, Nucl. Phys. B **32**, 221 (1971)
- [107] R. K. Bhaduri, *Models of the Nucleon: From Quarks to Soliton* (Addison Wesley, 1988)
- [108] G. Höhler *et al.*, Nucl. Phys. B **114**, 505 (1976)
- [109] M. Gari and W. Krumpelmann, Z. Phys. A **322** 689 (1985)
- [110] M. J. Ramsey-Musolf and H.-W. Hammer, Phys. Rev. Lett. **80**, 2539 (1998)
- [111] H.-W. Hammer and M. J. Ramsey-Musolf, Phys. Rev. C **60**, 045204 (1999);  
Phys. Rev. C **62**, 049902(E) (2000)
- [112] E. L. Lomon, Phys. Rev. C **66**, 045501 (2002)
- [113] E. L. Lomon, Phys. Rev. C **64**, 035204 (2001)
- [114] C. Crawford *et al.*, Phys. Rev. C **82**, 045211 (2010)
- [115] M. A. Belushkin, H. -W. Hammer and Ulf-G. Meißner, Phys. Rev. C **75**, 035202 (2007)
- [116] J. C. Bernauer *et al.* [A1 Collaboration], Phys. Rev. Lett. **105**, 242001 (2010)
- [117] J. Liu, R. D. McKeown, and M. J. Ramsey-Musolf, Phys. Rev. C **76**, 025202 (2007)
- [118] C. Amsler *et al.* [PDG], Phys. Lett. B**66**, 1 (2008)
- [119] J. Erler, A. Kurylov, and M. J. Ramsey-Musolf, Phys. Rev. D **68**, 016006 (2003)
- [120] J. Erler and M. J. Ramsey-Musolf, Phys. Rev. D **72**, 073003 (2005)
- [121] W. M. Yao *et al.*, J. Phys.G **33**, 1 (2006)
- [122] W. M. Alberico, S. M. Bilenky and C. Maieron, Phys. Rep. **358**, 227 (2002)
- [123] L. A. Ahrens *et al.*, Phys. Rev. D **35**, 785 (1987)
- [124] N. Baker *et al.*, Phys. Rev. D **23**, 2499 (1981)
- [125] M. Miller *et al.*, Phys. Rev. D **26**, 537 (1982)
- [126] T. Kitagaki *et al.*, Phys. Rev. D **28**, 436 (1983)
- [127] S. L. Zhu *et al.*, Phys. Rev. D **62**, 033008 (2000)
- [128] M. J. Musolf, B. R. Holstein, Phys. Rev. D **43**, 2956 (1991); W. C. Haxton, E. M. Henley,  
M. J. Musolf, Phys. Rev. Lett. **63**, 949 (1989)
- [129] D. B. Kaplan, M. J. Savage, Nucl. Phys. A **556**, 653 (1993)
- [130] C. M. Maekawa and U. van Kolck, Phys. Lett. B **478**, 73 (2000)
- [131] C. M. Maekawa, J. S. Veiga and U. van Kolck, Phys. Lett. B **488**, 167 (2000)
- [132] A. W. Thomas and R. D. Young, Nucl. Phys. A **782**, 1c (2007)

- [133] A. W. Thomas and R. D. Young, Nucl. Phys. A **790**, 173c (2007)
- [134] R. D. Young *et al.*, Phys. Rev. Lett. **99**, 122003 (2007)
- [135] B. W. Filippone and X.-D. Ji, Adv. Nucl. Phys. **26**, 1 (2001)
- [136] D. Adams *et al.* [Spin Muon Collaboration (SMC)], Phys. Rev. D **56**, 5330 (1997)
- [137] J. E. Amaro *et al.*, Nucl. Phys. A **602**, 263 (1996)
- [138] C. E. Carlson and M. Vanderhaeghen, Ann. Rev. Nucl. Part. Sci. **57**, 171 (2007)
- [139] J. Arrington, P. Blunden, and W. Melnitchouk, Prog. Part. Nucl. Phys. **66**, 782 (2011)
- [140] I. A. Qattan, A. Alsaad, and J. Arrington, arXiv:1109.1441v2 [nucl-ex] (2011)
- [141] N. Kivel and M. Vanderhaeghen, Phys. Rev. Lett. **103**, 092004 (2009)
- [142] A. V. Afanasev and C. E. Carlson, Phys. Rev. Lett. **94**, 212301 (2005)
- [143] J. Arrington *et al.*, Tech. Rep. JLab (2004)
- [144] OLYMPUS Collaboration, Tech. Rep., MIT (2009)
- [145] J. Arrington *et al.*, nucl-ex/0408020v1
- [146] S. Ramavataram, E. Hadjimichael and T. W. Donnelly, Phys. Rev C **50**, 1175 (1994)
- [147] A. A. Aguilar-Arevalo *et al.* [MiniBooNE Collaboration], Phys. Rev. D **81**, 092005 (2010)
- [148] T. W. Donnelly, *Invited lecture presented at Lake Louise Winter Institute* (1992)
- [149] M. Gorchtein and C. J. Horowitz, Phys. Rev. Lett. **102**, 091806 (2009)
- [150] A. Sibirtsev, P. G. Blunden, W. Melnitchouk, and A. W. Thomas, Phys. Rev. D **82**, 013011 (2010)
- [151] M. Gorchtein, C. J. Horowitz, and M. J. Ramsey-Musolf, Phys. Rev. C **84**, 015502 (2011)
- [152] Willem T.H. van Oers (for the Qweak Collaboration), Nucl. Phys. A **805**, 329c (2008)
- [153] <http://hallaweb.jlab.org/parity>
- [154] R. D. Young *et al.*, Phys. Rev. Lett. **97**, 102002 (2006)
- [155] K. Aulenbacher, Hyperfine Interactions Volume 200, Numbers 1-3, 3-7 (2011); H. Spiesberger, K. Kumar, F. Mass (private communication).